ISSN-Printed: 2536-5010
ISSN-Online: 2536-5134

Volume 7, No 1, 2017

EJT

EUROPEAN JOURNAL OF TECHNIC

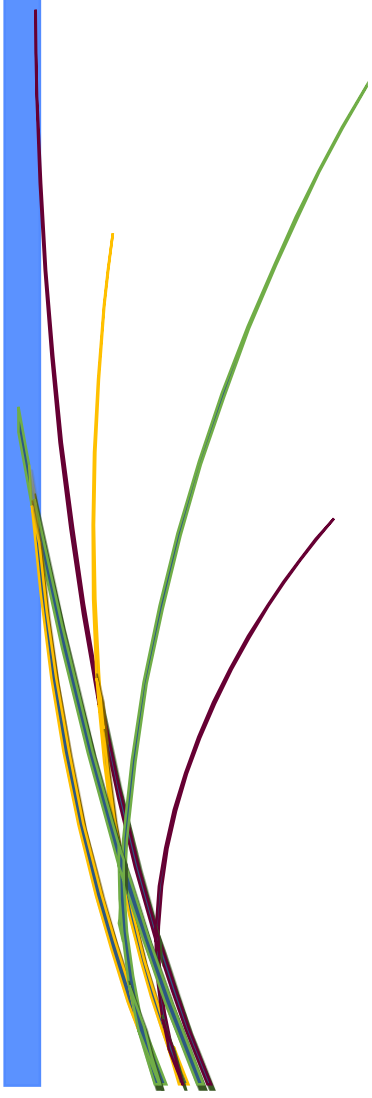

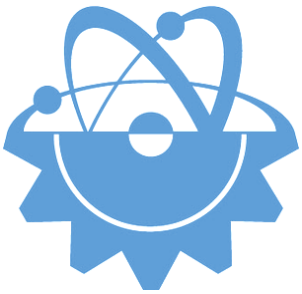

INESEG

Email (for orders and customer services enquiries): ineseg@ineseg.org, ejt@ineseg.org
Visit our home page on www.ineseg.org

EDITORIAL BOARD MEMBERS

TABLE OF CONTENTS

Cover And Editorial Board

Vol 7, Number 1, 2017
European Journal of Technic
EJT

DYNAMIC MODELING OF LITHIUM-ION BATTERY WITH TEMPERATURE EFFECT

Yusuf MURATOĞLU, Alkan ALKAYA *

Mersin University, Mersin, Turkey

* Corresponding author; E-mail: alkanalkaya@mersin.edu.tr

Received: 12 October 2016; Accepted: 25 February 2017

Lithium ion (Li-ion) batteries have become a promising alternative power source in electric vehicles (EVs) due to their high nominal cell voltage, high energy density, long life and not having a memory effect. However temperature effect and dynamic characteristic of the li-ion batteries greatly affects their performance. In this study, a dynamic model of li-ion battery has been developed by MATLAB/Simulink and simulated at different temperatures. Simulink model contains dynamic circuit parameters as a function of state of charge and temperature effect. Simulation results show that proposed dynamic model is effective and operational under the different temperature rates for dynamic output characteristic of li-ion battery.

Key words*: "Li-ion battery", "dynamic battery model", "temperature effect"*

1. Introduction

Lithium ion batteries are widely used in EVs with high energy density, high nominal cell voltage, long life among the various rechargeable batteries such as Lead-Acid batteries, Ni-based batteries and Na-based batteries [1,2]. Li-ion batteries cannot be used without battery management system (BMS) in EVs because of their safety, reliability and performance. BMS include several features such as cell measurement, cell balancing, thermal measurement, safety and reliability [3]. Performance of the li-ion battery related with predict state of charge (SoC) which is a key component of the BMS accurately. The SoC of a battery is defined as a ratio of the remaining capacity and maximum available capacity of a battery and cannot be measured directly. Therefore, SoC should be estimated by using the measured signals such as voltage and current via accurate battery model [4,5].

Several methods used for modelling of the lithium-ion battery in the literature [6-8]. These methods consist of four main groups such as analytical (experimental), statistical, electrochemical and electrical circuit models [9]. Analytical models based on developing physical model of the system with the help of physical equations and determine of model parameters with experimental results are simple and quick method. However, accuracy performance of the model is low [10]. Statistical model which is achieved model parameters by creating significant structures from data samples is a quick method with low accuracy. Electrochemical model based on the operation of the internal chemical structure of the battery is a complex method. Therefore, this method is hardly used [11]. Electrical circuit model, which enables mathematical operations on the equivalent circuit model is the most widely used method [12]. The electrical circuit models mainly include Thevenin model, PNGV

(Partnership for a New Generation of Vehicles) model, NREL (National Renewable Energy Laboratory) model, Randles model [13].

While modelling the li-ion battery, it is essential to consider temperature effect because the ambient temperature and the cell temperature are both greatly affects the behavior of the battery. Several modelling techniques have been proposed to represent the temperature effect of the battery. In reference [14], proposed a battery model which is able to simulate the effects on the battery behavior made by temperature. In reference [15], temperature-dependent cell model is presented to improve state of charge estimation. Temperature effect has become attractive research area topic for battery modelling in electric vehicle field.

In this study, a dynamic model of li-ion battery has been developed with second order Thevenin model by MATLAB/Simulink. Simulink model contains capacity-resistance change effect according to state of charge and ambient temperature effect for dynamic characteristic of the li-ion battery. Proposed dynamic battery model simulated under different temperature conditions.

2. Equıvalent Circuit Model

In this section, Second order Thevenin model shown in Fig. 1 is developed as the equivalent circuit model of the lithium-ion battery due to its high model accuracy and low complexity.

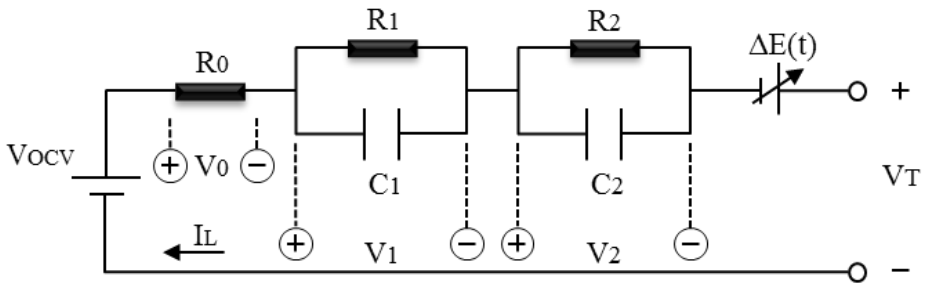

Figure 1. Second order Thevenin equivalent circuit model.

The equivalent circuit model can be described by following equations:

$$V_T = V_{OCV} - V_1 - V_2 - V_0 + \Delta E(t) \quad (1)$$

$$V_0 = R_0 I_L \quad (2)$$

$$C_1 \frac{dV_1}{dt} = -\frac{V_1}{R_1} + I_L \quad (3)$$

$$C_2 \frac{dV_2}{dt} = -\frac{V_2}{R_2} + I_L \quad (4)$$

where R_0 is the ohmic resistance, R_1 and R_2 are the polarization resistance, C_1 and C_2 are the polarization capacitance, V_1 and V_2 are the polarization voltages, V_T is the terminal voltage, V_{OCV} is the open circuit voltage, $\Delta E(t)$ is the potential correction term and I_L is the load current.

3. Open Circuit Voltage

The general equation of the state of charge is expressed as follows:

$$SoC = SoC_0 - \eta \int_0^t i(\tau)\, d\tau \tag{5}$$

Where $\eta = 1/(3600C)$, SoC is the present state of charge, SoC_0 is the initial state of charge and C is the maximum available capacity. The open circuit voltage which is defined as electrical potential difference between the two terminal at the battery when it is disconnected from the electrical load has a non-linear relationship between the state of charge.

4. Equivalent Circuit Parameters

The dynamic parameter values of the equivalent circuit model and state of charge has a nonlinear relationship. In this nonlinear relationship, parameters of the equivalent circuit model have constant values at 20%-100% SoCs. However, parameters of the equivalent circuit model change rapidly due to the chemical reaction in the battery at 0%-20% SoCs. Dynamic parameters of the equivalent circuit model which is related with SoC defined as;

$$R_0 = k_1 \times e^{k_2 \times SoC} + k_3 \tag{6}$$

$$R_1 = k_4 \times e^{k_5 \times SoC} + k_6 \tag{7}$$

$$C_1 = k_7 \times e^{k_8 \times SoC} + k_9 \tag{8}$$

$$R_2 = k_{10} \times e^{k_{11} \times SoC} + k_{12} \tag{9}$$

$$C_2 = k_{13} \times e^{k_{14} \times SoC} + k_{15} \tag{10}$$

where $k_1, k_2, \ldots, k_{15}$ are constant values of the equivalent circuit parameters.

5. Simulation Results

MATLAB/Simulink is used to developed dynamic model of the li-ion battery. Proposed battery model contains $V_{OCV} - SoC$ block, equivalent circuit block, equivalent circuit parameters block and temperature effect block as shown in Fig. 2.

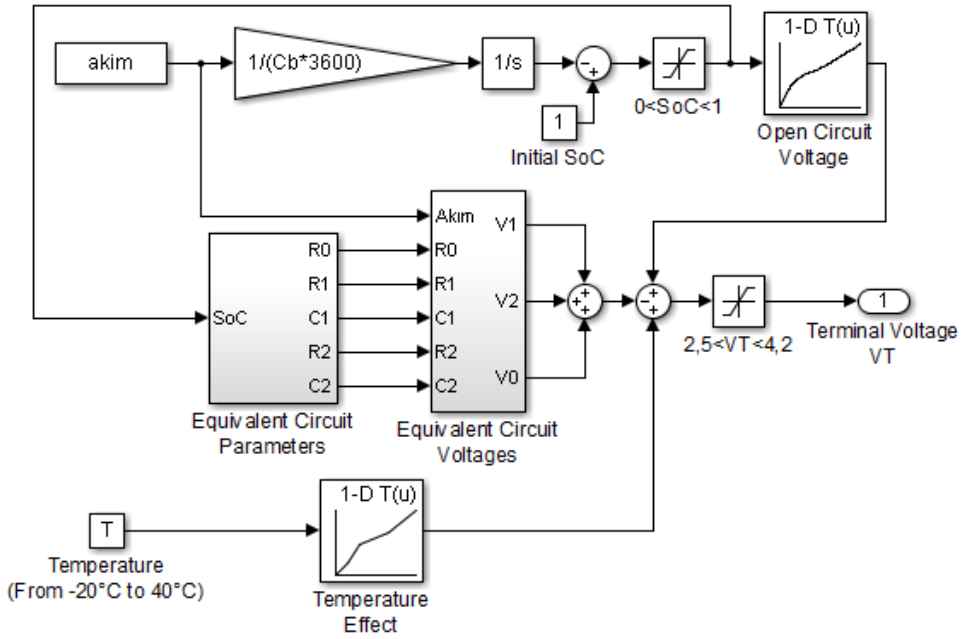

Figure 2. Dynamic Simulink model of li-ion battery.

The change in temperature, affects the equilibrium potential. To compensate this temperature influence, $\Delta E(t)$ is used in Simulink model as potential correction term. Fig. 3 shows that change of $\Delta E(t)$ due to temperature can be found in Ref. [16]. Temperature effect block developed using Fig. 3 as a look-up table.

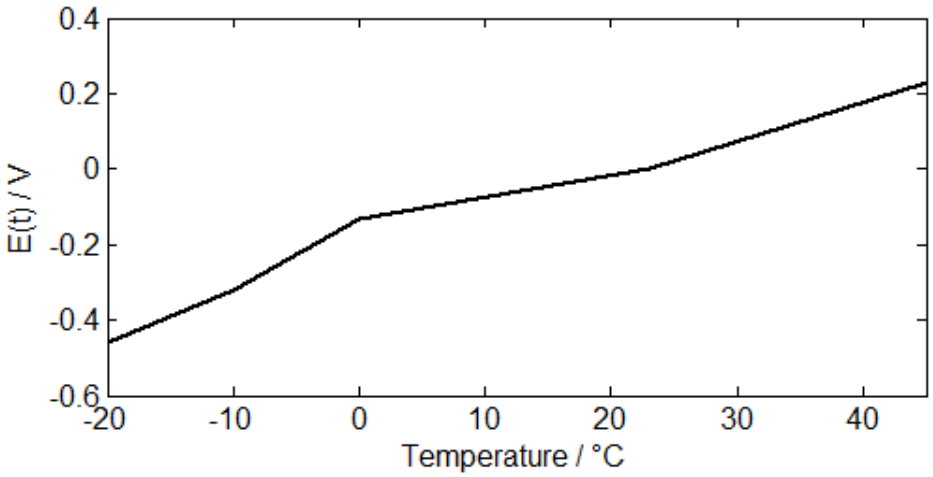

Figure 3. Temperature-dependent potential-correction term for the lithium-ion.

Fig. 4 shows the non-linear relationship between the V_{OCV} and SoC. Open circuit voltage of the battery as a function of SoC is assumed as a seventh-order polynomial equation. It can be represented as:

$$f(V_{OCV}, SoC) = 66.235 \times SoC^7 - 242.73 \times SoC^6 + 364.5 \times SoC^5 - 291 \times SoC^4 + 134.7 \times SoC^3 - 37.016 \times SoC^2 + 6.4617 \times SoC + 2.9007 \quad (11)$$

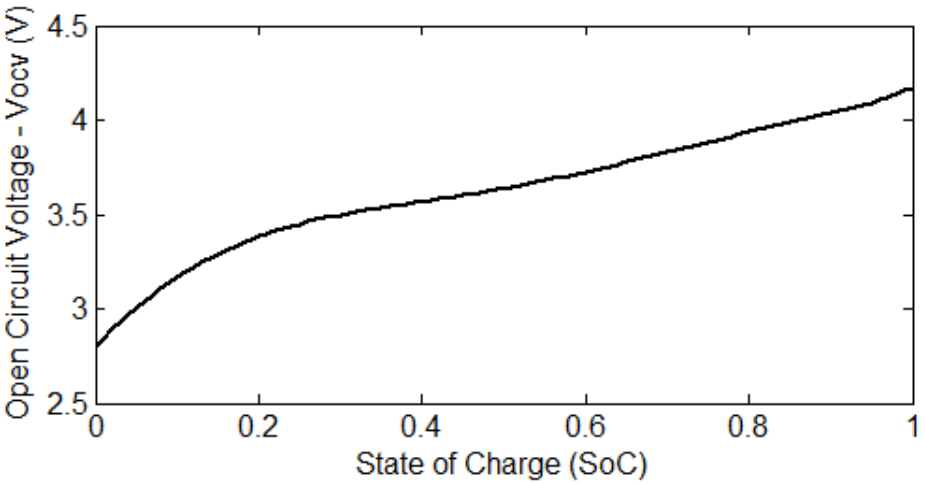

Figure 4. Non-linear relationship between open circuit voltage and state of charge.

Equivalent circuit block developed using Equations (1)-(4). Dynamic parameters of the equivalent circuit model which is related with SoC in equivalent circuit parameters block defined as;

$$R_0 = 2,2236 \times e^{-33,8871 \times SoC} + 0,016 \quad (12)$$

$$R_1 = 0,000124 \times e^{-25,0869 \times SoC} + 0,1656 \quad (13)$$

$$C_1 = 732,6083 \times e^{-11,6207 \times SoC} + 690,5780 \quad (14)$$

$$R_2 = 44,6259 \times e^{-333,6240 \times SoC} + 0,0257 \quad (15)$$

$$C_2 = 6191,5 \times e^{-10,6698 \times SoC} + 4470,1 \quad (16)$$

Proposed battery model is tested using 0.2C (0.65 A) discharge test data with different temperature condition such as $-20°C$, $-10°C$, $0°C$, $10°C$, $20°C$ and $40°C$. Fig. 5 displays the change of terminal voltage for dynamic battery model with different temperature effect.

The change in temperature has deeply affected terminal voltage. The terminal voltage and the temperature affect each other negatively. When the temperature increases, the terminal voltage is decrease as shown in Fig. 5.

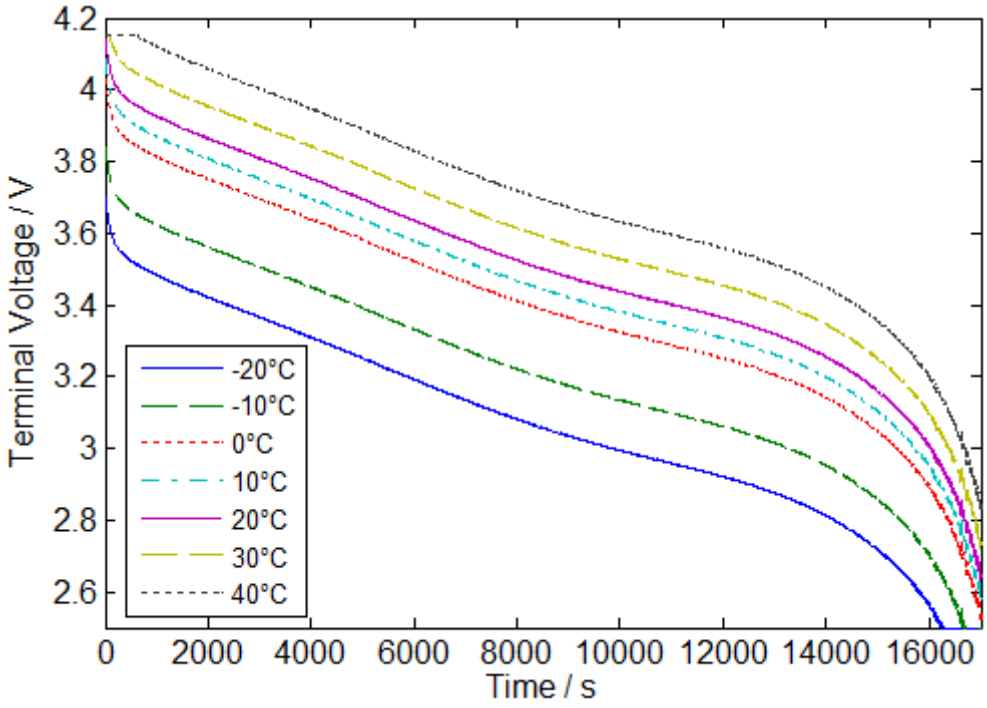

Figure 5. The change in battery runtime for a 0.65 A discharging condition at different temperatures.

Conclusion

In this study, dynamic battery model including capacity-resistance change effect at dynamic characteristic of the li-ion battery is proposed. Dynamic battery model developed by MATLAB/Simulink is tested using 0.2C (0.65 A) discharge test data and different temperature effects at $-20°C$, $-10°C$, $0°C$, $10°C$, $20°C$ and $40°C$. Simulation results show that developed temperature depended dynamic model can reflect the output characteristic of li-ion battery effectively.

Acknowledgment

The authors would like to thank for the financial support by scientific research project unit of Mersin University (Project number: BAP-2015-TP2-1196).

References

[1] Wang, Q., *et al*., A critical review of thermal management models and solutions of lithium-ion batteries for the development of pure electric vehicles, *Renewable and Sustainable Energy Reviews, 64* (2016), pp. 106-128.

[2] Abada, S., *et al*., Safety focused modeling of lithium-ion batteries: A review, *Journal of Power Sources, 306* (2016), pp. 178-192

[3] Rahimi-Eichi, H., *et al*., Sensitivity analysis of lithium-ion battery model to battery parameters, *In Industrial Electronics Society, IECON 2013-39th Annual Conference of the IEEE,* (2013), pp. 6794-6799

[4] Xiong, R., *et al*., Evaluation on state of charge estimation of batteries with adaptive extended Kalman filter by experiment approach, *IEEE Transactions on Vehicular Technology, 62* (2013), 1, pp. 108-117

[5] He, Y., *et al*., A new model for State-of-Charge (SOC) estimation for high-power Li-ion batteries, *Applied Energy, 101* (2013), pp. 808-814

[6] Wijewardana, S., *et al*., Dynamic battery cell model and state of charge estimation, *Journal of Power Sources, 308* (2016), pp. 109-120

[7] Rahman, M. A., *et al*., Electrochemical model parameter identification of a lithium-ion battery using particle swarm optimization method, *Journal of Power Sources, 307* (2016), pp. 86-97

[8] Rao, R., *et al*., Battery modeling for energy aware system design, *Computer, 36* (2003), 12, pp. 77-87

[9] Fotouhi, A., *et al*., A review on electric vehicle battery modelling: From Lithium-ion toward Lithium–Sulphur, *Renewable and Sustainable Energy Reviews, 56* (2016), pp. 1008-1021

[10] Rong, P., Pedram, M., An analytical model for predicting the remaining battery capacity of lithium-ion batteries, *IEEE Transactions on Very Large Scale Integration (VLSI) Systems, 14* (2006), 5, pp. 441-451

[11] Krintz, C., *et al*., Application-level prediction of battery dissipation. In *Proceedings of the 2004 international symposium on Low power electronics and design,*(2004), pp. 224-229

[12] Bae, K. C., *et al*., LiFePO4 dynamic battery modeling for battery simulator, *In Industrial Technology (ICIT), 2014 IEEE International Conference on,* (2014), pp. 354-358

[13] He, H., *et al*., Evaluation of lithium-ion battery equivalent circuit models for state of charge estimation by an experimental approach, *Energies, 4* (2011), 4, pp. 582-598

[14] Tan, Y. K., *et al*., Modelling of battery temperature effect on electrical characteristics of Li-ion battery in hybrid electric vehicle, *In Power Electronics and Drive Systems (PEDS), 2011 IEEE Ninth International Conference on*, (2011), pp. 637-642

[15] Baronti, F., *et al*., State-of-charge estimation enhancing of lithium batteries through a temperature-dependent cell model, *In Applied Electronics (AE), 2011 International Conference on*, (2011), pp. 1-5

[16] Gao, L., *et al*., Dynamic lithium-ion battery model for system simulation, *IEEE transactions on components and packaging technologies*, *25*, (2002), 3, pp. 495-505

DETERMINATION OF GEOLOGICAL AND GEOPHYSICAL (ELECTRICAL-VESMETHOD) FEATURES OF THE KARST CAVITY IN THE ESENTEPE REGION OF BATMAN PROVINCE

Nuray ALPASLAN[1]*, Ferhat ÖZÇEP[2], Mehmet Can BALCI[3], Nuray ÖNCÜL[4]

[1]*University of Batman , Faculty of Arts and Sciences, Department of Conservation and Restoration of Cultural Heritage

[2]University of İstanbul, Faculty of Engineering, Geophysics Engineering

[3]University of Batman, Faculty of Engineering, Civil Engineering

[4]Havin Engineering, Yılmazlar Center Kat:6 No:609,BATMAN, TÜRKIYE

* Corresponding author; E-mail:nuray.alpaslan@batman.edu.tr

Received: 15 October 2016; Accepted: 27 February 2017

Abstract:

Within the scope of this study; in order to reveal physical features of the ground pit which is considered to be the karst cavity in the Esentepe region of Batman Province, geological and geophysical researches were conducted. Within the framework of the geological studies carried out in the examination area, 4 exploratory drillings in total of 75 meters depth were performed at the locations determined with the purpose of identification of the changes in lateral and vertical directions of the geological and lithological status, the groundwater level and the engineering parameters of the ground pit which is thought to be in the karst cavity structure in Esentepe region. With the intent of detection of the physical features of the ground layers that were passed during borehole drilling, Standard Penetration Test (SPT) was carried out. Moreover, ground's natural unit bulk density, water content, sieve analysis and Atterberg limits were determined on the disturbed (SPT) andundisturbed (UD) specimens taken from the boreholes, and consolidation & Tri-axial Compression Tests were performed. Geophysical researches conducted in the examination area consist of Vertical Electrical Sounding. As geophysical study; vertical electrical sounding was performed at 2 points. Visible resistivity distance curves & ground electric sections of the Vertical Electrical Soundings and the lithology of the underground structure were evaluated by using Ipı2win program. Furthermore, in the examination area, with the multi-electrode resistivity method, resistivity area data obtained via AGI R8 device capable to measure 8-channel 84-electrode resistivity and IP were evaluated in the Earthimager 2D program which is a computer based evaluation program.

Comments were made by correlating the evaluations and the regional geology. Within the scope of the study, mechanism of the pit formations in karst cavity structure causing problems such as subsidence in the structures, construction of which is thought and as ground failure on the grounds on where these structures will be constructed, occurring at the city center of Batman Province was examined.

Key Words: Batman, Karst Cavity, Resistivity, Vertical Electric Sounding,Standart Penetration Test

1.Introduction

The main reason of the sinkhole formation can be explained by the fact that the limestone or similar soluble soil formations (dolomite, gypsum, halite etc.) can be dissolved with water having an acidic character [1, 2, 3]. In general, the most important indicators for the sinkhole formation are the emergence of fresh surfaces in the areas of contact with various sustaining walls or structures as well as bending or slipping on the sustaining walls. The speed of the melting hole, which forms the most common type of sinkholes in terms of formation mechanism, runs completely parallel with the melting rates of the limestone forming the soil. These rocks are soluble. With the dissolution of the karst rocks, only a small amount of residual material is retained. Therefore, expanding fractures and cracks do not get closer and the underground water circulation is not blocked. As a result, slowly collapsing land surfaces are formed.

The units containing sand in various regions of Batman Province and the sinkholes in the karst space structure may lead to problems such as subsidence of the constructions and soil failure in the construction space. Detection of these units prior to settlement is of great importance in terms of prevention of loss of life and property by eliminating the engineering problems that may occur during and after construction. It is known that there are many sinkholes in Batman Provincial centre. In the previous studies, especially the formation of sinkholes seen in the south of Esentepe, Gültepe district, has been investigated. During the construction of road by the Municipality personnel on October 6, 2011, a hole extending to the south of Esentepe area was found in the upper part of the road with the removal of the 30-30 cm thick soil cover. During the works on the field subsidence in two different places were found apart from other sinkholes in the same region. Each of the three subsidence are in the same direction and on about K 40-50B. The mouth size on the surface of the sinkhole is approximately 1 m x 0.75 m (Figure 1.a). The sinkhole is 8 m in depth and has a rectangular form. From this section, the sinkhole makes a 17 meters-long depth while the width is reduced to till 1.5 meters. The fault forming the northern wall of the sinkhole is covered by the newly formed sediments about 5 meters thick [4] (Figure l.b).

Figure 1a. View of the Sinkhole found in the South of Esentepe

Figure 1b. 5m Vertical View of the Fault from the Mouth of the Sinkhole (Eren et.al. 2012)

Batman province is located in the South-eastern Anatolia, whose neighbours are Muş in the north, Diyarbakir in the west, Bitlis and Siirt in the east and Mardin in the south. The field under investigation is the Esentepe District of Batman located in the city centre (Figure 2).

Figure 2. The Site Location Map of the Investigated field

2. The Geology of the Investigated field

Batman is geologically based on the Şelmo Formation and the Quaternary units consisting of upper Miocene-Pliocene aged mudstone sandstones and conglomerates. Aside from these units, the Eocene-Oligocene units that are exposed to the West Raman Mountain in the south are the oldest units in the investigated field (Figure 3). The limestone at the surface of West Raman Mountain and the dolomitic limestones form the Hoya Formation. The age of the 228m-thick unit between Batman Hasankeyf is Lower Eocene-Lower Oligocene [5].The unit represented by limestone, gypsum and shale on the northwest slopes of Raman Mountain forms the Germik Formation. This formation is composed of partly silty and sandy dolomite, limestone shale and white gypsum alternation. This unit is assessed to be within the Midyat Group and to correspond to the regressive evaporitic phase of the Upper Eocene Oligocene age [5].

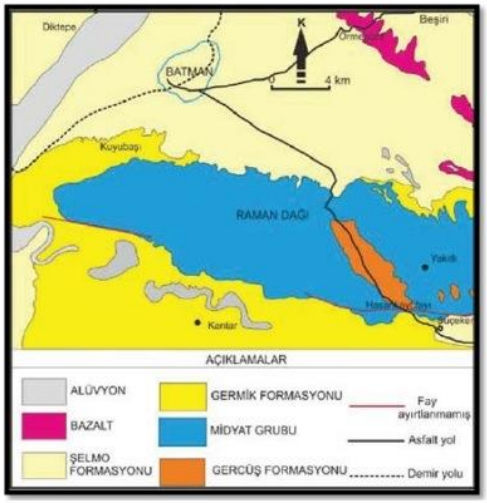

Figure 3. Geological Map of Batman City (prepared by adapting the MTA's 1 / 500,000 scale geology map)

Figure 4 shows the geological section of the investigated field. At the bottom of the formation are gypsum and salt-bedded sandstone and mudstone alternates, while at the upper parts are loosely attached conglomerate, sandstone and shale alternates. The unit is Upper Miocene-Lower Pliocene age. To the east of the city of Batman, Aydınkonak and Akça, the newly formed Pliocene sediments which are predominantly the loosely attached conglomerate and the sandstone on Şelmo Formation are considered to be the Lahti Formation defined in the Adıyaman region [5].

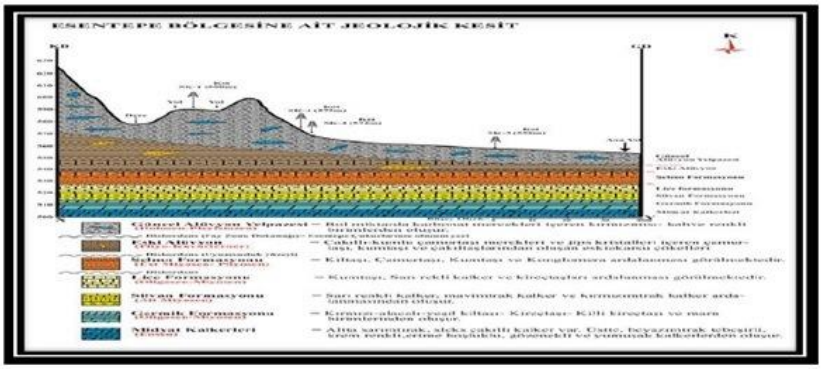

Figure 4. Geological Section of the Investigated Field

3. Findings of the research

3.1. Field Research and experiments

Within the frame of geological studies in the field of investigation, totally 75 meters long depth is drilled with 4 drills of 19.50 meters and 1 drill of 16.50 meters in the pre-chosen locations to determine the changes in the lateral and vertical directions of the geological and lithological state of the ground sinkhole, thought to be a part of karstic space in the Esentepe region, and to define engineering parameters. The index properties of the soil were determined and Standard Penetration Test (SPT) was performed in every well to determine the physical properties of the soil layers during

drilling. Figure 5 shows the general view of the sinkhole where the drilling work of SK-2 is made. It is seen that the units in SK-2 drilling wells are formed by the alternation of Clayed Sand and Sandy Clay levels where the Recent Alluviums of the Quaternary age are dominant (Figure 6).

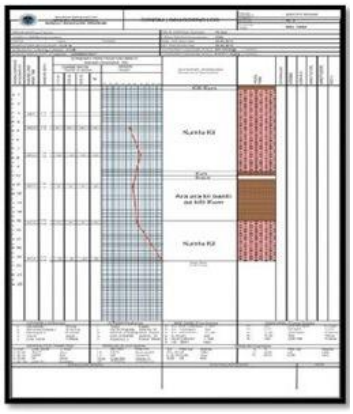

Figure 5. Overview of the drilled sinkhole Figure 6. SK-2 Log

According to the results of the SPT Tests obtained from the drillings in the field of investigation, the values in the SK-2 borehole shows that it is formed with the alternation of Clay Sand and Sandy Clays levels where the Recent Alluviums of the Quaternary age are dominant; and according to the SPT values it is in the form of solid and very solid soil. From the SPT-1 and SPT-2 values at the first 14-16 m levels of the SPT-N values obtained from the SK-3 borehole, it is understood to show a solid and very solid soil behaviour according to the soil classification (Table 1).

Table 1. SPT Experiment Results and Samples Obtained from Drills in the Field of Investigation

Drill No.	Depth (m)	SPT (N) Values
SK-1	19,50	UD-1=>2,00-2,15,SPT-1=> N=75,SPT-2=>N=81,SPT-3=> N=87
SK-2	19,50	UD-1=>3,00-3,20,SPT-1=> N=47,SPT-2=> N=63,SPT-3=>N=52,SPT-4=N=58,SPT-5=> N=50+
SK-3	19,50	SPT-1=>N=10,SPT-2=> N=20SPT-3=> N=66
SK-4	16,50	UD-1=>4,50-4,70,SPT-1=> N=18,SPT-2=> N=23,SPT-3=> N=71

3.2. Laboratory Experiments and Analyses

To define the lithological and geological states of the soil in the field as well as the engineering parameters, the Atterberg limits are determined and consolidation and triaxial compression test is made for the unit volume weight, water content, sieve analysis of the soil based on the disturbed and

undisturbed samples taken from the drilled wells. The liquid limit (PL) and plastic limit (PL), which are known as Atterberg Limits, were found in experiments on soil samples in sieve analysis and the Plasticity index (PI) was calculated. Table 2 gives the plasticity values according to the liquid limit range.

Table 2.Plasticity Values according to the Liquid Limit Range [6]

Liquid Limit Range (%)	Plasticity Degree	Description
<35	Low Plasticity	Oil-free or silty
35–50	Medium Plasticity	Medium oily
50–70	High Plasticity	Oily
70–90	Very High Plasticity	Very oily
>90	Excessive Plasticity	Excessively oily

Table 3. The index properties of obtained from drilled wells in the investigation field.

Drill no.	Sample No.	Depth (m)	Neutral density (gr/cm3)	Water content (%)	Liquid Limit (%)	Plasticity Limit (%)	Plasticity index (%)	Class
SK2/SPT-1	SPT-2	4.50	1.86	18.7	29.5	18.5	11.0	CL
SK2/SPT-2	SPT-2	7.50-8.00	1.90	11.3	24.3	17.9	6.4	SC
SK2/SPT-3	SPT	11.00	1.93	10.3	25.2	18.5	6.7	SC
SK2/SPT-4	SPT-15	15.50	1.86	18.9	26.2	17.0	9.2	SC
SK2/SPT-5	SPT	19.50-20.00	1.87	24.1	46.3	22.8	23.5	CI
SK3/SPT-1	SPT-1	4.50	1.90	12.2	27.9	17.9	10.0	SC
SK3/SPT-2	SPT-2	12.00	1.94	8.9	25.6	17.2	8.4	SC
SK3/SPT-3	SPT	20.00	1.85	18.9	26.0	17.3	8.7	CL

According to the Atterberg (plasticity) experiments on the soil samples obtained from the drilled wells, the Liquid Limit is found to be at the range of % 46.3 and % 24.3 and the Plasticity index (PI) is found to be at the range of 23.5 and % 6.4. According to the United Soil Classification System (USCS) laboratory tests made on the samples obtained from the SK-2 and SK-3 drilled wells in the field of investigation, the soil classes of the units composing the soil are found to be as follows: Soil class CL, inorganic clay with law plasticity; Soil class SC, clayed soil; and Soil class CI, clay with medium plasticity (Table 3).

The water content is the ratio of the weight of a specific volume of water to its dry weight. The water content values of the samples obtained from the drilled wells in the investigation field are shown in Table 3 according to the geotechnical laboratory results. The water content of the floor in the study area is calculated between 12% and 25%. Natural density values range from 1.94 gr / cm3 to 1.82 gr / cm3 (Table 3).

3.3. Geophysical Electrical Method Studies in the Field of Investigation

Electric-Resistance is the method of calculating the resistivity and thickness values of the underground layers by measuring the potential of the electric field created by underground artificial current. The resistivity is the inverse of the conductivity, which is the electrical conductivity of a material and has the unit of ohm-m. The equipment used in the electrical resistivity method is a current source (battery and generator), a transmitter (controlled current transmitter unit), current and potential cabling and electrodes (Figure 7). A complex drill-profile section with various arrays of currents (A, B) and voltage (M, N) electrodes is obtained with the greatest depth of research depending on the total length of the cable. Electrode arrangements can be used in different shapes (Wenner-Schlumberger, Dipole-Dipole, etc.) [7]. In the investigation field the SUPER STING R8 IP resistivity measurement equipment was preferred (Figure 8).

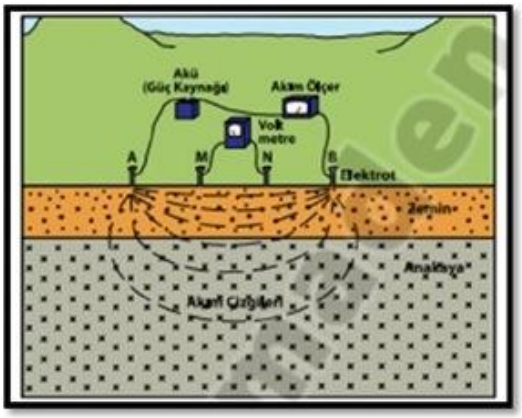

Figure 7. Typical Resistance Method's application in the Field [8]

Figure 8. SUPER STING R8 IP Resistivity Equipment

Vertical electric drilling technique (Figure 9) was used to investigate the vertical changes in the underground in the area of investigation, and directional measurements were made at separate points

(EAST-WEST). For this purpose, vertical electrical drilling measurements were made in two locations in the field of investigation. AB / 2 gap was applied as 30 m and electrode scheme was a schlumberger. Visible resistivity curves were plotted using the IpI2win program for apparent resistivity values obtained by the vertical electric resistivity method in the field of investigation. The electrical section of the investigation field is obtained by the electrical resistance values; and applying the measured values of Des-1 and Des-2 to the IP2win program.

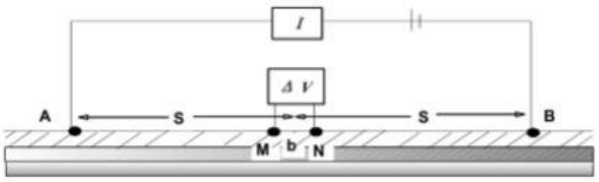

Figure 9. DES- Schlumberger Electrode Expansion [9]

It was tried to obtain resistivity values from layers up to about 36 inches deep by making an 80 m opening at the DES-1 point of the investigated field. At this point, the resistivity values at the level of 8.83 IN to 10,4 m were 1,08 ohm-m, which showed low resistivity values compared to other layers. The low clay value of 10 indicates that the ground is exposed to water (Figure 10).

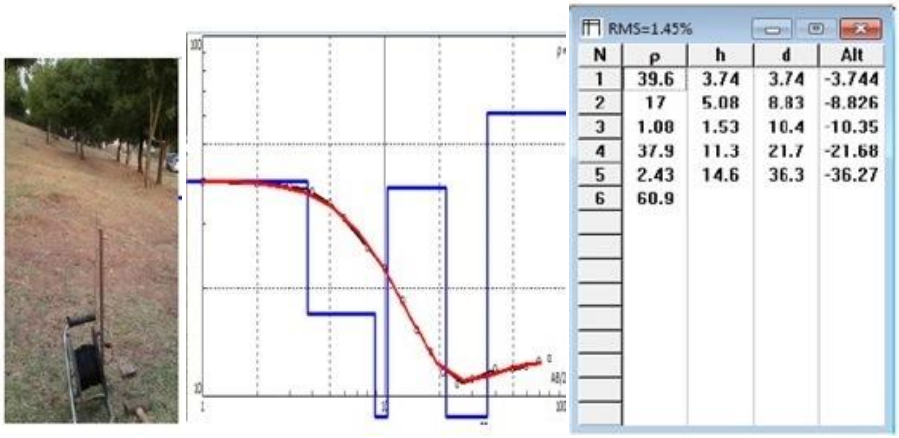

Figure 10. The measurement value of DES-1

It was tried to obtain the resistivity values from the layers up to about 30 m depth by making an 80m opening at the DES-2 point in the investigated field. At this point, the resistivity values at the level of 10.4 m to 33.2 m were 6.72 ohm-m and the resistivity values were low compared to other strata (Fig. 11).

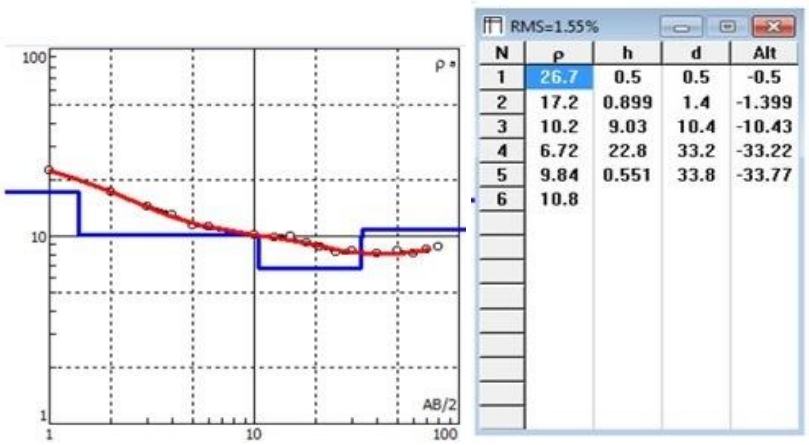

Figure 11. DES-2 Measurements

The electric section of the investigated field was created with the measurement values obtained from the Des-1 and Des -2 points by applying the IP2win program (Figure 12). According to the low electrical resistivity values of the DES (Vertical Electricity Drilling) sections obtained from DES study performed in the field, loose or potentially water-containing loose units are detected between 5.22 and 13.11 meters and water-containing units are detected between 7.94-9.81 meters. Low resistivity values between 4 m and 10 m in the DES (Vertical Electrical Drilling) sections obtained by the Vertical Electrical Drilling (DES) study made in the field of investigation show the possibility of underground water at the 4th meter (Figure 12). The most important evidence of the existence of groundwater is undoubtedly the significant resistivity reductions in regions very close to the groundwater level. The decrease in the resistivity value indicates that the grain diameter of the structure is reduced and vice versa, the growth of the resistivity value indicates the growth of the grain diameter. The gravel content of the clay at some levels lead to an increase in the resistivity, whereas the clay content of the sand at some levels lead to a decrease in the resistivity.

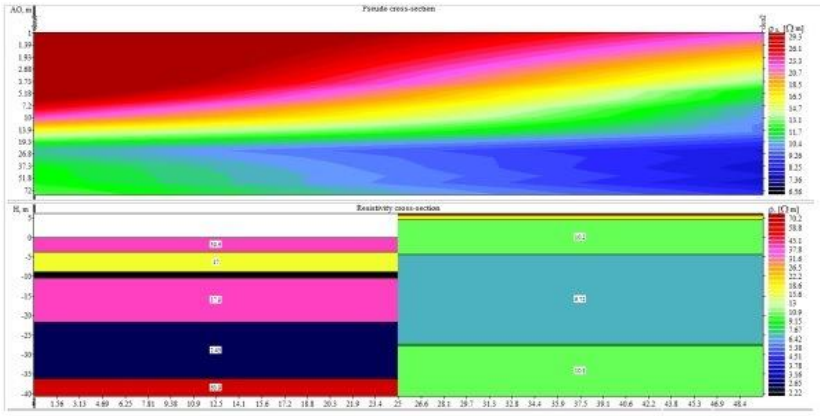

Figure 12.Des-1 Des -2 Soil Electrical Section

In recent years, rapid developments in the field of electronics and computers have enabled the development of an automatically-changeable multi-electrode resistivity measurement method (electrical resistivity imaging), which allows drilling-profile measurements to be taken along a

direction. Today, thanks to multi-electrode measuring devices, it is fast and easy to make measurements. From the data measured by this method, information about the resistivity structure in both the vertical and horizontal directions of the underground can be obtained. In the multi-electrode method, the measuring device is computer controlled. After all the electrodes are connected to the measuring device by a single cable, they are measured sequentially for the desired electrode array. As a result, this allows making measurements at certain stations (points) and for certain AB / 2 values and direct drilling-profile measurements. With this data, a pseudo-section is obtained. In the application of the electrical method to the multi-electrode system, the visible resistivity pseudo-section data is interpreted by an inversion algorithm to obtain resistivity depth sections along the profile for potential indicator points, showing the 2D resistivity structure for both lateral and vertical directions [10]. Also in this study, multi-electrode electrical measurements were made in the field to extend the depth of the investigation (Figure 13).

Figure 13. Measurement in the field with the multi-electrode electrical resistivity method

In the investigation field, the resistivity field data obtained with the AGI R8 device capable of measuring resistivity and IP with 84 electrodes and 8 channels by the vertical electrical drilling (DES) method was evaluated in the Earthimager 2D program, a computer evaluation program.The assessments were made in correlation with the regional geology. Dipol-Dipol-Gradiant method was applied in the resistivity studies and the electrodes were placed 2-4 meters apart. 42 electrodes were placed. 2 series were made. These measurements were evaluated in the Eartlmager 2D evaluation program. These evaluations were converted to a horizontal image. In order to determine the depths, thicknesses, resistivity values and water retention properties of underground units, the profile resistivity and geophysical underground structure of the profile are drawn. The data obtained from the points evaluated in the computer evaluation programs were transferred to the related sections and maps after data integration was completed. Two-dimensional sections were obtained in resistivity measurements in the investigated field and named as ERT1, ERT2 profiles (Table 4).

Table 4. The Electrode Distances and Profile Lengths of Electrical (Resistivity) Measurement Profiles

Lines	Electrode distance	Profile Length
ERT1	**2 m**	**84 m**
ERT2	**4 m**	**168 m**

With one - two-dimensional resistivity values obtained from the investigated field were tried to make a section between different electrode gaps along two profiles. Different interpretations have been developed about the approximate cover thicknesses as well as existence and the depths of groundwater in these 2 dimensional sections. The points taken for ERT locations in the survey area have been mapped in UTM 37 T Zone and ED50 6 degree coordinate system.

ERT-1, an 84-m line, is roughly North-South (K-G) directional and plotted along the average level of elevation along the line. A 2-m electrode space was chosen and arrayed accordingly (Fig. 14). Very close units are detected in this section after application of the Dipole-Dipole-Gradient method.

Because of the high level of alluvium, generally the gravel levels in the sections determine the resistive units. This profile generally corresponds to silty, sandy, clayed and gravelly levels. The units are generally very close to each other. It was examined in 5 different levels. As it is shown in the ERT-1 section in Figure 14, **clay** unit is represented by blue, **fine gravelly clay** unit is represented by green, **coarse-gravelly sandy clay** unit is represented by red, the **less sandy clay** unit is represented by light blue, and the **fine gravelly clay** unit is represented by yellow. This dominant unit is the **less sandy clay** unit. On the surface is generally the clay unit with a blue legend, followed by smooth grain-dispersed gravelly clay unit and then a coarse gravelly clay unit.

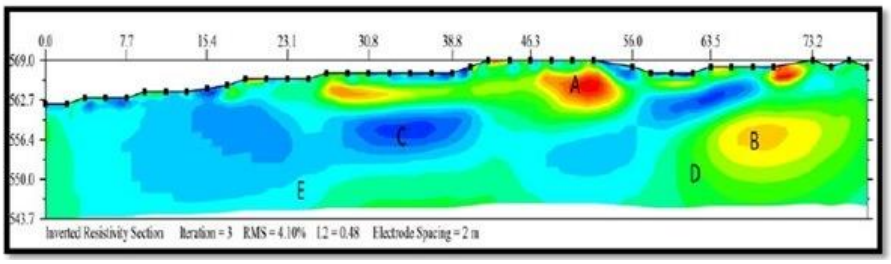

Figure 14. ERT-1 Section

As it can be seen in the conductivity model of the ERT-1 section in Figure 15, resistivity is higher in the 46.3- to 63.5-meter section than in the other units. The decrease in conductivity and the increase in resistivity is due to the decrease in the thickness of that unit and the reduction in the contact structure among the units. The clay value of less than 10Ω indicates that the soil exposed to water. The conductivity value is high in most of the section.

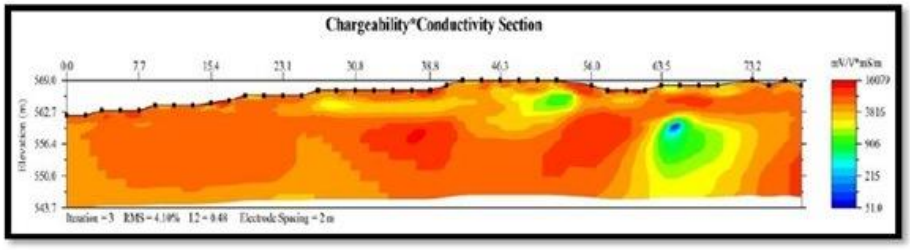

Figure 15. ERT-1 The Conductivity Model of the Section

ERT-2 is a north-south (K-G) directional in a length of 168 m and parallel to ERT-1, and average height levels along the section are plotted. The electrode gap was chosen to be 2 m and arrayed accordingly (Fig. 16). Very close units have been detected in this section with application of Dipole-Dipole-Gradient methods. The section generally consists of 4 units. But these units are very close to each other. In general, the B-C units represent clay units as it is seen in the ERT-2 section in Figure 16. The D unit yellow zone represents generally the sandy clay units. In this section, the resistivity value of the blue zone under the 101st meter is very low, probably surface waters from this area are leaking into the underground. Since the clay unit just below zone A does not pass through the water, the leaks occur southwards underground. It is thought that this area consists of hollow units containing sandy waters of about 12 meters deep at A region.

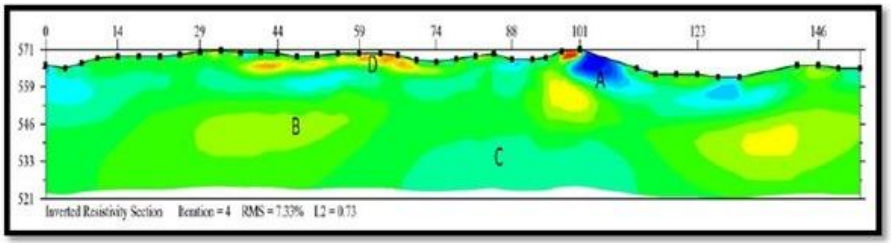

Figure 16. ERT-2 Section

As it is seen in the conductivity model of the ERT-2 section in Figure 17, the spread of the conductivity is shown in the section. Red and yellow zones, probably as a legend of excessively watery zones are highly observable.

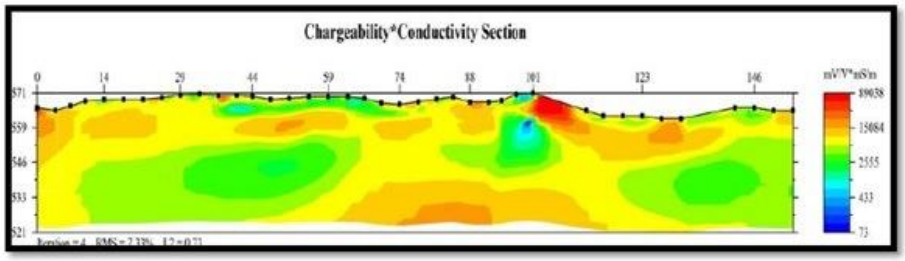

Figure 17. ERT-2 The Conductivity Model of the Section

4. Conclusion

In this study, the investigations made within the geological surveys in the Batman City Esentepe Region indicate that the investigated field is composed of quaternary aged units formed by alternation of Clayed Sand and Sandy Clay levels and behaves as a solid and very solid soil according to SPT-N values. Although the soil parameters found with the geological examinations in the Batman City Esentepe Region are suitable for settlement, it is observed that the calcium carbonate lenses in the clayed sand units form large-scale sinkholes under the effect of tectonism. In underground cavities, there are usually closures with high-value resistivity curves in accordance with the shape of the cavity. If the space is limestone and the interior is filled with ionized water, the closures are determined by low-value resistivity curves.

The low resistivity values between 4 m and 10 m in the DES (Vertical Electrical Drilling) sections obtained by the Vertical Electrical Drilling (DES) study conducted in the investigated field

indicate the possibility of underground water at the 4th meter. The most important evidence of the existence of groundwater is undoubtedly the significant resistivity reductions in regions very close to the underground water level. A decrease in the resistivity value indicates that the grain diameter of the structure is reduced and vice versa, an increase in the resistivity value indicates a growth in the grain diameter. The gravel content of the clay at some levels lead to an increase in the resistivity, whereas the clay content of the sand at some levels lead to a decrease in the resistivity. The resistivity values were found to be low in the sandy space structure between 9.50 m – 10.50 m in the resistivity model, mechanical drilling results and especially the DES-1 resistance model and SK-2 drilling. Again, in SK-2 drilling, a low resistivity value is seen at 0.50-9.50 m sandy clay level. In the obtained conductivity model, the resistivity value between 46.3 and 63.5 meters is higher than the other units; the decrease in the conductivity and the increase in resistance result from the decrease in the thickness of the units due to the decrease in contact structure among the units. The clay value of less than 10 Ω indicates that the soil is exposed to water. Considering the increase in the number of sinkhole formation in Batman city centre it is suggested that the drilling values taken from where the base of the construction will be settled in the field should not be assessed alone; rather an extensive engineering studies should be carried out in the areas to be opened for construction.

References

[1] Bates, R. L. & Jackson, J. A. 1987. Glossary of Geology. Third edition, American Geological Institute Alexandria, VA.

[2] Elrod, M., 1899. The Geologic Relations of Some St. Louis Ground Caves and Sinkholes. Indiana Academy of Science Proceedings, 1898, 258-267.

[3] Fetter, C.W.,1980. Applies Hydrogeology, Columbus, Ohio. Merrill Publishing, 488p

[4] Eren, Y. , Nalbantçılar, M.T. , Beyaz, T. , Dinç, S. , Ünal, M. , Arslan, Ş. & Polat, S., 2012.Formation mechanism of Esentepe (Gültepe/Batman) Karst Cavity, Batman University Life Sciences Journal, 1(2), 385-394.

[5] Yılmaz, E.& Duran, O. 1997. Southeastern Anatolia Region Otokton and Allokton Units Stratigraphy Naming Convention,syf. 241, T.P.A.O. Research Center Group Presidency Education Publications. No: 31, Ankara.

[6] Bell, F.G., 2007. Engineering Geology. Second edition, Butterworth-Heinemann is an imprint of Elsevier,UK-USA, 581p.

[7] Bernard, J., Orlando, L., & Vermeersch, F., 2004. Electrical rezistivity imaging for environmental applications. 16th International Geophysical Congress and Exhition of Turkey, Abstracs Book,376-379

[8] Robinson, E.S., & Coruh, C., 1988, *Basic exploration geophysics* Wiley, New York,562 p.

[9]Başokur, A.T.,2004. Interpretation of Vertical Electric Drilling Data, Lecture Note

[10]Candansayar, M.E., 2005. Underground water searches with direct current resistivity method, *Seminar Notes of Engineering Geophysics and Applications, Chamber of Geophysics Engineers*,52- 114

COMPARISON OF PARAMETERIZATION METHODS USED FOR B-SPLINE CURVE INTERPOLATION

Sıtkı ÖZTÜRK[1], Cengiz BALTA[1], Melih KUNCAN[2*]

[1]Kocaeli Üniversitesi, Mühendislik Fakültesi, Elektronik ve Haberleşme Mühendisliği Bölümü, Kocaeli, TÜRKİYE

[2]Siirt Üniversitesi, Mühendislik-Mimarlık Fakültesi, Mekatronik Mühendisliği Bölümü, Siirt, TÜRKİYE
E-mail: melihkuncan@siirt.edu.tr

Received: 1 October 2016; Accepted: 4 March 2017

Abstract: In this work we deal with the enterpolation of B-spline curves to fiven data points. B-spline curves are generated and compared with the given data points by various parameterization methods. To perform B-spline curve interpolation on the input data, the parameterization and the node vector must be generated using the input data. For parameterization purposes, uniform, chord length, centripetal, Foley, universal and similar methods have been developed. The uniform method gives good results if the data points are regular. Chord-to-beam parameterization can produce undesirable oscillations in long chords. Therefore, the centripetal method has been developed which operates according to the square root of the chord distance. In this study, these methods were compared with different data sets.

Key words: B-spline, interpolation, parameterization.

1. Introduction

B-spline techniques for curves and surfaces were proposed in the early 1940s and were developed by Rich Riesenfeld in the 1970s. The B-spline structure is a generalized version of the Bezier curves developed by Pierre Bezier. The letter "B" refers to the word "basis" [1].

B-spline curves have been developed to address the following disadvantages in Bezier curves

- The grade of the Bezier curve depends on the number of control points.
- Bezier curves only provide global control, not local control.
- While Bezier is easy to maintain C^1 continuity of curve segments, it is insufficient to maintain continuity C^2.

B-spline curves provide local control. That is, the shifted control points change the neighborhoods affected by the control point only. In addition, B-spline curves can provide continuity of the curved parts at the desired level [1]. For example, when two curve segments C^2 are combined with continuity, it is desirable that the first and second derivatives of the merging points of the curves are equal. If C^n continuity is desired at the junction of two curves, both curves must be polynomials at n. degree.

B-spline curves are defined by control points and are used to approximate a targeted set of points or surfaces. Also, a parameter space, which is expressed as a node vector that is defined independently of the length of the points, is needed. The node vector may be uniformly uniform, or it may be defined as a nonuniform distribution with a variety of methods to approximate the target points.

2. Recursive Computation of B-Spline Base Functions

Computer-based B-spline curve computations use the Cox-de Boor algorithm, which recursively computes with respect to the input of the node vector. A sample B-spline curve at the p-th order is defined as follows:

$$C_{(u)} = \sum_{i=0}^{n} N_{i,p}(u) P_i \tag{1}$$

In this definition, P_i denotes control points, whereas $N_{i,p}(u)$ denotes p-th degree B-spline basis functions. The U vector consists of continuously increasing real numbers that operate independently of the object space and are called the node vector.

Each u_i element of the U vector is called a node. Under these definitions, the i-th base function of B-spline at the p-th grade is expressed in a computerized manner with the Cox-de Boor algorithm as follows:

$$N_{i,0}(u) = \begin{cases} 1, & u_i \le u \le u_{i+1} \\ 0, & diğer \end{cases}$$

$$N_{i,p}(u) = \frac{u - u_i}{u_{i+p} - u_i} N_{i,p-1}(u) + \frac{u_{i+p+1} - u}{u_{i+p+1} - u_{i+1}} N_{i+1,p-1}(u) \tag{2}$$

3. B-spline curve interpolation

Bezier and B-spline curves work in computer graphics, animation applications and CAD-CAM surface modeling stages, according to the control points and node vector data from the designer. However, in reverse engineering applications and for data interpolation purposes, this process must be done in a inverse. In this case, it is desirable to generate the control points and the necessary node vector, while providing point data to enter the curve or the surface. At this stage, the operations are reversed. In Fig. 1, the node vector space and the independent state of the object space are given.

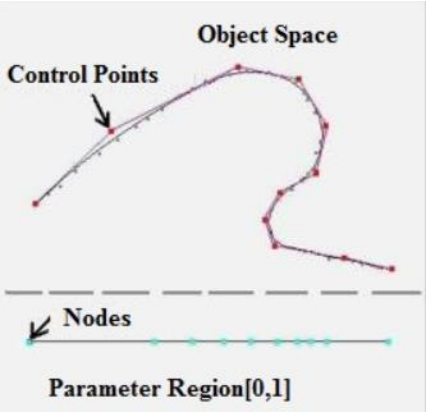

Fig. 1. Parameter space and independence of object space

The equation for the B-spline curve is given as:

$$C_{(u)} = \sum_{i=0}^{n} N_{i,p}(u) P_i \tag{3}$$

In terms of parameterization, the value of the point to be calculated for each parameter value on the node vector is expressed as follows:

$$D_k = C\left(t_k\right) = \sum_{i=0}^{n} N_{i,p}(t_k) P_i, \quad 0 \le k \le n \tag{4}$$

The values of the base functions in the parameter values are written in the matrix N:

$$N = \begin{bmatrix} N_{0,p}(t_0) & N_{1,p}(t_0) & N_{2,p}(t_0) & \cdots & N_{n,p}(t_0) \\ N_{0,p}(t_1) & N_{1,p}(t_1) & N_{2,p}(t_1) & \cdots & N_{n,p}(t_1) \\ \vdots & & & \ddots & \vdots \\ N_{0,p}(t_n) & N_{1,p}(t_n) & N_{2,p}(t_n) & \cdots & N_{n,p}(t_n) \end{bmatrix} \tag{5}$$

The computed D destination points and the P control points are expressed in matrix form as follows:

$$D = \begin{bmatrix} d_0 \\ d_1 \\ \vdots \\ d_n \end{bmatrix}, \quad P = \begin{bmatrix} p_0 \\ p_1 \\ \vdots \\ p_n \end{bmatrix} \tag{6}$$

While the control points are given, in the forward direction calculation, the B-spline curve equation is expressed in matrix form as follows:

$$D = N.P \tag{7}$$

For curve interpolation operations where the control points are to be calculated, the following steps are taken to obtain the P control points:

$$D = N.P \tag{8}$$

$$N^T D = N^T N P$$

$$P = \left(N^T N\right)^{-1} \left(N^T D\right)$$

4. Data Parameterization Methods

In B-spline interpolation and approximation problems, a set of points is given as input. If it is assumed that the node vector changes at [0,1], then some of the cut-off parameters in this range are required for the stoppages to correspond to the data points in the input set. For $D_0,...D_n$ data points, the unit parameter value is defined in the $t_0,...t_n$ region. If $C(u)$ is defined as a curve passing through all the data points, $D_k = C(t_k)$ is for the k values, $0 \le k \le n$ at the cut-off points. Fig. 2 shows how parameters are associated with data points.

Selection of parameter values includes uncertainty and there are infinitely many alternatives. However, careless selection of parameter values can cause undesirable shapes and fluctuations to be generated.

During the parameterization phase, various methods called uniform, chord length, centripetal, universal are used.

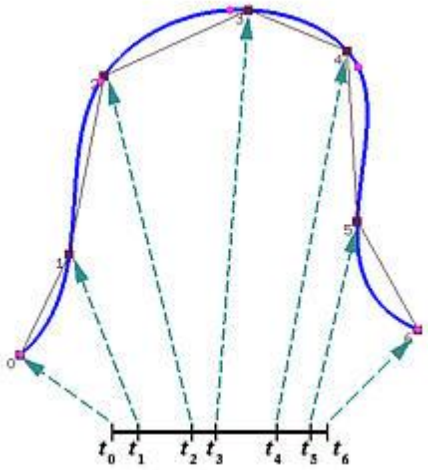

Fig. 2. Parameters and corresponding data points [8]

4.1. Uniformly distributed parameterization

Uniformly distributed parameterization is the simplest method for assigning parameters to given input data points. If it is assumed that parameters are to be distributed in the range [0,1], and if this range of pieces of input is considered to be divisible, then the parameters are defined as follows:

$$t_0 = 0,$$

$$t_i = \frac{i}{n}, \quad 1 \le i \le n-1, \tag{9}$$

$$t_n = 1$$

4.2. Parameterization according to chord length

If the distances between input data points are irregularly distributed, the chord-length method works better than uniform parameterization.

Given $D_0, D_1, \ldots D_n$ data points. The distance between point D_{i-1} and point D_i is expressed by $|D_i - D_{i-1}|$. In this case, the sum of the beam distances between all data points is expressed as:

$$L = \sum_{i=1}^{n} |D_i - D_{i-1}| \tag{10}$$

In this case, the chord length ratio from point D_0 to point D_k is expressed as follows:

$$L_k = \frac{\sum_{i=1}^{k} |D_i - D_{i-1}|}{L} \tag{11}$$

In the normalized case, assuming that parameterization has been performed in the range [0,1], the distribution is as follows.

$$t_0 = 0, \quad t_k = \frac{1}{L} \sum_{i=1}^{k} |D_i - D_{i-1}|, \quad t_n = 1 \tag{12}$$

4.3. Centripetal method

Lee proposed a centripetal parameterization. In the case of a car driving on a racetrack, it is desirable that the centrifugal force (or normal force) be very high in sharp turns when driving on a piste. For a safe ride, Lee suggests that along the way the centrifugal force must be proportional to the change in angle. The centripetal method presents this model approach. This model can be seen as an improved version of the chord length method [2].

$D_0, D_1, \ldots D_n$ data points are given. If the base factor is defined as $e = 1/2$, the distance between point D_{i-1} and point D_i is denoted by $|D_i - D_{i-1}|^e$. Kiriş- In the chord method, this expression was used topless. In this case, the length of the entire data polygon is expressed in terms of the centripetal metric as follows:

$$L = \sum_{i=1}^{n} |D_i - D_{i-1}|^e \tag{13}$$

The ratio of the data beam length from point D_0 to point D_k to the total beam length is expressed as follows.

$$L_k = \frac{\sum_{i=1}^{k} |D_i - D_{i-1}|^e}{L} \tag{14}$$

In the normalized case, assuming that parameterization is performed in the range [0,1], the values are distributed in the following manner.

$$t_0 = 0$$

$$t_k = \frac{1}{L}\sum_{i=1}^{k}|D_i - D_{i-1}|^e \qquad (15)$$

$$t_n = 1$$

4.4. Universal method

Lim proposed a method that differs from other methods in 1999. In the previous methods, the new proposed method is based on calculating the parameter values from the uniformly distributed clamped node vector, while the node vector is generated from these parameter values after the parameter values are determined [3].

In the Lim method, base functions are generated, starting from a uniformly distributed node vector. The peak values of these base functions are considered as input to the parameter list. Although this method produces more natural-looking curves than previous methods, it produces undesirable oscillations in some cases [3].

Suppose that we wanted to generate the necessary parameter values for $n+1$ data points using B-spline at p. $m = n + p + 1$, the number of elements in the node vector is $m+1$. In this case a uniformly distributed, clamped-clamped node vector is obtained as:

$$u_0 = u_1 = ...u_p = 0, \quad u_{p+i} = \frac{i}{n-p+1} \quad i = 1,2,...,n-p, \quad u_{m-p} = u_{m-p+1} = ...u_m = 1 \qquad (16)$$

4.5. Foley-Nielson method

This method was proposed by Foley and Neilson. While the previous methods use the beam spacing between data points, the Foley-Nielson method adds an account between the adjacent points. This method uses the Nielson scale to measure the distance between points. On this count, geometry does not change when it enters rotation, translation and scaling operations. The transformed B-spline curve can be obtained from transformed data points [4].

$m = 2$, when working with two-dimensional data points, the coefficient matrix $Q = \{q_{ij}\}$, $i, j = 1,2$ is defined as:,

$$q_{11} = \frac{V_y}{g}, \; q_{22} = \frac{V_x}{g}, \quad q_{12} = q_{21} = -\frac{V_{xy}}{g}, \quad g = V_x V_y - (V_{xy})^2$$

$$V_x = \frac{\sum_{i=0}^{n}(x_i - \bar{x})^2}{n+1}, \qquad (17)$$

$$V_y = \frac{\sum_{i=0}^{n}(y_i - \bar{y})^2}{n+1},$$

$$V_{xy} = \frac{\sum_{i=0}^{n}(x_i - \bar{x})(y_i - \bar{y})}{n+1}$$

$$\bar{x} = \frac{\sum_{i=0}^{n} x_i}{n+1}, \quad \bar{y} = \frac{\sum_{i=0}^{n} y_i}{n+1}$$

In this case, the Neilson distance between points U and V is defined as:

$$M[P](U,V) = \sqrt{(U-V)Q(U-V)^T} \tag{18}$$

According to the computed Neilson distance, if chord distance parameterization is performed, affine-invariant parameterization can be obtained which can be applied to transformations. In the Foley parameterization, the Δt_i parameter step is defined as:

$$\Delta t_0 = d_0\left[1+\frac{3\hat{\theta}_1 d_1}{2(d_0+d_1)}\right], \qquad \Delta t_{n-1} = d_{n-1}\left[1+\frac{3\hat{\theta}_{n-1} d_{n-2}}{2(d_{n-2}+d_{n-1})}\right]$$

$$\Delta t_i = d_i\left[1+\frac{3\hat{\theta}_i d_{i-1}}{2(d_{i-1}+d_i)}+\frac{3\hat{\theta}_{i+1} d_{i+1}}{2(d_i+d_{i+1})}\right], \qquad i=1,2....,n-2 \tag{19}$$

$$d_i = M[P](P_i,P_{i+1}), \quad \hat{\theta}_i = \min(\theta_i, \pi/2)$$

$$\theta_i = \pi - \arccos\left[\frac{d_{i-1}^2 + d_i^2 + M^2[P](P_{i-1},P_{i+1})}{2d_i d_{i-1}}\right]$$

Here, θ_i is also an affine invariant angle, which is calculated by Neilson distance and is not affected when it enters transformations. In Fig. 3, the notations used in the Foley method are given..

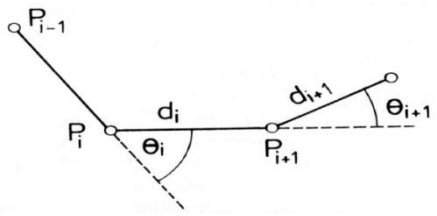

Fig. 3. Parameters used in the Foley method [5]

4.6. Node vector production

After the parameter values are generated, the node vector is generated from these values. Assuming we have $n+1$ parameter values defined in $t_0, t_1, ...t_n$ and we use p th degree B-spline fragments, we need $m+1$ node values, defined as $m = n+p+1$ shaped. If the curve is defined as clamped, the first $p+1$ node value is 0. And the last $p+1$ knot value becomes 1. The $n-p$ nodes in the middle are uniformly distributed according to various methods.

If uniform parameterization is used, the median terms are divided into $n-p+1$ pieces.

$$u_0 = u_1 = ...u_p = 0$$

$$u_{j+p} = \frac{j}{n-p+1}, \qquad j=1,2,...,n-p \tag{20}$$

$$u_{m-p} = u_{m-p+1} = ...u_m = 1$$

5. Applications

The first dataset interpolated in Fig. 4 is taken from the work of Irvine et al. This data can be problematic for interpolation methods due to sudden directional changes and sparse data points [6].

Table 1. The maximum deviation table from the beam along the curve piece, 1. Dataset

Method	1	2	3	4	5	6	7	Average	RMS	Max. Deviation	Time (ms)
Uniform	0.1918	0.0889	0.4133	0.1647	0.4564	0.1964	0.2765	0.255	0.2843	0.4564	49,860
Chord	1.7113	0.5507	0.0524	2.877	0.3785	0.061	2.304	1.133	1.5569	2.877	50,739
Universal	0.102	0.047	0.4007	0.1642	0.3667	0.2513	0.1360	0.2097	0.2439	**0.4007**	135,781
Foley	0.0988	0.1354	0.2475	0.728	0.0976	0.0909	0.5904	0.2840	0.3753	0.728	77,506
Centripetal	0.2135	0.1952	0.1777	0.7214	0.0832	0.0906	0.6385	0.3028	0.3889	0.7214	**49,789**

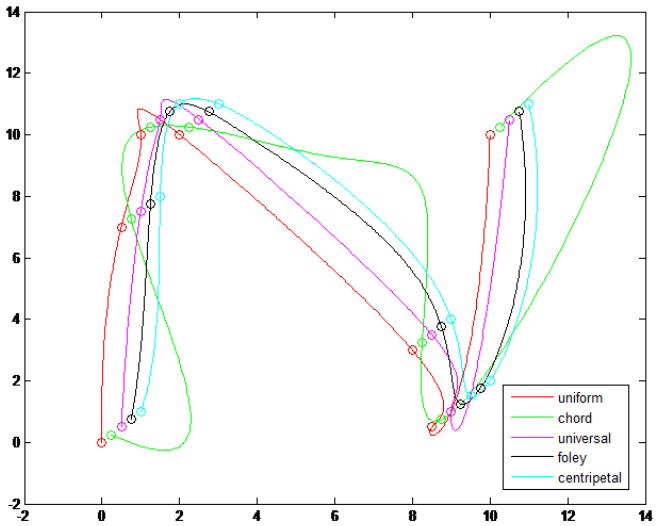

Fig. 4. Cubic Curves Produced by Various Parameterization Methods, 1. Dataset

Fig. 5 shows the cubic B-spline curves generated by the various methods of parameterization for the second dataset. The second data set I in Fig. 5 was taken without the same operation as the first data set. There are also sudden changes in direction and rare data difficulty similar to Larry Irvine et al [6].

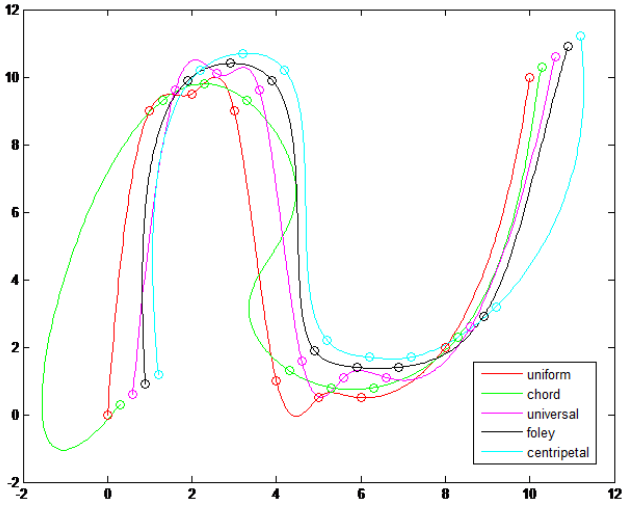

Fig. 5. Cubic Curves Produced by Various Parameterization Methods, 2. Dataset

Table 2. The maximum deviation table from the beam along the curve piece, 2. Dataset

Method	1	2	3	4	5	6	7	8	Average	RMS	Max. Deviation	Time (ms)
Uniform	0.209	0.259	0.473	0.049	0.482	0.152	0.35	0.376	0.2938	0.3271	**0.4733**	50,461
Chord	1.847	0.118	0.106	0.841	0.067	0.053	0.259	0.431	0.4652	0.7420	1.847	**49,805**
Universal	0.18	0.442	0.367	0.054	0.476	0.193	0.519	0.256	0.3109	0.3471	0.5187	133,821
Foley	0.59	0.12	0.161	0.269	0.141	0.031	0.345	0.199	**0.2319**	0.2829	0.5895	76,887
Centripetal	0.667	0.109	0.177	0.231	0.134	0.051	0.191	0.802	0.2952	0.3940	0.8024	52,574

The third set of data in Fig. 6 is taken from the work of Fritsch and Carlson. Sudden distance changes are tested here [7].

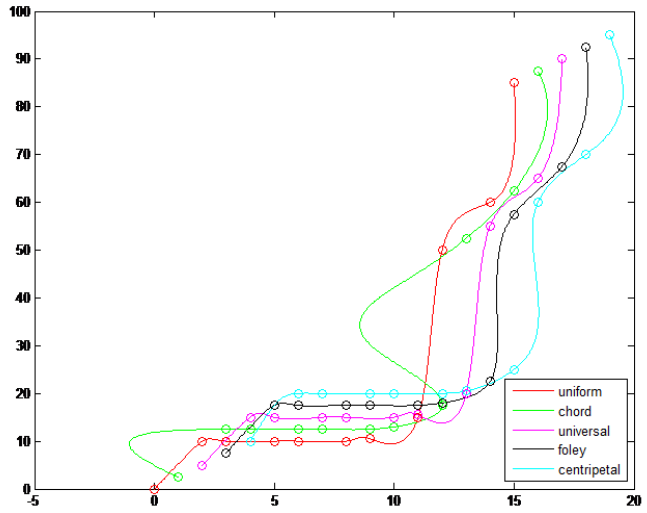

Fig. 6. Cubic Curves Produced by Various Parameterization Methods, 3. Dataset

Table 3. The maximum deviation table from the beam along the curve piece, 3. Dataset

Method	1	2	3	4	5	6	7	8	9	10	Average	RMS	Max. Deviation	Time (ms)
Uniform	0.123	0.359	0.142	0.078	0.185	0.337	1.168	0.19	0.652	0.651	0.3885	0.506	1.168	**46,438**
Chord	3.347	0.057	0.011	0.008	0.082	0.053	0.583	3.915	0.238	0.806	0.91	1.661	3.915	49,580
Universal	0.169	0.447	0.366	0.162	0.234	0.361	1.246	0.212	0.324	0.469	0.399	0.499	1.246	135,65
Foley	0.164	0.354	0.111	0.131	0.079	0.057	0.516	0.412	0.13	0.597	0.255	0.316	**0.597**	75,379
Centripetal	0.505	0.045	0.027	0.001	0.04	0.105	0.268	0.741	0.305	1.096	0.3132	0.467	1.096	49,11

The fourth data set in Fig. 7 was taken from the work of Boeing employee ETY Lee [2]. Here, there are more data points near the corners.

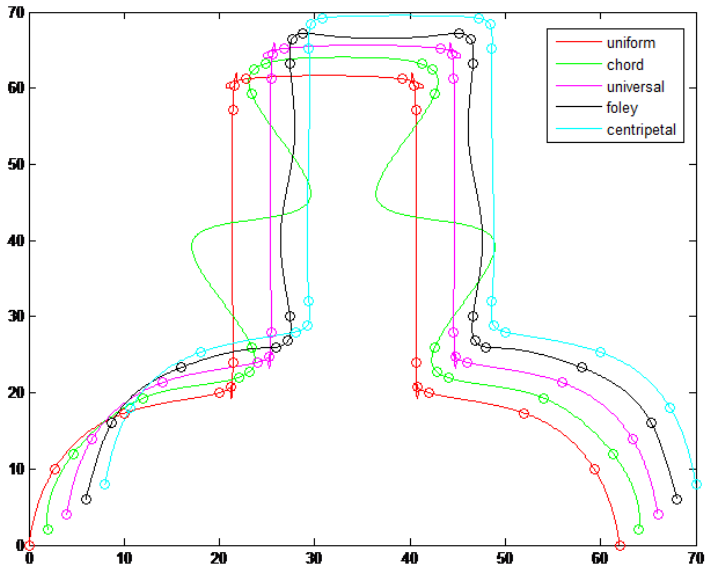

Fig. 7. Cubic Curves Produced by Various Parameterization Methods, 4. Dataset

Table 4. Maximum deviations table from the beam along the curve piece, 4. Dataset

Method	Uniform	Chord	Universal	Foley	Centripetal
1	0.4593	0.8607	0.4602	0.2704	0.3944
2	0.9257	0.6698	0.9127	1.011	0.9574
3	0.225	0.2848	0.2747	0.5958	0.2614
4	0.109	0.8897	0.1558	0.1798	0.1449
5	0.1584	0.4455	0.1461	0.1909	0.1756
6	0.1879	5.224	0.2024	0.999	0.2223
7	0.0998	0.4396	0.1009	0.1437	0.1264
8	0.3779	0.084	0.3907	0.2422	0.1928
9	0.4538	0.8721	0.4598	0.6513	0.3511
10	0.3885	0.08393	0.3903	0.2422	0.1928
11	0.06689	0.4396	0.092	0.1441	0.1278
12	0.1419	5.224	0.2029	0.9916	0.2105
13	0.1518	0.4433	0.1539	0.1937	0.1756
14	0.1074	0.07757	0.1617	0.1655	0.1449
15	0.2171	0.2919	0.2754	0.5958	0.2614
16	0.9257	0.6717	0.9088	1.011	0.9574
17	0.457	0.8607	0.4524	0.2782	0.3944
Average	**0.2830**	1.0508	0.3377	0.4651	0.2718
RMS	0.4111	1.8705	0.4148	0.5741	0.3991
Max. Deviation.	0.9257	5.224	**0.9127**	1.011	0.9574
Time (ms)	44,255	**43,387**	127,132	69,769	**43,429**

6. Conclusion

In order to be able to interpolate input data with B-spline curves, it is necessary to parameterize the data in the first step. Various methods are used to parameterize the input data. Commonly used methods are uniform uniform parameterization, chord length, universal parameterization, Foley angle parameterization centripetal methods.

The uniform method provides good results if the data points are regular. According to the chord distance, parameterization can produce unwanted oscillations in long beams. Therefore, the centripetal method has been developed which operates according to the square root of the beam spacing. The Foley method, on the other hand, has been successful in providing sharp rotations due to the addition of angle values.

In this study, basic parametrization methods are tested for different data sets and the obtained curves and error measurements are given in Tables 1, 2, 3 and 4 with Figures 4, 5, 6 and 7. From these data sets, it was observed that for the first three data sets, the centripetal-centric method succeeded from the other methods and the performance approaches the Foley angle method. For the fourth data set containing intense data at the corners, the centripetal method was observed to be more successful.

In case of sudden change of the beam length between data points, the centripetal method that works according to the square root of the beam distance is preferred; in the datasets where there are sudden and sharp angular rotations, the Foley method, which adds the angle values, is preferred; In cases where the data are uniformly distributed, the chord-beam distance method would be preferable. Where surface details are insignificant and speed is important, it is seen that uniform methods can be preferred in terms of simplicity in calculations.

Acknowledgment

This project was supported by the Coordinator of BAP Coordination Unit of Scientific Research Projects of Kocaeli University as the project number 2015-018.

References

[1] Solomon, D. *Curves and Surfaces for Computer Graphics*, *Springer*, (2006),

[2] Lee, E. Choosing Nodes in Parametric Curve Interpolation, *Computer Aided Design, vol. 21, no. 6*, (1989), sayfa 363-370.

[3] Lim, C. G. A Universal Parameterization in B-spline Curve and Surface Interpolation, *Computer Aided Geometric Design 16*, (1999), sayfa 407-422.

[4] Foley, T.A., & Nielson, G.M. Knot selection for parametric spline interpolation. Mathematical methods in computer aided geometric design. *Academic Press Professional, Inc*, (1989), sayfa 261–72.

[5] Hoschek, J. & Lasser, D. *Computer Aided Geometric Design*, *A K Peter, Ltd.* (1993)

[6] Irvine, L., Marin, S., & Smith, P. Constrained Interpolation and Smoothing, *Constructive Approximation, Volume 2, Number 1*, (1986), sayfa 129-151.

[7] Fritsch, F., & Carlson R. Monotone Piecewise Cubic Interpolation, *SIAM Journal on Numerical Analysis, Volume 17, Number 2*, (1980), sayfa 238-246.

[8] Piegl, L., & Tiller, W. The NURBS Book, *Springer*. (1997),

Vol 7, Number 1, 2017
European Journal of Technic
EJT

EXPERIMENTAL AND ARTICIAL NEURAL NETWORK BASED STUDIES ON THERMAL CONDUCTIVITY OF LIGHTWEIGHT BUILDING MATERIALS

[1]Davut Sevim, [2]Şehmus FİDAN*, [3]Süleyman POLAT , [4]Hasan OKTAY

[1]Batman University Vocational School

*[2]Batman University Engineering Faculty Department of Electric-Electronic Engineering Batman

[3]Batman University Engineering Faculty Department of Geology Engineering Batman

[4]Batman University Engineering Faculty Department of Mechanical Engineering Batman

* Corresponding author; sehmus.fidan@batman.edu.tr

Received: 15 November 2016; Accepted: 2 April 2017

Abstract:

The growing concern about energy consumption of heating and cooling of buildings has led to a demand for improved thermal performances of building materials. In this study, an experimental investigation is performed to predict the thermal insulation properties of wall structures of which the mechanical properties are known; by using Levenberg-Marquardt training algorithm based artificial neural network (ANNs) method for energy efficient buildings. The produced samples are cement based and have relatively high insulation properties for energy efficient buildings. In this regard, 102 new concrete samples and their compositions are produced and their mechanical and thermal properties are tested in accordance with ASTM and EN standards. Then, comparisons have been made between the experimental results and the ANN predicted results. It can be concluded that thermal performance of lightweight materials could be predicted with high accuracy using artificial neural network approach.

Key words: *Concrete, thermal properties, mechanical properties, ANN, energy efficient building*

1. Introduction

A great amount of energy consumption is expended through building heating and cooling. It is mandatory to minimize consumption of energy which directly affects energy sources by means of economic and environmental values. The temperature of the living environment which is the one of the most important comfort conditions varies with the surrounding the structure of walls and ceilings as a result of interaction with external atmospheric conditions such as wind speed, solar radiation and the ambient temperature [1]. It is possible to keep the changing temperature in the comfort zones by heating and cooling air within a space. For this reason, it is necessary to heat the living spaces in winter season by giving sufficient amount of moisture, and to cool the spaces in summer season. That is, heating ventilating and air conditioning (HVAC) system has been the most important solution for a more comfortable life. Because capacities of the HVAC systems greatly depend on the types of the walls and roofs used, which are responsible for a major fraction of heat loss or gains for the heating or cooling loads due to their large surface area in many buildings [2]. It is critical both to improve the thermal performance of these structures and to improve thermal comfort of the occupants in terms of reducing the energy use.

In order to describe the thermal performance of the building structures, many studies have been conducted to identify the dynamic thermal characteristics of the components which indicate the magnitude of heat loss and gains through building structures under periodic boundary conditions and are influenced by the effective parameters, which can be categorized as environmental parameters (ambient air temperature, solar heat flux, ventilation etc.), design parameters (orientation, solar absorptivity, emissivity etc.) and thermophysical properties (thermal conductivity, specific heat, density, thickness etc.) [3]. Many investigations declared that those characteristics strongly depend on the thermal conductivity of the building's layer materials [4–11]. Besides, the thermal conductivity of a building wall or roof material are strongly affected by microstructure, mineralogical composition, proportion, supplementary materials, moisture content, and porosity, as shown in Fig. 1. Furthermore, these structures also need to have suitable mechanical properties because they must stand without being damaged from natural causes for many years. Therefore, if these structures having appropriate thermal and mechanical properties are selected, also accurate cooling load calculation is performed, and then suitable HVAC system components can be selected in terms of reducing the energy use. However, it is difficult to determine the ideal thermal conductivity properties of these structures by means of both energy and time efficiency due to the accuracy of test methods and high price of the devices. Hence, this situation leads scientists to search for new solutions.

The mathematical models which are used to describe experiences gathered from data of concrete mixes behaviors are most reliable and accurate as well as recommended methods [13]. These models based on experimental data are generally in regression forms, and called ‘‘Free models” [14]. However, because of more assumptions and less accuracy in regression form, regression methods cannot be used when the problem contains many independent variables. Recently many new modeling methods such as artificial neural networks (ANN), expert systems as a free model can approximate complex and non-linear relation due to any parameters and trial and error process by learning real record relationship without any presumptions [15]. Artificial neural networks (ANN) are a family of massively parallel architectures that produces meaningful solutions to the problems and capable of learning and generalization of examples and experiences, even if the input data is incorrect or incomplete. ANN is a powerful tool to solve for some complex engineering problems.

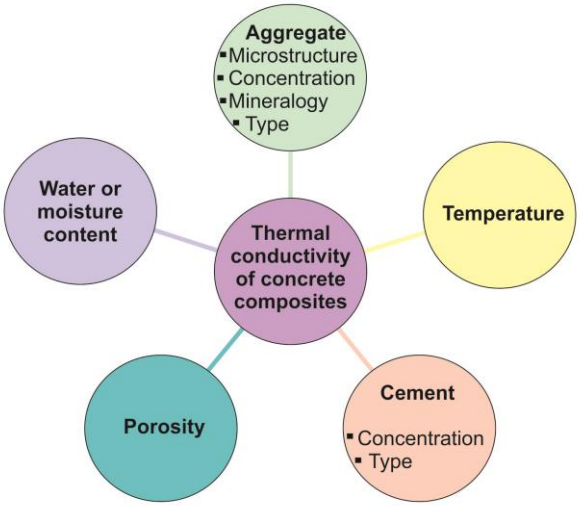

Fig.1. Parameters affecting thermal conductivity of structures[12]

The basic strategy for developing a neural network-based model for material behavior is to train a neural network on the results of a series of experiments using that material. If the experimental result contains relevant information on the behavior of the material, the neural network training will contain sufficient information on the behavior of a material to qualify as a model material [16]. This learning of the neural network not only be able to reproduce the experimental results, but would be able to bring the results of other experiments by the generalization ability.

In the literature, the ANN has been used to predict the effect of material behavior, especially on mechanical properties. Marai M. Alshihri et al. [15] are used the neural networks (NNs) to predict the compressive strength of light weight concrete (LWC) mixtures after 3, 7, 14, and 28 days of curing. The finding of this study indicated that the neural networks models are sufficient tools for estimating the compressive strength of LWC. Furthermore, Guang and Zong, [17] proposed a method to predict 28-day compressive strength of concrete using multilayer feed-forward neural networks. Dias, [18] presented an artificial neural network model for predicting the strength and slump of ready mixed concrete. Eldin and Senouci, [19] employed a neural network for measuring and predicting of the strength of rubberized concrete. Lai [20] predicted the mechanical properties of concrete by ANNs. Moreover, Gencel et al [21] predicted the thermal conductivity of concrete with vermiculite by using artificial neural networks approaches with 20 datasets. The root mean square error, the mean absolute error, and determination coefficient statistics are used as evaluation criteria of the models, and the experimental results are compared with these models.

Therefore, this research aimed to produce new concrete types in order to develop a lightweight construction material with higher thermal insulation property and to predict ideal thermal conductivity values of those produced concrete wall or roof structures by using an ANN method so as to reduce the energy consumption of the buildings. The composite materials were manufactured by reinforcing varying volume fraction of lightweight aggregates in cementitious matrix, which were exposed to the same conditions. The test program was conducted mainly to investigate the effect of pumice (PA), rubber aggregates (RA) and expanded perlite (EPA) on the thermal property of samples by using thermal response method. After experimental test program, an artificial neural network (ANN) method, which is Levenberg-Marquardt algorithm, is constructed for the prediction of thermal conductivity of concretes

of which the mechanical properties are known. Then, the actual experimental results were compared with the predicted results. The findings and results are presented in detail in the following sections.

2. Experimental Procedure Instructions

2.1. Concrete Mixtures, Materials and Test Methods

Several materials were used to obtain different lightweight building elements. The materials were locally available ordinary Portland cement (PC) (CEM I 42.5R), silica fume (SF), fine aggregate, coarse aggregate, RA, PA, EPA and superplasticizer (SP). Both river sand and uncrushed gravel were employed as the fine and coarse aggregates, respectively. Crumb rubber consisting of particles ranging in a size from 4.75 mm to 0.075 mm was generated from waste tire without steel fibers with a cracker mill process. Perlite is a siliceous volcanic glass, whose volume can expand substantially under the effect of heat. When it is heated above 870 ºC, its volume increases 4–20 times of the original volume [22]. Pumice is a porous volcanic rock with amorphous structure and composed mainly of SiO_2. It is widely used in many industries [23]. Due to their low density and high thermal and sound insulation capacity, both pumice and expanded perlite are suitable materials to produce lightweight concrete (ASTM C330/330M, ASTM C 332). In accordance with ASTM C136, the gradation of aggregates was selected to be ideal region depending on the maximum grain size. Due to the fact that the gradation of aggregates has a significant impact on the property of the concrete composition, in this study, single and uniform grain size was used, as shown in Fig. 2.

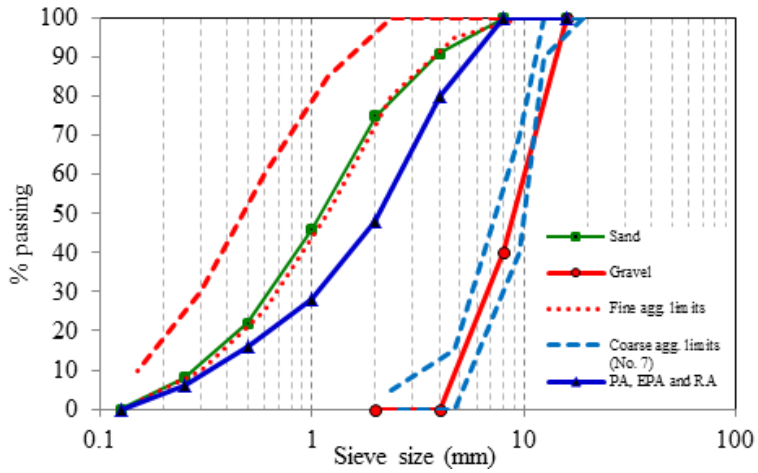

Figure 2. Sieve analyses of aggregates

Concrete mixtures were designed to have a constant water–cementitious material ratio (w/c) of 0.48 and total cement content of 350 kg/m^3. Normal aggregates were replaced by PA, EPA and RA at different volume fractions vary between 10% and 50%. In total, 102 concrete samples were produced and their mechanical tests which are the compressive strength, bulk density, porosity are performed on air dry samples aged 28 days. The compressive strength test was carried out in accordance with ASTM C39 at a loading rate of 0.24 MPa/s on 100 x 100 x 100 mm cube specimens by a testing machine with a maximum capacity of 3000 kN. The thermal conductivity test was performed on same state with the age of 35 days according to EN 12667. In this study, ISOMET 2104 device (Fig. 3) was used to measure

thermal conductivity of concrete samples on the basis of TPS method and the values of the device ranges for the measured parameters are presented in Table 1. In the TPS technique, the source of heat is a hot disc made out of a bifilar spiral, which also serves as a sensor for temperature increase in the samples. In comparison with stationary or steady state methods, the advantage of transient methods is that some of them give a full set of thermophysical properties within a single rapid measurement. All test result measurement values presented in the tables are based on the average values ± a tolerance limit (less than 4%) in order to cover the range of all properties as measured for different samples of the same category.

Table 1. Values of device range for measuring parameters

Measurement	Measurement range	Accuracy
Thermal conductivity coefficient	0.015–6 W/m K	5 % of reading + 0.001 W/m K
Specific heat capacity	4 x10^4 – 4 x10^6 J/m^3 K	15 % of reading + 1.103 J/m^3 K
Operating temperature	From -20 – +70 °C	1°C

Fig. 3. The thermal property measurement device used in this study.

3. Construction of Neural Network Model and Parameters

Neural networks algorithm is extremely useful tool for solving complex engineering problems especially recognizing patterns, fitting a function and clustering of data. Basic ANN structure has three inputs, hidden and output layer. Connection between all layers is achieved by weights that show how strong the connection is between layers. All input neuron cell node collect data from world and multiplies by a weight. The neuron will combine these inputs with reference to a threshold value and activation function. There are number of activation functions in use with ANN such as logistic or hyperbolic tangent function. In training process, the error between experimental result of sampled concrete and output was evaluated. The calculated error was propagated backward through the neural network layers, and every neuron weights are updated, it can be described a neuron by the following equations:

$$o = f\left(wx + bias\right) \quad (1)$$

where w and x defines weights and input that defines

$$w = w_1, w_2, \ldots, w_n \quad (2)$$

$$x = x_1, x_2, \ldots, x_n \quad (3)$$

The transfer function:

$$net = \sum_{i=1}^{n} w_i x_i + b \quad (4)$$

Bias, b has the effect of increasing or decreasing the net input of the activation function. On the field artificial neural network, the sigmoid function is a type of activation function and is used excessively in neural networks application. Sigmoid function which refers to the special case of the logistic function is defined by the formula:

$$C_j = f\left(net_j\right) = \frac{1}{1+e^{-(net)}} \quad (5)$$

In this study, ANN architecture was designed as an input layer with 4 neurons and an output layer with one neuron, where every layer in network has 3-5-4 neurons; respectively. Data collected from experimental setup were divided into two parts: training and testing. Matlab – Neural Network Toolbox was used for design, train and simulate. It provides user-friendly and simple graphical user interface(nntool GUI) to efficiently design of several neural network. Using this program, a neural network model was constructed, trained and tested using the available test data of 102 different concrete samples gathered from experimental setup. The data used in neural network model are arranged in a format of four input parameters that cover the bulk density, porosity, compressive strength, and the percentage of aggregate content (%). A basic neural model where consist of 4 inputs and a single output used in this study as shown in Fig. 4.

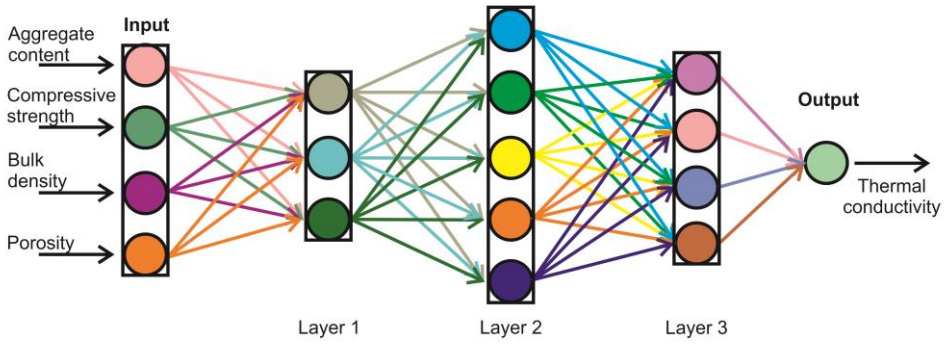

Fig. 4. Structure of ANN model used in this study

In ANN model, Levenberg–Marquardt (LM) algorithm was selected as learning algorithm. Since there is no best option to select number of hidden layer and neurons, several combinations were tried. After trial procedure, optimal results were obtained with 3-5-4 neuron structure, respectively. The quality and speed of training process could improve using normalization that shown by the following formula:

$$x_i = \frac{X - X_{min}}{X_{max} - X_{min}} \quad (6)$$

where x, x_i, x_{max} and x_{min} are original, normalized, maximum and minimum values, respectively.

4. Result and Discussion

The results of the experimental tests gathered from the mechanical and thermal properties of AEC, PC, EPC and RC and mixtures prepared, in contrast with the control mixture, NC are shown in Table 2.

Table 2. Mechanical and thermal properties of produced concrete wall samples*

Types of concrete	Compressive strength, σ_c (MPa)	Bulk density, ρ (kg m-3)	Porosity, ϕ (%)	Thermal conductivity, λ (W m-1 K-1)
NC	51.85	2345.09	9.69	1.96
AEC	48.11	2288.86	8.41	1.91
EPC10	31.21	2139.09	12.86	1.51
EPC20	19.02	1885.52	18.37	1.22
EPC30	10.01	1559.44	23.28	0.70
EPC40	8.15	1376.56	26.12	0.50
EPC50	4.88	1168.63	28.20	0.36
PC10	33.46	2005.34	11.23	1.54
PC20	23.39	1851.02	16.55	1.29
PC30	13.07	1559.95	22.05	0.76
PC40	9.90	1400.72	24.20	0.54
PC50	9.51	1329.97	27.28	0.41
RC10	42.04	2244.30	9.19	1.72
RC20	30.41	2148.07	11.43	1.44
RC30	19.04	2033.93	12.23	1.22
RC40	9.51	1874.62	14.19	0.89
RC50	4.53	1644.98	16.35	0.62

* These properties are the average of the six specimens for each test.

Various performance indices are used to evaluate the convergence of experimental values in order to predict values. Root mean-square error, mean absolute percentage error, mean absolute error and coefficient of correlation (R^2) are performed in various studies. The mean absolute percentage error (MAPE) and R^2 performance indices were used in this study. The mean absolute percentage error was calculated by following equation:

$$MAPE = \frac{1}{n}\sum_{i=1}^{n}\frac{|o_i - t_i|}{t_i}.100 \quad (7)$$

where t_i is target mean value, o_i is output value and n total data number.

After experimental setup was performed, an artificial neural network (ANN) method, which is Levenberg-Marquardt algorithm, is selected for prediction of thermal conductivity of concretes of which the mechanical properties are known. A comparison between the results of experimental study and ANN predicted values are depicted in Fig. 5. MAPE values of predicted data, which shows the percentage value of absolute error, was calculated as 3.17. The correlation coefficient R^2 was calculated as 0.997. The results indicate that ANN makes good predictions for both training and testing periods. Therefore, it can be concluded that the prediction of the artificial neural network has proceed in the correct manner.

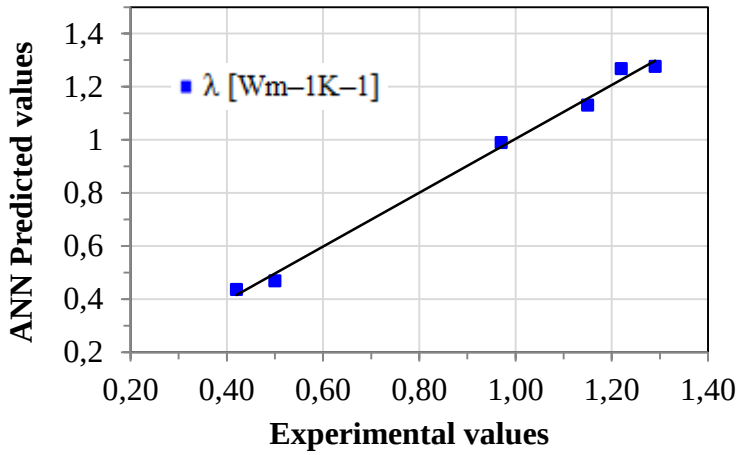

Fig. 5. Correlation between actual (experimental) and ANN results

5. Conclusion

In this study, an experimental investigation is carried out to predict the thermal insulation properties of building wall structures of which the mechanical properties are known, by using an artificial neural network (ANNs) method in order to provide energy efficiency in buildings. Levenberg-Marquardt training algorithm based neural network was designed to predict thermal conductivity properties of lightweight building materials. Since there is no specific rule to determine the number of neurons and hidden layer, the neural network were optimized by trial/error method and the best results were obtained with 3-5-4 hidden layered structure. The value of the mean absolute percentage error (MAPE) 3.17 and correlation coefficient R^2 were calculated as 0.997, respectively. The estimated performance indices show that the error is in acceptable limits. The actual experimental results were compared with the predicted results, ANN estimation is pretty good and can strongly be suggested to decrease time consuming and complicate laboratory experiment.

References

[1] Dağsöz A.K., *et al*., Yapılarda sıcak etkisinin getirdiği problemlerin ısı yalıtımı ile çözümü ve enerji tasarrufu, IV. Ulusal Tesisat Mühendisliği Kongresi ve Sergisi, Izmir, Türkiye, 1999, pp. 329–339.

[2] Bansal K., *et al*., Development of CLTD values for buildings located in Kolkata, India. *Applied Thermal Engineering*, *28* (2008), pp.1127–1137.

[3] Moosavi L., *et al*., Thermal performance of atria: An overview of natural ventilation effective designs. *Renewable and Sustainable Energy Reviews*, *34*, (2014), pp. 654–670.

[4] Zhang Y., *et al*., Exploring buildings' secrets: The ideal thermophysical properties of a building's wall for energy conservation, *International Journal of Heat and Mass Transfer*, *65* (2013), pp. 265–273.

[5] Asan H., Numerical computation of time lags and decrement factors for different building materials, *Building and Environment*, *41* (2006), pp. 615–620.

[6] Asan H, Sancaktar Y. S., Effects of Wall's thermophysical properties on time lag and decrement factor, *Energy and Building*, *28* (1998), pp. 159–166.

[7] Jin X., *et al*., Thermal performance evaluation of the wall using heat flux time lag and decrement factor, *Energy and Building*, *47* (2012), pp. 369–374.

[8] Zhang Y., *et al*., Ideal thermophysical properties for free-cooling (or heating) buildings with constant thermal physical property material, *Energy and Building*, *38* (2006), pp. 1164–1170.

[9] Zhang Y., *et al*., Impact factors analysis on the thermal performance of hollow block wall, *Energy and Building*, *75* (2014), pp. 330–341.

[10] Kontoleon K. J., *et al*., The influence of concrete density and conductivity on walls' thermal inertia parameters under a variety of masonry and insulation placements, *Applied Energy, 112* (2013), pp. 325–337.

[11] Barrios G., *et al*., Wall/roof thermal performance differences between air-conditioned and non air-conditioned rooms, *Energy and Building*, *43* (2011), pp. 219–23.

[12] Khan MI., Factors affecting the thermal properties of concrete and applicability of its prediction models, *Building and Environment*, *37* (2002), pp. 607–614.

[13] Pooliyadda S. P., Dais W. P. S., Neural networks for predicting properties of concrete with admixtures, *Construction Building Materials*, *15* (2001), 7, pp. 371–379

[14] Ramezanianpour A. A., Davapanah A., Concrete properties estimation and mix design optimization based on neural networks, World Conference on Concrete Materials and Structures (WCCNS), Kuala Lumpur, Malaysia, 2002.

[15] Marai M., *et al*., Neural networks for predicting compressive strength of structural light weight concrete, *Construction and Building Materials, 23* (2009), pp. 2214–2219.

[16] Masri S. F., *et al*., Identification of Nonlinear Dynamic Systems Using Neural Networks, *Journal of Applied Mechanics, 60* (1993), pp. 123–133.

[17] Guang N. H., Zong W. J., Prediction of Compressive Strength of Concrete by Neural Networks, *Journal of Cement and Concrete Research, 30* (2000), pp. 1245–1250.

[18] Dias W. P. S., Pooliyadda S. P., Neural Networks for Predicting Properties of Concretes with Admixtures, *Journal of Construction and Building Materials,* 15 (2001), pp. 371–379.

[19] Eldin N. N., Senouci A. B., Measurement and Prediction of the Strength of Rubberized Concrete, *Journal of Cement and Concrete Composites*; *16* (1994), pp. 287–298.

[20] Lai S., Serra M., Concrete Strength Prediction by Means of Neural Network, *Journal of Construction and Building Materials*, *11* 1997, 2, pp. 93–98.

[21] Gencel O., *et al*., Modeling of Thermal Conductivity of Concrete with Vermiculite by Using Artificial Neural Networks Approaches, *Experimental Heat Transfer*, *26* (2013), 4, pp. 360–383, DOI:10.1080/08916152.2012.669810.

[22] Chandra S., Berntsson L., Lightweight Aggregate Concrete, Noyes Publications/William Andrew Publishing, NY, 2002.

[23] Yasar E., Erdogan Y., Strength and thermal conductivity in lightweight building materials, *Bulletin Engineering Geology Environment, 67* (2008), pp. 513–519

HIGH GAIN AND COAX FED MODIFY RECTANGULAR MICROSTRIP ANTENNA DESIGN FOR X BAND APPLICATION

*[1]*İsa ATAŞ, [2]Teymuraz ABBASOV, [3]M. Bahattin KURT, [3]Hüseyin ACAR*

[1] Dicle University, Diyarbakır Vocational School, Diyarbakır, Turkey

[2]İnönü University, Engineering Faculty, Electrical-Electronics Engineering, Malatya, Turkey

[3] Dicle University, Engineering Faculty, Electrical-Electronics Engineering, Diyarbakır, Turkey

*Corresponding author; E-mail: isaatas21@gmail.com

Received: 15 November 2016; Accepted: 2 April 2017

Abstract: *This study presents a design of coax-fed rectangular microstrip antenna operation in different applications within the context of X-bands. High gain and radiation pattern characteristics are obtained by using coax-fed network technique. The Rogers Kappa was chosen as a substrate material for the designed patch antenna with a dielectric constant of 4.38, and a height of 2.4 mm. Simulation results are obtained and examined by using the High Frequency Structure Simulator (HFSS) software. The simulated results indicate the band from 8.2GHz to 11.7 GHz (return loss < −10 dB) and produce a gain of 6.53 dB at 8.7GHz and 11.65 dB at 11GHz, respectively.*

Key words*: microstrip antennas, coax-fed, gain, directivity, high gain.*

1. Introduction

Nowadays, researches on microstrip antenna especially focuses on size reduction, increasing gain, wide bandwidth (BW), multiple functionality and system-level integration [1], [2]. Microstrip Antenna (MA) which are used in many field such as mobil communication, wireless internet, satellite and misille navigation, radar systems and biomedical applications have a good credit in meeting these requirements among the other antenna types [3]. However MA have some disadvantages such as low gain and narrow BW. These bad characteristics of MAs have been tried to improve by using different methods such as choosing special dielectic material, modifying the geometric configuration, etc. MA was firstly mentioned conceptually by Deschamps(1953), and later a patent was taken for a MA by Gutton and Baissinot. Because of not existing of good dielectric substrates, first practical MA was developed by Howel and Munson at the beginning of 1970 [4].

1.1. Feeding Methods

MAs have two feeding techniques. These are contacting and non-contacting feeding. Feeding technique affects the antenna input impedance and radiation characteristics, and therefore, is an important design parameter [5].

1.1.1. Contacting Feeding

In this method, the Radio Frequency power is fed directly to the radiating patch using a microstrip line or coaxial element. Microstrip line feed is one of the easier methods to design and fabricate as it is just conducting strip connecting to the patch and therefore can be considered as extension of the patch [5], [6]. The most important advantage of this method is to maintain its planar structure. By controlling the inset position, solving matching problem is get easier. The disadvantage of this method is that as substrate thickness increases, surface wave and spurious feed radiation increases, which limit the BW for practical designs [3]. Coaxial Probe feed where the inner conductor of the coax is attached to the radiation patch while the outer conductor is connected to the ground plane, are also widely used. Advantages of this method is easy to fabricate and match, and it has low spurious radiation. The disadvantages of this method is having narrow BW and more difficult to model, especially for thick substrates ($h > 0.02\lambda_0$) [3]. For thick substrates, which are generally employed to achieve broad BW, both the above methods of direct feeding the MA have problems. In the case of a coaxial feed, increased probe length makes the input impedance more inductive, leading to the matching problem. For the microstrip feed, an increase in the substrate thickness increases its width, which in turn increases the undesired feed radiation. Also, both the microstrip feed line and the coaxial probe possess inherent asymmetries which generate higher order modes which produce cross-polarized radiation. To overcome these problems, noncontacting (indirect) feeds, discussed below, have been introduced [3], [6].

1.1.2. Non - Contacting Feeding

The electromagnetic coupling is also known as proximity coupling. The feed line is placed between the patch and the ground plane, which is separated by two dielectric media. The advantages of this feed configuration include the elimination of spurious feed-network radiation. The disadvantages are that the two layers need to be aligned properly and that the overall thickness of the antenna increases [3]. Another method for indirectly exciting a patch employs aperture coupling. In the aperture-coupled MA configuration, the field is coupled from the microstrip line feed to the radiating patch through an electrically small aperture or slot cut in the ground plane. Similar to the electromagnetic coupling method, the substrate parameters of the two layers can be chosen separately for optimum antenna performance. This feeding method gives increased BW [6]. We chosen the coaxial probe feed because of its simple to match and easy to fabricate properties. In Fig. 1, proposed coaxial fed MA was shown.

1.2. Methods of Analysis

There are many methods of analysis for MAs. The most popular models are the transmission-line, cavity, and full wave (which include primarily Finite Element, Finite Difference Time Domain, and Moment Method). The transmission-line model is the easiest of all, it gives good physical insight, but is less accurate and it is more difficult to model coupling. Compared to the transmission-line model, the cavity model is more accurate but at the same time more complex. However, it also gives good physical insight and is rather difficult to model. In general when applied properly, the full-wave models are very accurate, very versatile, and can treat complex geometries [3]. In this study, we used High Frequency Structure Simulator [7] (HFSS) which is widely used in antenna design and employ the full-wave finite element method for analyzing the electromagnetic structures.

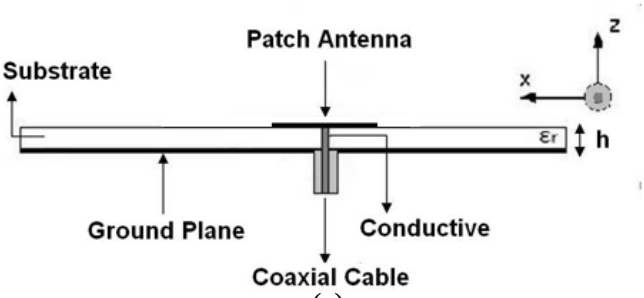

(a)

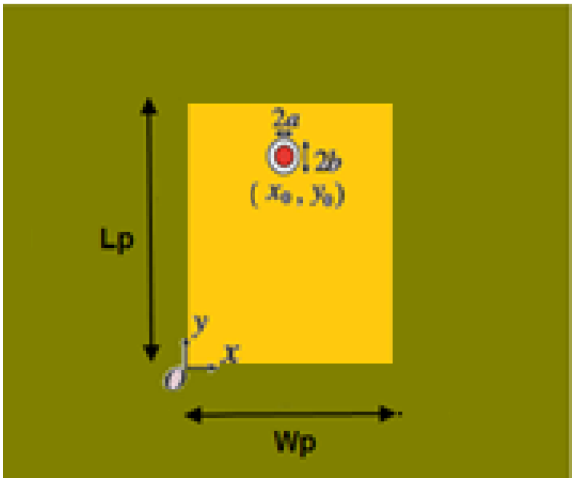

(b)

Figure 1. Coaxial feed microstrip antenna (a) side view (b) top view.

2. Methods

2.1. Design of Rectangular Microstrip Antenna

Microstrip antennas manufactured with printed circuit technology are comprised of a conductor radiating on the upper surface and a ground conductor containing an insulator on the lower surface of the insulating material having a low-loss thin layer [8]. Since the numeric values obtained as simulation results of theoretical calculations are not in desired levels, some parameters are manually changed to achieve appropriate results. "Rogers Kappa-438" is selected as insulating material of the antenna designed in this study and a dielectric constant (ε_r) of 4.38, an insulating copper thickness (t) of 0.035 mm and a dielectric height (h) 2.4mm are taken. Physical parameters of the antenna designed with a center frequency of 10GHz are calculated with equations (1-6) used in transmission line model [3] [6] and demonstrated below.

$$W = c_o \sqrt{\frac{(\varepsilon_r + 1)}{2}} / 2 f_r \tag{1}$$

$$\varepsilon_{eff} = \left[\frac{\varepsilon_r + 1}{2}\right] + \left[\frac{\varepsilon_r - 1}{2}\right] \sqrt{\frac{1 + 12h}{W}} \tag{2}$$

$$\Delta l = 0.412h \frac{(\varepsilon_{eff} + 0.3)(\frac{W}{h} + 0.264)}{(\varepsilon_{eff} - 0.258)(\frac{W}{h} + 0.8)} \tag{3}$$

$$L = \left[\frac{c_o}{2 f_r \sqrt{\varepsilon_{eff}}} \right] - 2\Delta l \tag{4}$$

$$x_0 = \frac{W_p}{2} \tag{5}$$

$$y_0 = \frac{L_p}{2\sqrt{\varepsilon_{eff}}} \tag{6}$$

In the transmission line formula, ε_r is dielectric constant of insulating material, ε_{eff} effective dielectric value of insulating material, C_o light speed, fr resonance frequency, h thickness of insulating material and ΔL line expansion. The probe feed point is located at (x_0, y_0), and antenna input impedance is chosen as 50 Ω. Table 1 below demonstrates the output and input parameters of rectangular coax-fed antenna.

Table 1. Inset Fed Microstrip Antenna Parameters

Inputs	
Solution Frequency (fr)	10GHz
Substrate Thicknes (h)	2.4mm
Loss Tangent (tanδ)	0.005
Dielectric Constant (ε_r)	4.38
Conductor thickness (t)	0.035mm
Outputs	
Patch Width (W)	8.9mm
Patch Length (L)	5.4mm
Substrate Width	70mm
Substrate Length	70mm
SMA inner Radius (2a)	1.28mm
SMA outer Radius (2b)	4.1mm
Probe feed (xo)	3.75mm
Probe feed (yo)	2mm
Microstrip line impedanc (Z_0)	50Ω

3. Results and Findings

Simulation results of the designed antenna obtained by using HFSS simulation program are presented in this section. The return loss (RL) of the proposed antenna is shown in Figure 2. When simulation results are analyzed based on (<10 dB) RL criterion, it was observed that the maximum radiation of proposed antenna was primarily in 8.7GHz frequency and in 11GHz frequencies. At 8.7GHz operating frequency of the proposed antenna VSWR value was obtained as 0.5dB and RL value was obtained as -34.00dB. At 11GHz operating frequency of the proposed antenna VSWR value was obtained as 2dB and RL value was obtained as -18.59dB.

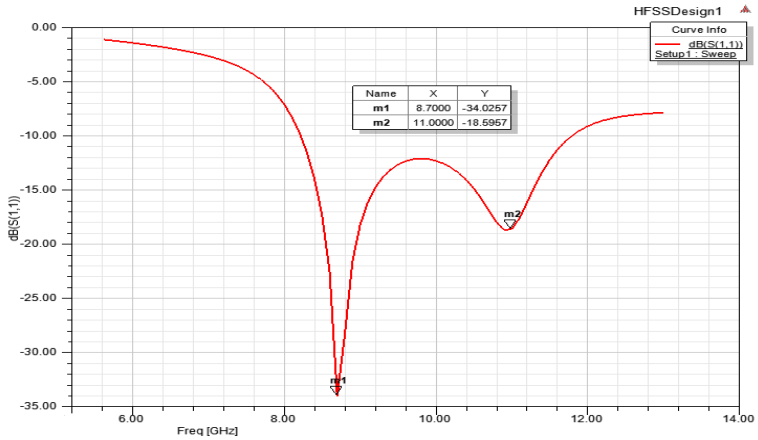

Figure 2. RL Characteristic of the Proposed Antenna

In Figure 3, VSWR characteristic of simulated antenna is given. Figure 4 shows all possible impedances in the frequency range (8 GHz–12 GHz) of the antenna on the Smith Chart, and from figure part of these impedances that fall into VSWR≤2 circle are seen.

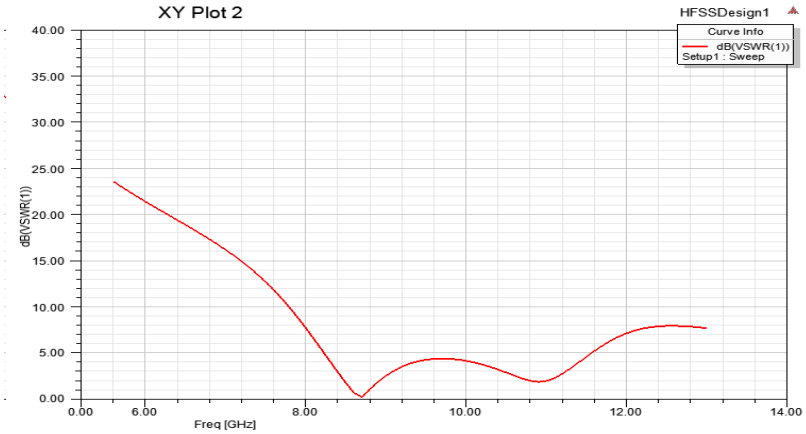

Figure 3. VSWR characteristic of proposed antenna.

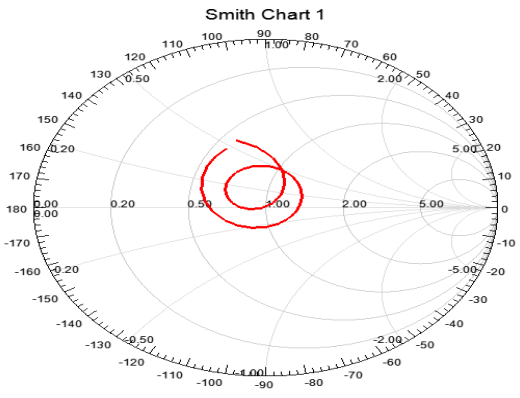

Figure 4. Changing of Input Impedance on Smith Chart.

It has been observed that the gain value is changed by shifting the feed point of the patch. The relationship between the feed shape and the gain at the corner points of the patch is shown in Figure 5.

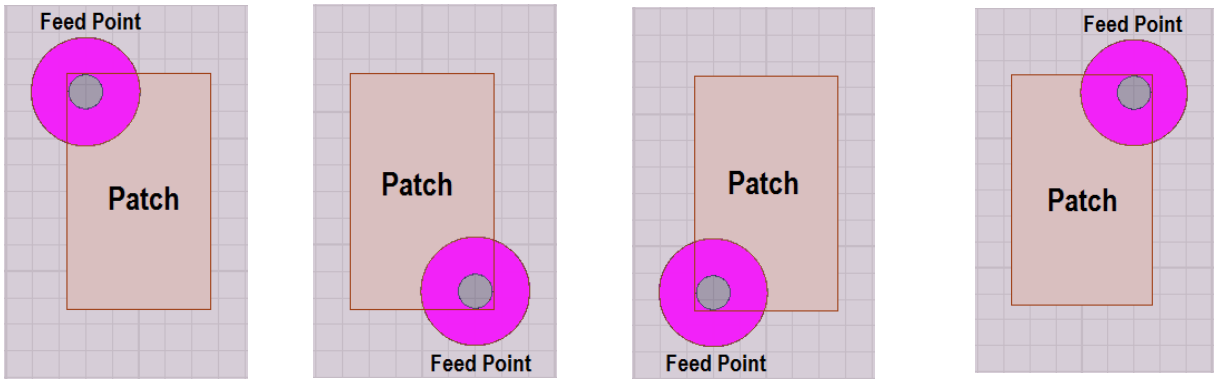

(a) **(b)** **(c)** **(d)**

Figure 5. Geometry structure of patch antenna at different feed points (a) (-3.75,-2) gain=9.46dB (b) (3.75,2) gain=11.65dB (c) (-3.75,2) gain=9.08dB (d) (3.75,-2) gain=8.82

In Figure 6, the E–Plane (phi=90º) 2D radiation pattern of proposed antenna with resonance frequencies 8.7GHz and 11GHz are shown.

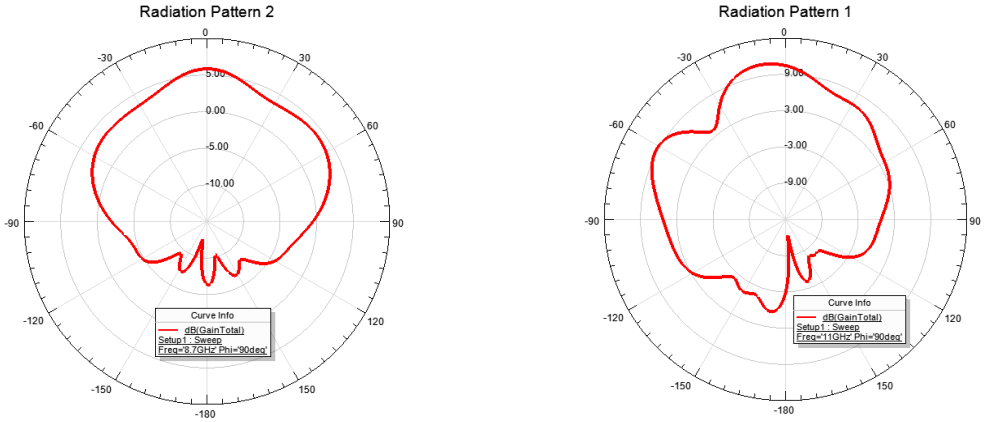

(a) **(b)**

Figure 6. Radiation Pattern E-Plane Graphs (a) 8.7GHz (b) 11GHz

4. Conclusion

In this study, a linearly polarized, high gain antenna that can operate in the X band is designed and simulated. The antenna shows the best radiation pattern when catches the appropriate high gain. In our study, 11.65dB gain was obtained at the frequency of 11GHz. The gain of the antenna at the feed point (xo=3.75, yo=2) and the return value behaved appropriately. The designed microstrip antenna is small size and high gain and suitable for today's communication devices. It is aimed to fabricate the designed antenna and add measurement results in the next stage.

Acknowledgment

This research was financially supported by the Researching Projects Committee of the University of Dicle (DUBAPK) with project number 14–MF–71. We are grateful to DUBAPK for financial assistance.

References

[1] D. Sanchez-Hernandez and I. D. Robertson. 1996. A Survey of Broadband Microstrip Patch Antennas. Microwave Journal, (Sep. 1996), 60-84.

[2] Dipak K. Neog, Shyam S. Pattnaik, Dhruba. C. Panda, Swapna Devi, Bonomali Khuntia, and Malaya Dutta, "Design of a Wideband Microstrip Antenna and the Use of Artificial Neural Networks in Parameter Calculation", IEEE Antennas and Propagation Magazine, Vol. 47, No.3, June 2005

[3] C.A. Balanis, *Antenna Theory Analysis and Design*, 3rd ed. Hoboken, NJ, USA: Wiley-Interscience, 2005, p. 816.

[4] S. Erdemir and A.E. Yılmaz, "L1 Frekansında Çalışan E-Şekilli Mikroşerit Gps Anteni Tasarımı", Uludağ Üniversitesi Mühendislik-Mimarlık Fakültesi Dergisi, Cilt 19, Sayı 1, 2014.

[5] James, J. R., Hall, P. S. 1988. "Handbook of Microstrip Antennas", The Institution of Engineering and Technology. 2.edition, (June 1, 1988) Number of Pages: 1350.

[6] Kumar, G. and Ray, "Broadband Microstrip Antennas", Artech House. 451p. , K.P. 2003, USA.

[7] Ansys Hfss (ver. 15), Ansys Corporation. Canonsburg, PA, USA. Retrieved from http://www.ansys.com/Products/Electronics/ANSYS-HFSS, 2014

[8] Garg, R., et al., Microstrip Antenna Design Handbook. Artech House Antennas and Propagation Library, 1-2, 2001

Vol 7, Number 1, 2017
European Journal of Technic
EJT

INVESTIGATION OF EFFECTS OF DIFFERENT PARAMETERS ON MECHANICAL PROPERTIES IN FRICTION STIR WELDING OF AZ31B MAGNESIUM ALLOY

Vedat Veli ÇAY[1,*], Nida KATI[2], Sermin Ozan[2], Veysel YAPICI[3]

[*1]Civil Aviation School, Dicle University, Diyarbakır

[2] Metallurgy and Materials Engineering Department, Firat University, Elazığ

[3]Gazi Vocational High School, Elazığ

[*]Corresponding athour; Email: vedatcay@yahoo.com

Received: 15 February 2017; Accepted: 12 May 2017

In recent year, the use of magnesium alloys in aerospace, space, and automotive industry as structural materials has gradually been increased. The solid state welding method for joining of these materials were effective. The friction stir welding is one of the solid state welding method. In this study, the weldability of rolled AZ31B magnesium sheets has been investigated by friction stir welding. Samples have been welded at different welding parameters such as the 1500, 2300 rpm rotational speeds and 100,160 and 190 mm/min transverse speeds. In order to investigate the effect of welding speeds and rotational speeds on metallurgical and mechanical properties, metallographic and mechanical tests were carried out on the welded areas of the samples.

Keywords: Welding, Friction stir welding, Magnesium alloys, Tensile strenght

1. Introduction

Magnesium is a widely used metal in industry due to its lightness and strength. In search of weight saving in automotive and space-aircraft industries, magnesium metal comes to the forefront as the lightest structural metal in terms of engineering applications with its low density of 1.74 g / cm^3 [1]

The fact that the magnesium is lighter than steel and zinc by 75% and aluminium by 33% makes it usable as a construction material in many industries. In addition, low inertia caused by the low density of magnesium is an advantage for fast moving parts. The lightness also means the easier transportation of the piece during manufacturing and cheaper shipment of the finished product. Thus, fuel consumption and emissions can be reduced. When magnesium alloys are compared with other metal alloys, it has a very high specific tensile compressive strength and a lower modulus of elasticity and thus a very high deflection resistance [2].

Along with major developments in metal and material science in recent years, the joining of metallic materials has gained a great importance [3]. Especially the problems arising from the production of new materials with improved properties and joining of these materials with existing fusion welding methods have led researchers to develop new joining methods. High heat input in joining magnesium and its alloys by using fusion-based welding methods can cause the formation of cracks in the welding seam as a result of high thermal expansion of these materials and the wide range of solidification temperatures [4]. In some alloys, the thermal cycle during welding causes the components in the main solid solution to precipitate in the molten zone or base material. This precipitation reduces mechanical properties and resistance to chemical impacts. Due to these reasons, it is difficult to weld magnesium plates by using fusion welding methods. Friction Stir Welding, one of the solid state welding methods, provides great advantages in joining these materials [5-7]. Friction Stir Welding, a newly developed solid state welding method, involves immersing a stepped stirrer tip rotating at high speed on an interface of two sheets fixed as butt-to-butt and moving it at a certain speed across the length desired to be welded [4,8].

In the literature, it is possible to encounter many studies on Al and its alloys by using the friction stir welding method. However, there is a limited number of studies on magnesium and its alloys. The aim of this study was to investigate the effect of different rpm and feed rate on mechanical behaviours by joining AZ31B magnesium sheets via friction stir welding method.

2. Material and Method

In the experimental study, AZ31B magnesium alloy was commercially supplied in the form of a plate with the dimensions of 400x1000x5 mm from VIG Machinery Industry Trade Limited Company (VIG Makine Sanayi Ticaret Limitet Şirketi) and it was sized for welding as shown in Figure 1. Table 1 shows the chemical composition of this alloy.

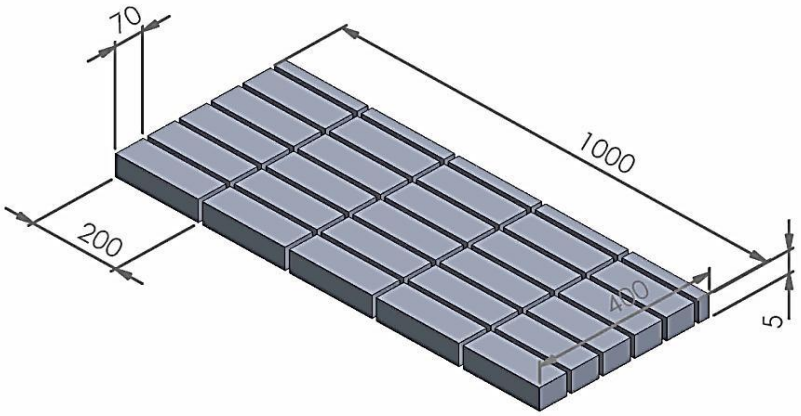

Figure 1. Sample dimensions of AZ31B Magnesium alloy supplied from the market and prepared for Friction Stir Welding

Table 1. Chemical composition of AZ31B magnesium alloy

AZ31B	Al	Zn	Mn	Si	Fe	Sn	Ag	Ti	Cu	Ni	Mg
%	3.0	1.01	0.2113	0.0137	0.0039	0.0015	0.0006	0.0005	0.0004	0.0002	95.72

Friction stir welding (FSW) process of the samples prepared for the welding process was performed by using BRIGGEPORT brand milling machine with max. 4600 rpm operating capability, adjustable rpm and adjustable feed rate in automatic position.

A tip in the form of screw tip geometry was used during the friction stir welding. Tips were designed in 2 parts so that their shoulder parts and tip parts were separate. While shoulder parts were made from AISI 1040 steel, tip parts were made from M5 guidance HSS steel.

As shown in Figure 2, the shoulder part was drilled thoroughly for screw tip, threaded into Ø 5 mm guide shoulder, and welded from the top.

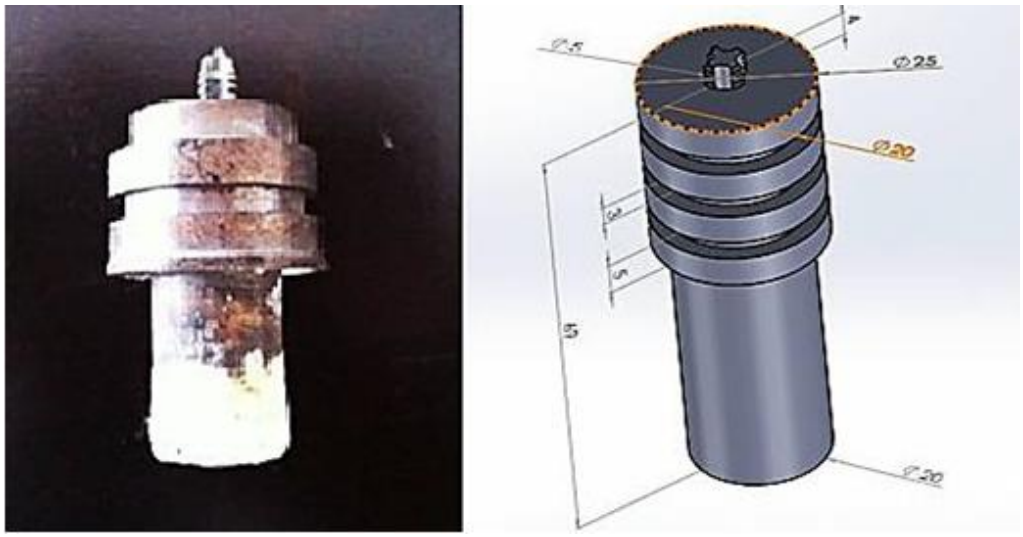

Figure 2. The schematic diagram of tool geometry.

After cleaning the welding surfaces of the materials to be welded, they were put as butt-to-butt. The sheets put as butt-to-butt were connected to the table and the weld line of the sheets was adjusted in parallel with the feed direction of the milling table and tightened with the fishplates (Fig. 3).

Friction stir welding was applied to magnesium alloy plates by using the welding parameters given in Table 2.

Figure 3. Fixture mechanism of the material couple to the milling machine

Table 2 Friction stir welding parameters

Sample No	Pin Geometry	Rotational speed (rpm)	Travel speed (mm/min.)
S1	Screw	1500	100
S2			160
S3			190
S4		2300	100
S5			160
S6			190

In the friction stir welding process, no deoxidization process was performed to the magnesium alloy prior to the welding process of the material, and the welding process was performed at the stages shown in Figure 4.

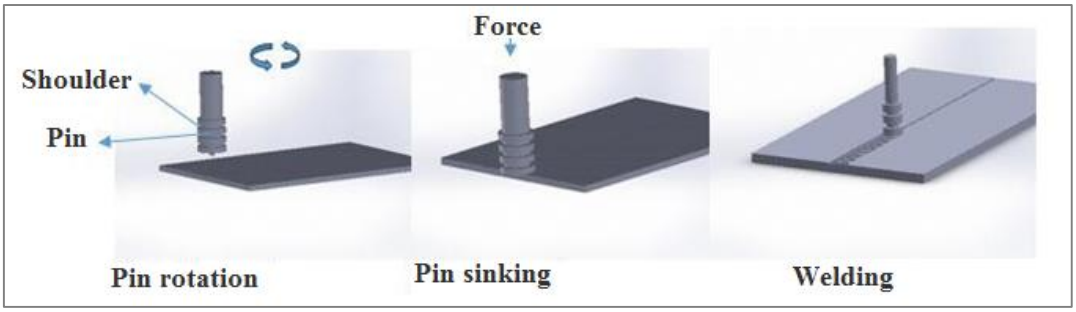

Figure 4. Stages of FSW

2.1. Microhardness Measurements

Microhardness measurements were performed to examine the hardness changes of the samples joined with friction stir welding. Before the microhardness measurements, the samples were

metallographically prepared and etched. The microhardness measurements of the etched samples were carried out by applying a load of 500 gr with the EMCOTEST DuraScan microhardness device with 1-mm intervals and a loading speed of 10 sec on a line perpendicular to the weld cross section from the central axis of the samples.

In the measurements, 136º square base pyramid tip was used. Figure 5 shows the regions where the microhardness measurements were made.

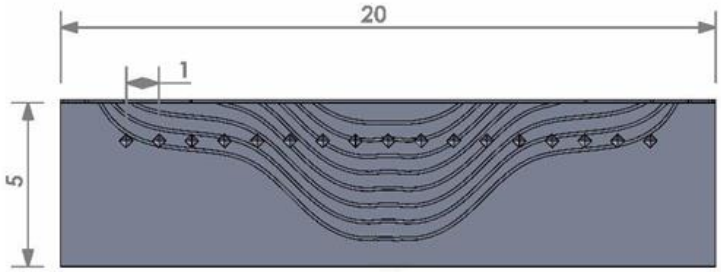

Figure 5. Hardness measurement scheme

2.2. Tensile Tests

Welded samples were prepared by cutting in CNC milling machine in order to apply tensile test to the friction stir welded samples. They were machined as in Figure 6 and brought into the appropriate sizes according to TS 287 (EN 895).

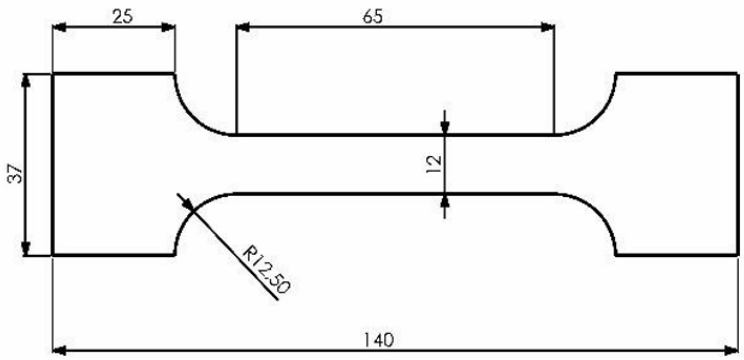

Figure 6. Schematic sketch of tensile specimen.

3. Result and Discussion

When friction stir welded samples were examined, it was observed that the microstructure zone of the welded sample was composed of four different zones. These zones were analysed as Base Metal (BM), Heat Affected Zone (HAZ), Thermo-mechanically Affected Zone (TMAZ) and Dynamically Recrystallized Zone (DRZ) as in figure. The DRZ is also divided into two namely, Crown and Nugget. (Fig. 7)

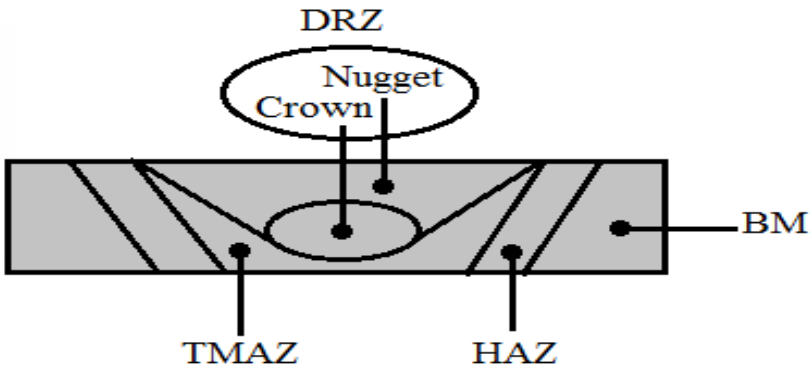

Figure 7. Schematic view of the microstructure formed in the weld region.

3.1. Microhardness

Before performing welding process to AZ31B Mg alloy, 10 different points were measured and the average hardness value was calculated as 65 HV.

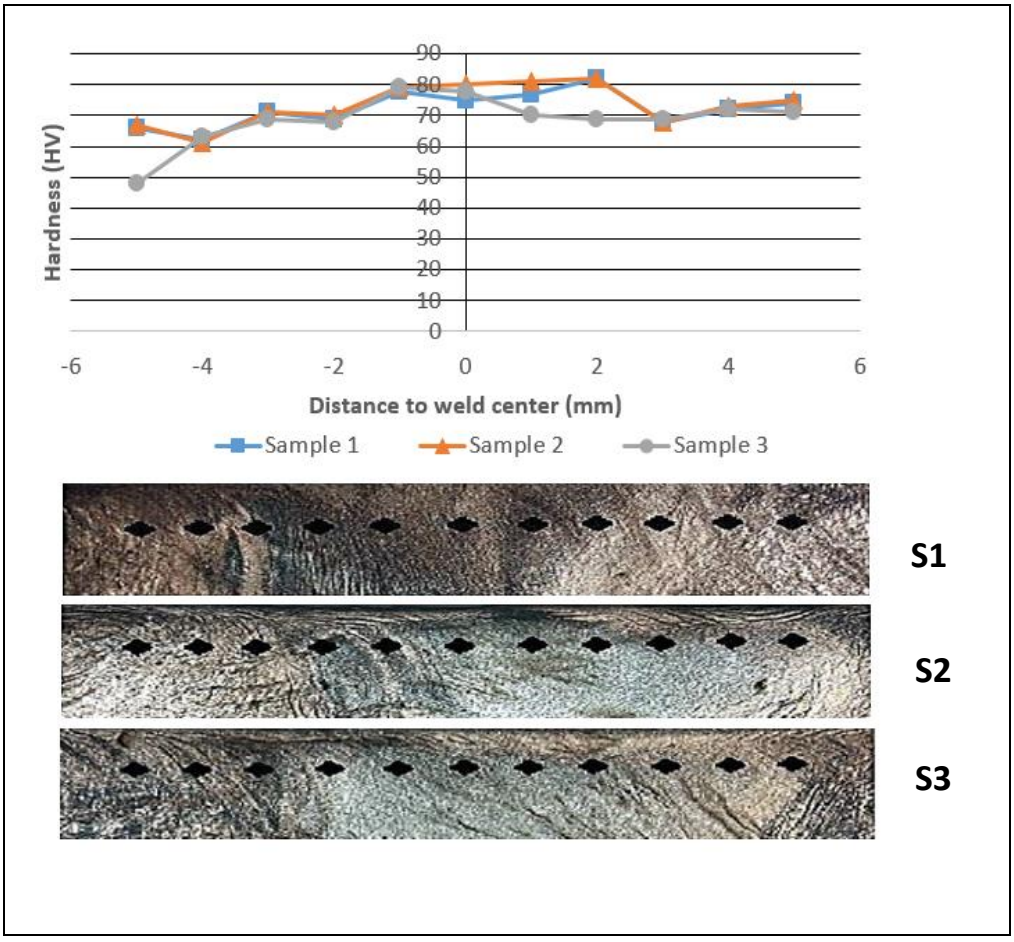

Figure 8. Hardness profiles registered across the transverse cross-section of the welded samples (S1,S2,S3).

Figure 8 shows microhardness graph of samples S1, S2 and S3 joined using 1500 rpm and feed rates of 100/160/190 mm/min. It was measured that maximum hardness value of sample S1 was 78 vickers, maximum hardness value of sample S2 was 82.6 vickers and maximum hardness value of sample S3 was 77.1 vickers. This measured maximum hardness values were found in the DRZ. The hardness value of all the samples in the DRZ was higher than the hardness of the base material. The reason for this was the formation of recrystallization by the effect of plastic deformation and heat and the thinning of grain structure [9]. As we got closer to the base material from the welding interface, hardness values decreased and the results close to the hardness values of the base material were obtained.

When the hardness distribution was examined, hardness decreased in a zone starting from the weld zone and close to the surrounding of the tool shoulder. The hardness values increased when it moves away from the centre in the tool shoulder length. This was associated with the reduction of heat effect in these zones.

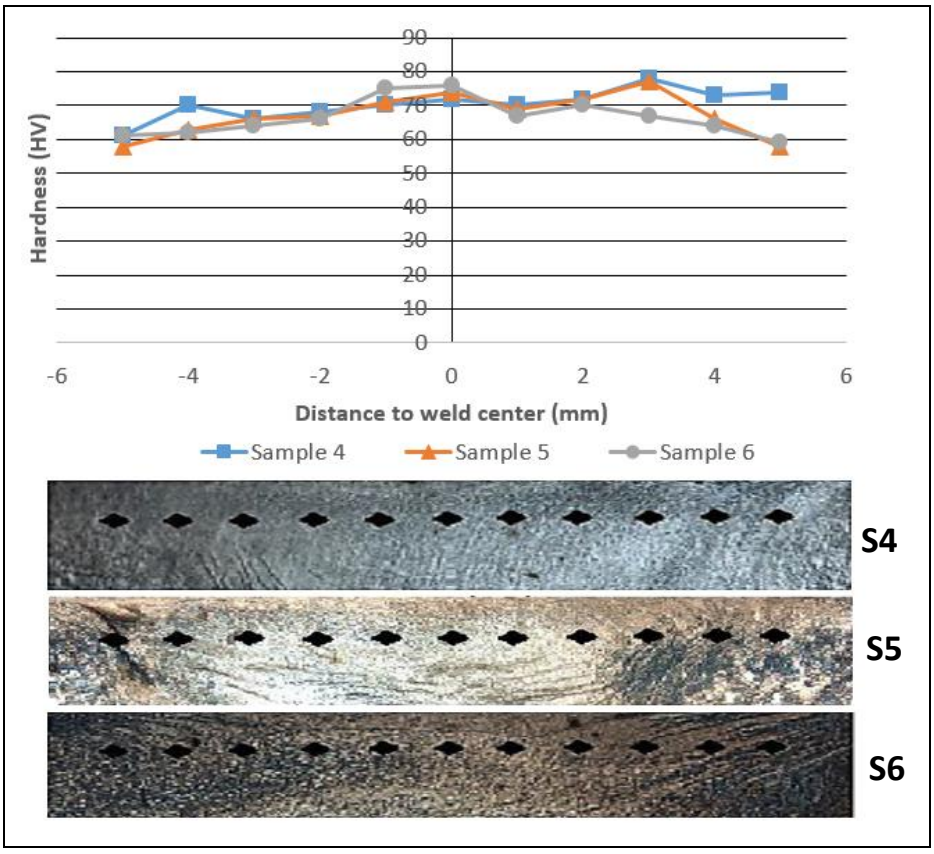

Figure 9. Hardness profiles registered across the transverse cross-section of the welded samples (S4,S5,S6).

Fig. 9 shows microhardness graph of samples S4, S5 and S6 joined using 2300 rpm and feed rates of 100/160/190 mm/min. It was measured that maximum hardness value of sample S4

was 78 vickers, maximum hardness value of sample S5 was 76,5 vickers and maximum hardness value of sample S6 was 74,6 vickers. When the hardness distributions of these welded connections are examined, it is seen that there is a similar distribution in all three samples.

When microhardness values of specimens at 1500 rpm and 2300 rpm were evaluated, no significant differences were found. However, depending on the increasing rotational speed, the hardness values of S4, S5 and S6 were slightly lower. However, depending on the increasing speed of rotation, the hardness values of S4, S5 and S6 were slightly lower. This is due to the excess heat input to the sample, depending on the speed of rotation.

3.2. Tensile Properties

Figure 10 shows tensile-strain graphs of all samples. When the graph of the S1 sample joined with 1500 rpm, screw tip and 100 mm/min feed rate was examined, it was observed that tensile stress was 79 Mpa, the breaking stress was 77 Mpa and % elongation value was 1.5. It was observed that the tensile stresses of samples S2/S3 were 80/109 Mpa, the breaking stresses were 80/109 Mpa and % elongation values were 1.8/2.1 in the welding process in the same rpm with 160 mm/min and 190 mm/min feed rates respectively.

When fracture surface images of the samples were examined, the part under the shoulder of the mixer (crown region) showed work hardening due to the effect of stirring and the strength increased and the samples fractured from a point between the heat-affected zone (HAZ) and the thermodynamically recrystallized zone (TMAZ) [10]. No significant change in tensile values was observed with increasing welding speed.

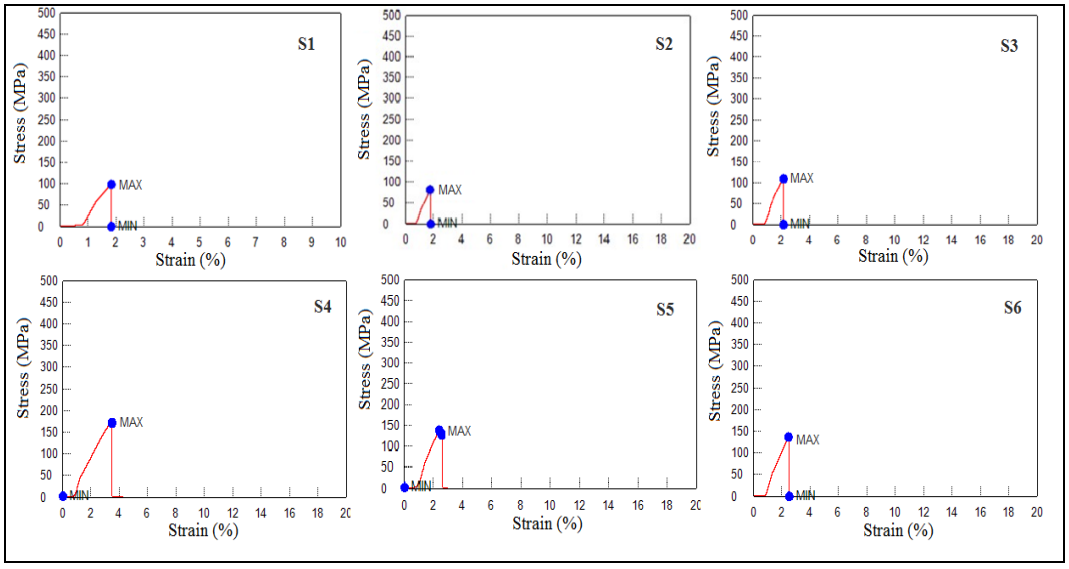

Figure 10. Example stress–strain curves of all samples

It was seen from Figure 10 that tensile stress was 173 Mpa, breaking stress was 171 Mpa and % elongation value was 3.5 in the stress/strain graphs of sample S4 joined with 2300 rpm, threaded tip and 100 mm/min feed rate. When the graphs of samples S5/S6 at different feed rates were examined, it was determined that the tensile stresses were 138/136 Mpa, breaking stresses were 127/136 Mpa and % elongation values were 2.6/2.5, respectively. Table 3 shows the welding parameters of all samples and the strength values obtained from tensile test.

The tensile strength values of the samples in this group decreased with increasing feed rate. This is because the amount of heat entering the material reduced, so the grain coarsening also occurred less. When the fracture surface images of samples S4, S5, and S6 were examined, it was determined that the fracture sites were in the region between the thermodynamically affected zone (TMAZ) and the heat-affected zone (HAZ) as in the other sample groups.

Tablo 3. FSW parameters and results of tensile test

Sample No	Pin Geometry	Rotational speed (rpm)	Travel speed (mm/min.)	Ultimate tensile strenght (Mpa)	Yield strenght (Mpa)	Elongation (%)
S0				274	271	10
S1	Screw	1500	100	79	77	1,5
S2			160	80	80	1,8
S3			190	109	109	2,1
S4		2300	100	173	171	3,5
S5			160	138	127	2,6
S6			190	136	136	2,5

Even though the related studies have revealed that the most important parameters affecting the welding quality are feed rate and rotational speed of the tip, the rotational speed of the tip rather than the feed rate was found to be effective in the present study. A quite brittle structure formed in the weld zone in welding of Mg alloys [11]. This is because the Mg alloy has a hexagonal closest- packed (HSP) lattice system and a cross- shifting is observed in these materials. When the stress-strain curves were examined, it was observed that tensile sample stretched in a very low rate and the material fractured even before passing to the plastic zone [12] This is because the weld zone had a very fragile structure and also there were porosities in the weld zone.

4. Conclusions

In this study, 5 mm-thick AZ31B magnesium alloy sheets were successfully joined by using friction stir welding method with different rpm values and feed rates and the following generalizations can be made depending on the results obtained with the effects of these parameters on the mechanical properties.

1. It was observed that welding seam image of the samples joined with friction stir welding was much smoother than the other welding methods and no machining process was necessary.
2. Weld defect (gap) occurred in all samples of AZ31B magnesium alloy in FSW. Such gap defects have also been determined in other studies in the literature. This situation is one of the characteristic faults occurring at the welding of magnesium alloys.
3. It was observed in all welded samples that the orientations in weld metal with the increasing welding feed rate increased but the orientations in the weld metal at low feed rates were not evident.
4. When the microhardness values of samples S1 (100 mm/min), S2 (160 mm/min) and S3 (190 mm/min) welded at 1500 rpm and screw tips were examined, hardness values close to each other were obtained in each of three samples. Accordingly, it was thought that the feed rate did not have any significant effect on the hardness of the welded joint.
5. Hardness values close to each other were also obtained in the samples S4 (100 mm/min), S5 (160 mm/min) and S6 (190 mm/min) welded with 2300 rpm and threaded tip.
6. When the tensile strength results of all the samples were examined, it was observed that these values were lower than the tensile strength value of the base material. When the tensile test results were examined, it was observed that the fractures occurred usually in the zones between the thermo-mechanically affected zone (TMAZ) and the heat-affected zone (HAZ). The reason for occurrence of the fractures in these zones was the formation of grain coursing due the heat effect and thus the decrease of the strength in this transition zone.

References

[1] Zeytin, H.K., Magnezyum Alaşımları: Otomotiv Endüstrisinde Uygulaması ve Geleceği, *Marmara Araştırma Merkezi,* Kocaeli 1999

[2] Mert, F., Özdemir, A., Karatas, Ç., Magnezyum Alaşımlarının Basınçlı Döküm Yöntemiyle Kalıplanabilirliğinin Değerlendirilmesi, *Journal of Polytechnic* 13 (2010) 3 pp 165-176

[3] Thomas, W.M., Nicholas, E.D., Friction Stir Welding for the Transportation Industries,

Material Desing, 18 (1997) 269-273.

[4] Özdemir, N., Büyükarslan, S., Sarsılmaz**,** F., Sürtünme Karıştırma Kaynak Yöntemi ile Birleştirilmiş AA1030 Alüminyum Alaşımında Karıştırıcı Uç Profili ve İlerleme Hızının Arayüzey Mikroyapı Değişimi Üzerine Etkisi, *Fırat Ünv. Fen ve Müh. Bil. Dergisi*, 19 (2007) 3 407-415.

[5] Johnsen M.R., Friction Stir Welding Takes Off at Boeing, Welding Journal, Cambride UK, (199) 35-39.

[6] Çam, G., Sürtünme Karıştırma Kaynağı ve Uygulamaları, PAÜ Müh. Fak. *9. Denizli Malzeme Sempozyumu* (2002) 450-458.

[7] Metal Handbook, Nonferrous Alloys an Special Purpose Materials, Volume: 2 ASM 1993.

[8] Şık, A., Sürtünme Karıştırma Kaynağı ile Birleştirilen Magnezyum Levhaların Mekanik Özelliklerinin İncelenmesi, SAÜ. Fen Bil. Der. 14 (2010) 2 s 134-140.

[9] Fujii, H., Cui, L., Maeda, M., Nogi K., Effect Of Tool Shape On Mechanical Properties and Microstructure of Friction Stir Welded Aluminum Alloys, *Materials Science and Engineering*: A, (2006) 419, 25-31.

[10] Cavaliere P., Cerri, E., Mechanical Response of 2024-7075 Aluminium Alloys Joined By Friction Stir Welding, **Journal of Materials Science**, 40 (2005) 3669 – 3676.

[11] Ericsson M., Jin, L.Z., Sandström R., Fatigue properties of friction stir overlap welds, *International Journal of Fatigue***,** 29 (2007) 57-68.

[12] Cavaliere, P., Squillace, A., High temperature deformation of friction stir processed 7075 aluminium alloy, *Materials Characterization*, 55 (2005) 136-142.

EFFECTS OF NEAR-FAULT AND FAR-FAULT GROUND MOTIONS ON SEISMIC PERFORMANCE OF 5-STORY R/C BUILDING

Rehber AKDOĞAN*, A.Halim KARAŞİN

Dicle Üniversitesi, İnşaat Mühendisliği Bölümü, Diyarbakır, Turkey

* Corresponding author; E-mail: rehber.akdogan@dicle.edu.tr

Received: 15 October 2016; Accepted: 12 April 2017

In this study, seismic performance of a building structure which designed according to current Turkey Earthquake Code (TEC-2007) is examined. Effects of near-fault and far-fault ground motions on the seismic performance is investigated. Current earthquake code is not describe any information about near-fault or far-fault ground motion. To search this effect, 3 groups of strong ground motions each include 7 strong ground motion records are selected with regard to TEC-2007 and seismic performance of 5-story reinforced concrete structure is assessed. The focused structure is represent our county stock in high incidence. The results show that near-fault records are more destructive for structure.

Key words*: seismic performance, near-fault, far-fault, strong ground motion*

YAKIN VE UZAK FAY YER HAREKETLERİNİN 5 KATLI BETONARME BİNANIN DEPREM PERFORMANSINA ETKİSİ

ÖZET: Yapılan çalışmada, konut tipi bir yapının ülkemizde kullanılmakta olan deprem yönetmeliğine (DBYBHY-2007) göre deprem performansı incelenmiştir. Güncel çalışmalarda sıkça ele alınan yakın fay ve uzak fay etkilerinin deprem performansı incelemesindeki etkisi irdelenmiştir. Mevcut deprem yönetmeliği yakın veya uzak fay etkisi ile ilgili bir tanımlama yapmamaktadır. Bu etkiyi inceleyebilmek için faya mesafesine göre her biri 7 kuvvetli yer hareketinden oluşan 3 grup kuvvetli yer hareketi kaydı yönetmeliğimize göre seçilmiş ve bu kayıtlara göre yapının performansı incelenmiştir. İncelenen betonarme yapı, ülkemizde konut amaçlı kullanılan yapı stokunun ciddi bir kısmını oluşturduğu için 5 katlı olarak belirlenmiştir. Uygulanan analizlerden elde edilen sonuçlara göre faya yakın kaydedilen yer hareketlenin yapıda daha fazla hasara yol açtığı anlaşılmıştır.

Anahtar sözcükler: deprem performansı, yakın fay, uzak fay, kuvvetli yer hareketi.

1. Giriş

Ülkemizdeki nüfusun %70'i 1. ve 2. derece deprem bölgelerinde yaşamakta olduğundan dolayı uzun yıllar boyunca yaşanan depremlerde (Erzincan 1992, Kocaeli 1999, Van 2011 vs) büyük can kayıpları yaşanmış, meydana gelen hasarlardan dolayı tüm ülkede büyük manevi ve maddi kayıp yaşanmıştır. Böylesi kayıplara neden olan imalat ve tasarım kusurları 1940lardan bu yana çıkartılan deprem şartnameleriyle giderilmeye çalışılmıştır. Geçmişin verdiği her deneyimle beraber gelişen deprem bilgisi yenilenen her şartnameyle beraber ortaya koyulmuştur. Geliştirilen yeni hesap yöntemleri ve mühendislik yaklaşımlarıyla günümüze kadar geliştirilerek sunulan depremle ilgili teknik şartnameler [1];

- •1940 – Zelzele Mıntıkalarında Yapılacak İnşaata Ait İtalyan Yapı Talimatnamesi
- •1944 – Zelzele Mıntıkaları Muvakkat Yapı Talimatnamesi
- •1949 – Türkiye Yersarsıntısı Bölgeleri Yapı Yönetmeliği
- •1953 – Yersarsıntısı Bölgelerinde Yapılacak Yapılar Hakkında Yönetmelik
- •1962 – Afet Bölgelerinde Yapılacak Yapılar Hakkında Yönetmelik
- •1968 – Afet Bölgelerinde Yapılacak Yapılar Hakkında Yönetmelik
- •1975 – Afet Bölgelerinde Yapılacak Yapılar Hakkında Yönetmelik
- •1998 – Afet Bölgelerinde Yapılacak Yapılar Hakkında Yönetmelik
- •2007 – Deprem Bölgelerinde Yapılacak Binalar Hakkında Yönetmelik

DBYBHY-2007 [2] yönetmeliği ülkemizde geçerli olan en güncel deprem yönetmeliğidir. Bu yönetmelik hem deprem analizi hem de taşıyıcı sistem tasarımı açısından diğer yönetmeliklere kıyasla daha gelişmiş olmakla beraber doğrusal olmayan zaman tanım alanında kullanılmak üzere seçilecek deprem kayıtlarında, depremin merkez üssünün deprem kaydının alındığı noktaya uzaklığını dikkate almamaktadır. Ancak, özellikle son yıllarda faya yakın bölgelerden elde edilen deprem kayıtlarının yüksek hızlı darbe etkisi içermesi nedeniyle diğer kayıtlara göre önemli farklılıklar içerdiği

bilinmektedir. Akkar ve ark. [3], yakın fay ve uzak fay kuvvetli yer hareketi arasındaki farkı Şekil 1'de gösterilen hız kaydında da görülen darbe periyodu ile açıklamışlardır. Buradaki darbe periyodu, fayın kayıt merkezine uzaklığı, fayın doğrultusu ve fayın yırtılma yönünden etkilenmektedir [4, 5, 6].

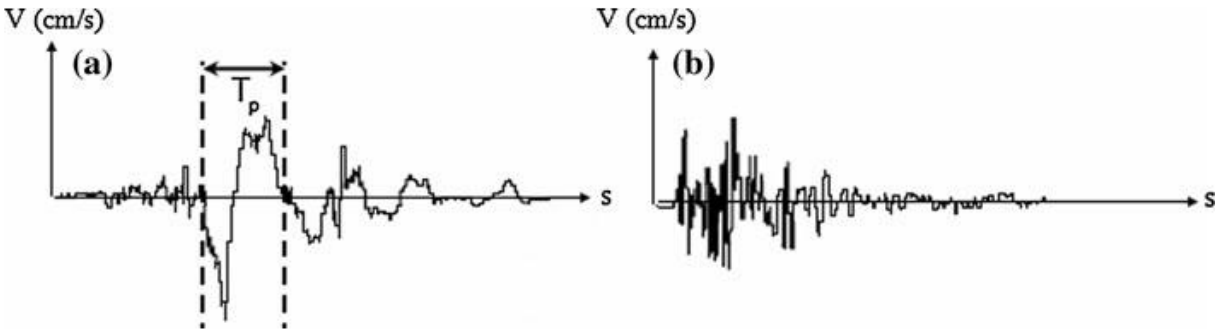

Şekil 1. Kuvvetli Yer Hareketi Hız Kaydı, (a)Yakın Fay Kuvvetli Yer Hareketi, (b)Uzak Fay Kuvvetli Yer Hareketi [3]

Yakın fay etkileri konutlar, barajlar, tüneller, nükleer santraller gibi pek çok yapı tipinde incelenmiştir. Chopra ve Chintanapakdee [7] yaptıkları çalışmada tek serbestlik dereceli sistemlerde yakın fay ve uzak fay deprem kayıtlarının spektruma etkisini incelemişlerdir. Yakın fay deprem kayıtlarının bileşenlerinin bile çoğu durumda farklı etkilere sebep olduğunu belirtmişlerdir. Adanur ve ark. [8] ise uzak ve yakın fay deprem kayıtlarının Boğaziçi köprülerinin deprem performanslarına etkilerini incelemişlerdir. Zhang ve Wang [9] uzak ve yakın fay deprem kayıtların betonarme ağırlık tipi bir barajın sismik performansına etkisini incelemişlerdir. Liu ve ark. [10] faya yakın bir bölgede olduğu düşünülen farklı kat sayısına sahip bitişik binaların etkilerini incelemişlerdir. Mazza ve Vulcano [11] yaptıkları çalışmada yakın fay yer hareketlerinin yatay ve düşey bileşenlerini dikkate alarak taban izolasyonlu betonarme çerçeveli binaların doğrusal olmayan dinamik tepkileri üzerine etkilerini incelemişlerdir.

2. Yöntem

Bu çalışma kapsamında deprem merkez üssünün, deprem kaydının alındığı noktaya uzaklığı irdelenmiştir. Bu amaçla, öncelikle betonarme bir yapının tasarımı yapılmış ve tasarım kriterlerine uygun olarak deprem grupları belirlenmiştir.

2.1. Tasarım

Dikkate alınan bina 5 katlı, her iki yönde 3 açıklıklı, betonarme çerçeveli taşıyıcı sisteme sahip, konut amaçlı kullanılacak simetrik bir binadır. Yapının her iki yönde 5'er m açıklığa sahip olduğu düşülmüştür. Bu yapının statik hesabı, ülkemizde sıklıkla kullanılmakta olan Sta4Cad paket programı [12] kullanılarak yapılmıştır. Program tasarımda TSE-500 [13], TSE-498 [14] VE DBYBHY-2007 [2] yönetmeliklerini dikkate almaktadır. Tasarım aşamasında dikkate alınan bilgiler Tablo 1'de verilmiştir;

Tablo 1. Tasarım Parametreleri

Tasarım parametresi	Veri
Deprem bölge katsayısı (A_0)	0.4
Deprem yapı davranış katsayısı (R_x/R_y)	8
Yapı önem katsayısı (I)	1
Yerel zemin sınıfı	Z2
Zemin grubu	C
Spektrum karakteristik periyodu (T_a/T_b)	0.15/0.6
Hareketli yük katsayısı	0.3
Zemin yatak katsayısı (Ko)	3000 t/m^3
Kayma dalgası hızı, ($V_{s,30}$)	200~400 m/s
Sabit yük (G)	5.0 kN/m^2
Hareketli yük (Q)	3.5 kN/m^2

Şekil 2'de yapının genel görünümü (sol) ve dikkate alınan aks ve eleman bilgileri (sağ) verilmiştir.

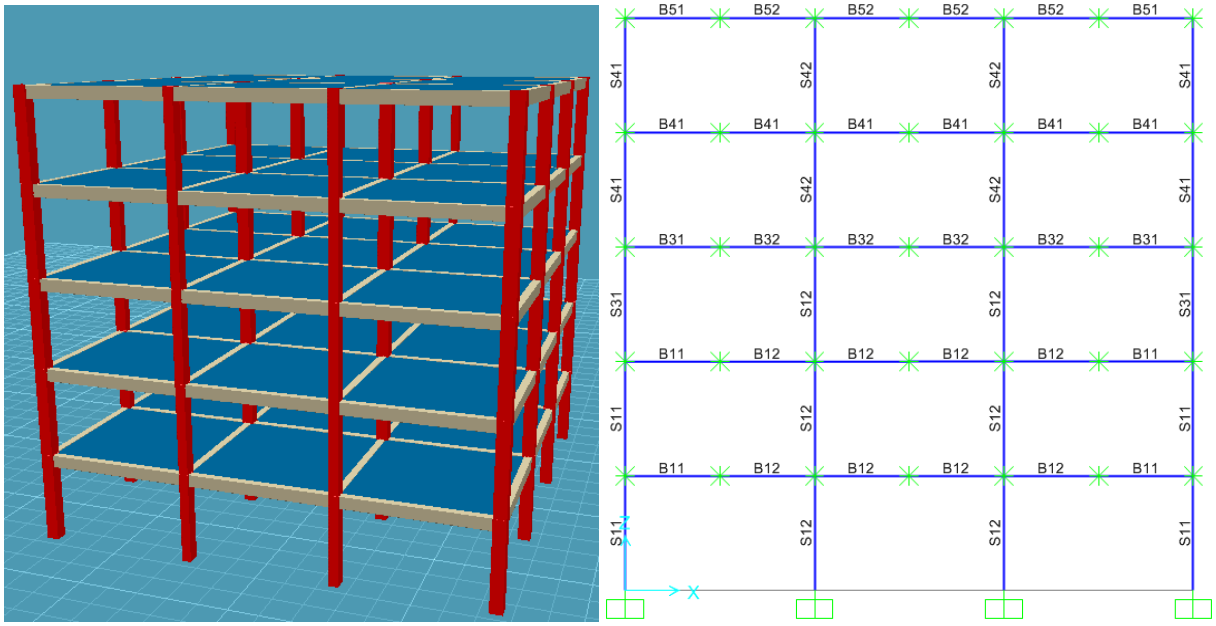

Şekil 2.Yapnın Genel Görünümü (Solda), Dikkate Alınan Aks ve Eleman Bilgileri (Sağda)

Çerçeve sistemindeki elemanların tümü çubuk olup, kirişlerin tamamı 25x40, S11 kolonları 35x40 ve S12 kolonları 40x40 boyutlarındadır (Şekil 3). Tasarım aşamasında kiriş tabliyesinin kesit dayanımına olan etkisi dikkate alınmamıştır.

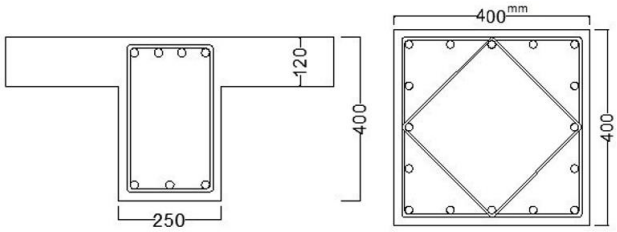

Şekil 3. Kiriş ve Kolon Eleman Kesitleri

Çerçeve sistemin yükleri, döşemelerin yükleri uygun şekilde dağıtılarak hesaplanmıştır. Bina ve kat kütlesi buna göre hesaplanmıştır,

$$mi=G+0.3*Q=570.75\ kN \quad (1)$$

2.2. Kuvvetli Yer Hareketlerinin Belirlenmesi

Statik ve betonarme tasarımı yapılan çerçeve sistemi Perform-3D sonlu elemanlar programı [15] kullanılarak modellenmiş ve sismik analizleri yapılmıştır. Serbest titreşim analizi sonucunda yapının hâkim titreşim periyodu T1=1.328 sn, katkı çarpanı %82 olarak hesaplanmıştır. Kuvvetli yer hareketi kayıtlarının seçimi DBYBHY-2007 dikkate alınarak belirlenmiştir. Buna göre;

• Kuvvetli yer hareketi kısmının süresi, binanın birinci doğal titreşim periyodunun 5 katından ve 15 saniyeden kısa olmamalı,

• Üretilen deprem yer hareketinin sıfır periyoda karşı gelen spektral ivme değerlerinin ortalaması A0g'den küçük olmamalı,

• Her ivme kaydı için %5 sönüm oranı için yeniden bulunacak spektral ivme değerlerinin ortalaması, 0.2T1 ile 2T1 arasındaki periyodlar için tanımlanan Sae(T) elastik spektral ivmelerinin %90'ından daha az olmamalıdır.

PEER Ground Motion Database'den [16] faydalanılarak seçilen deprem kayıtları DBYBHY-2007 dikkate alınarak yeniden ölçeklendirilmiştir. Belirlenen gruplarda fayın uzaklıkları Joyner-Boore mesafelerine göre (Rjb) sınıflandırılarak Tablo 2'de verilmiştir.

Tablo 2. Deprem Kayıt Grupları

Grup	Faya olan uzaklık (R_{jb}), km
G1	0-5
G2	5-20
G3	20-100

PEER Ground Motion Database, Amerikan şartnamelerini (ASCE 7-16, 2016 [17]) dikkate alarak deprem kayıtlarını belirlemektedir. Bu şartnamede deprem kayıtlarının belirlenmesi, 2 boyutlu veya 3 boyutlu yapı tipine göre farklıdır. Bu nedenle, belirlenen deprem kayıtları DBYBHY-2007'de uygun olarak kontrol edilmesi gerekmektedir. Tablo 2'de verilen uzaklıklar ve Tablo 1'de verilen tasarım parametrelerine uygun olarak belirlenip yeniden ölçeklendirilen deprem kayıtları Tablo 3'te verilmiştir.

Tablo 3. Dikkate Alınan Deprem Kayıtları

Grup	NGA	Deprem kaydı	Büyüklüğü (mag)	R_{jb} (km)	Ölç. kats.
	179 FN	Imperial Valley-06	6.53	4.9	1.60
	183 FP	Imperial Valley-06	6.53	3.9	1.00
	821 FN	Erzincan, Turkey	6.69	0	1.10
G1	1063 FN	Northridge-01	6.69	0	0.75
	1085 FN	Northridge-01	6.69	0	0.80
	1176 FP	Kocaeli, Turkey	7.51	1.4	1.00
	1605 FP	Duzce, Turkey	7.14	0	1.22
	184 FP	Imperial Valley-06	6.53	5.1	1.00
	266 FN	Victoria, Mexico	5.33	18.5	4.00
	802 FN	Loma Prieta	6.9	7.6	2.00
G2	988 FP	Northridge-01	6.69	15.5	3.00
	1009 FN	Northridge-01	6.69	14.6	2.00
	1158 FP	Kocaeli, Turkey	7.51	13.6	1.50
	1500 FN	Chi-Chi, Taiwan	7.62	17.2	2.00
	169 FP	Imperial Valley-06	6.53	22.0	2.00
	832 FN	Landers	7.28	69.2	3.00
	838 FP	Landers	7.28	34.9	4.00
G3	862 FN	Landers	7.28	54.2	4.00
	1187 FN	Chi-Chi, Taiwan	7.62	38.1	2.21
	1640 FN	Manjil, Iran	7.37	93.6	4.00
	3277 FN	Chi-Chi, Taiwan	6.3	61.5	4.00

3. Bulgular

Her deprem grubu için ayrı ayrı yapılan analizlerden elde edilen kesme kuvveti, yer değiştirme oranı ve eleman uç dönmelerinin ortalaması alınarak (DBYBHY-2007, 2.9.3) elde edilen değerlerle deprem performansı elde edilmiştir. Burada tanımlanmış olan hasar bölgeleri ve hasar sınırları Şekil 4'te gösterilmiştir.

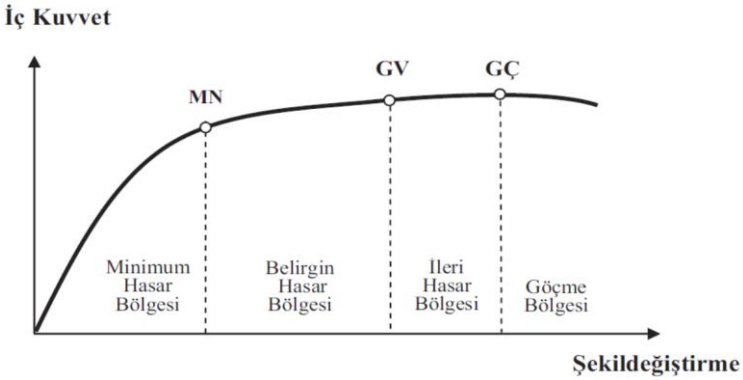

Şekil 4.Eleman Düzeyinde Hasar Sınırlandırması (DBYBHY-2007)

Elde edilen sonuçlara göre tüm analiz grupları için hem kat kesme kuvveti hem de eleman kesme kuvveti açısından güvenli olduğu tespit edilmiştir. Rölatif kat yer değiştirmesi ve eleman

düzeyinde performans sonuçları analiz grubuna bağlı olarak Tablo-4'de verilmiştir. Burada MN minimum hasar bölgesini, BH belirgin hasar bölgesini, İH ileri hasar bölgesini ve G göçme gölgesini göstermektedir.

Tablo 4. Performans Değerlendirmesi Sonuçları

Grup	Eleman	Eleman hasarları				Yapı hasarı	
		MH	BH	İH	G	Depl., %	Hasar
G1	Kolon	16	4	-	-	2.797	BH
	Kiriş	6	6	3	-		
G2	Kolon	16	4	-	-	2.300	BH
	Kiriş	6	9	-	-		
G3	Kolon	16	4	-	-	2.352	BH
	Kiriş	6	9	3	-		

Eleman uç eğriliğine bağlı sismik performans sonuçları Şekil 5'te gösterilmiştir. Şekillerde eleman uç hasar düzeyleri renklerle ifade edilmiştir. Beyaz minimum hasar düzeyini, mavi belirgin hasar düzeyini ve kırmızı ileri hasar düzeyini göstermektedir.

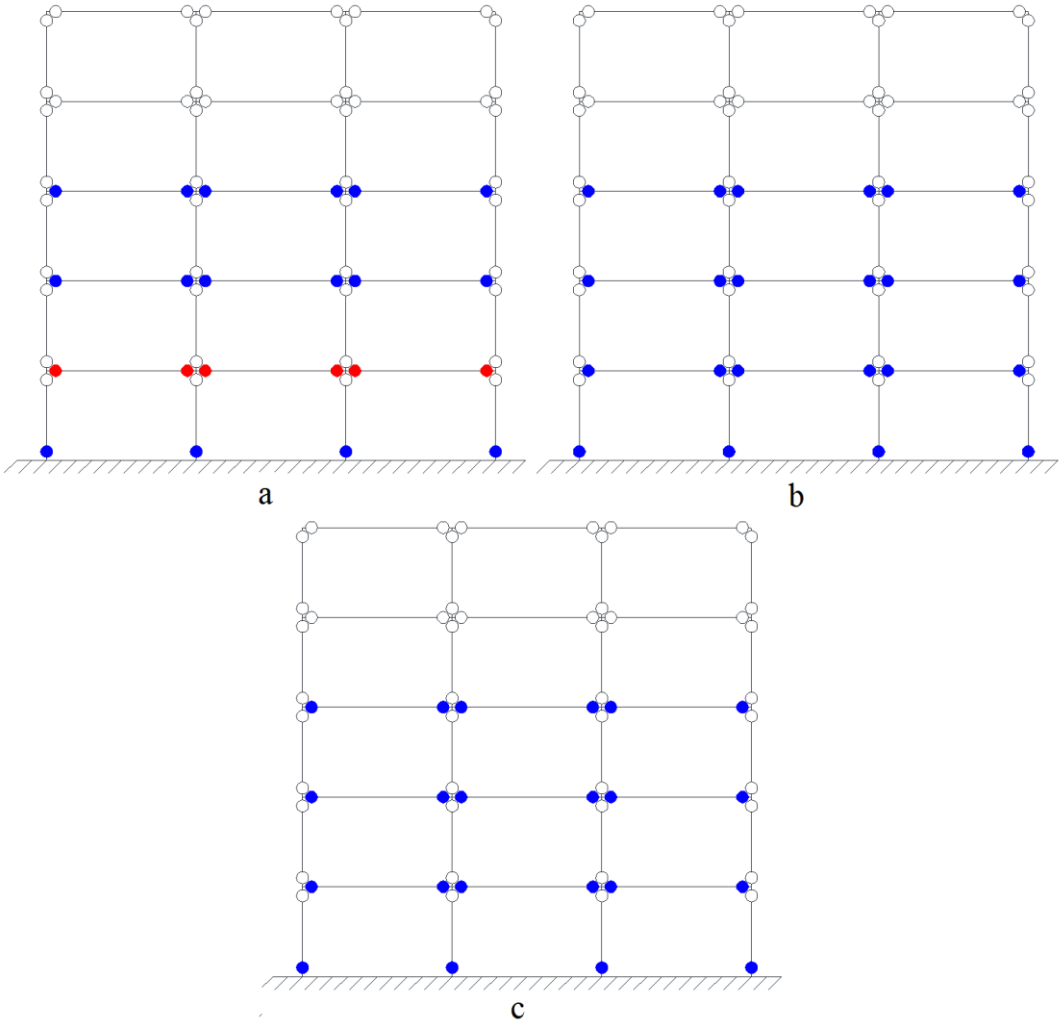

Şekil 5.Eleman Hasar Düzeyleri, a) G1 Grubu, b) G2 Grubu, c) G3 Grubu

4. Sonuçlar

Bu çalışmada, DBYBHY-2007'e göre tasarlanmış betonarme bir yapının orta aksının, faya uzaklıklarına göre farklı belirlenmiş 3 kuvvetli yer hareketi grubuna göre deprem performansı incelenmiştir. Dikkate alınan çerçeve için yapılan analizler neticesinde aşağıda sıralanan sonuçlar elde edilmiştir;

• Tüm kat ve elemanların kesme kuvveti açısından yeterlidir.

• Kat yer değiştirme oranının en yüksek %2.797 ile G1 grubunda ve en düşük %2.3 ile G2 grubunda olduğu ancak bütün analiz gruplarında bu açıdan belirgin hasar seviyesinde olduğu tespit edilmiştir.

• Eleman eğrilikleri açısından en fazla hasarın G1 grubunda oluştuğu ve bazı kirişlerin ileri hasar bölgesine ulaştığı görülmüştür.

• En az hasarın ise G2 ve G3 gruplarında eşit sayıda olduğu tespit edilmiştir.

Tüm bu sonuçlar dikkate alındığında, analiz için seçilen depremlerin aynı spektruma göre belirlenmiş olsalar dahi aynı sonuçlar vermeyebileceği ve sonuçlar açısından yakın depremlerin yapıya çok daha fazla hasar verdiği sonucuna varılmıştır.

References

[1] Alyamaç E.A., Erdoğan A.S., Geçmişten Günümüze Afet Yönetmelikleri ve Uygulamada Karşılaşılan Tasarım Hataları, *Deprem Sempozyumu*, Kocaeli, Turkey, pp. 707-715

[2] DBYBHY-2007, Deprem Bölgelerinde Yapılacak Binalar Hakkında Yönetmelik, *T.C. Bayındırlık ve İskan Bakanlığı Afet İşleri Genel Müdürlüğü, Deprem Araştırma Dairesi Başkanlığı*, Ankara, Turkey, 2007

[3] Akkar, S, Yazgan, U, Gulkan, P., Drift Estimates in Frame Buildings Subjected to Near-Fault Ground Motions, *Journal of Structural Engineering ASCE*, 131 (2005), pp. 1014–1024

[4] Archuleta, R.J., Hartzell, S.H., Effect of Fault Finiteness on Near-Source Ground Motion, *Bulletin of the Seismological Society of America*, 71 (1981), pp. 939–957

[5] Megawati, K., Higashihara, H., Koketsu, K., Derivation of Near-Source Ground Motions of the 1995 Kobe (Hyogo-ken Nanbu) Earthquake from Vibration Records of the Akashi Kaikyo Bridge and Its Implications, *Engineering Structures* 23 (2001), pp. 1256–1268

[6] Pulido, N., Kubo, T, Near-Fault Strong Motion Complexity of the 2000 Tottori Earthquake (Japan) from a Broadband Source Asperity Model, *Tectonophysics*, 390 (2004), pp. 177–192

[7] Chopra, A.K., Chintanapakdee, C., Comparing Response of SDF Systems to Near-Fault and Far-Fault Earthquake Motions in the Context of Spectral Regions, *Earthquake Engineering and Structural Dynamics*, 30 (2001), pp. 1769–1789

[8] Adanur, S., Altunişik, A.C., Bayraktar, A., Akköse, M., Comparison of Near-Fault and Far-Fault Ground Motion Effects on Geometrically Nonlinear Earthquake Behavior of Suspension Bridges, *Natural Hazards*, 64 (2012), pp. 593-614

[9] Zhang, S., Wang, G., Effects of Near-Fault and Far-Fault Ground Motions on Nonlinear Dynamic Response and Seismic Damage of Concrete Gravity Dams, *Soil Dynamics and Earthquake Engineering*, 53 (2013), pp. 217-229

[10] Liu, T., Luan, Y., Zhong, W., Earthquake Responses of Clusters of Building Structures Caused by a Near-Field Thrust Fault, *Soil Dynamics and Earthquake Engineering*, 42 (2012), pp. 56-70

[11] Mazza, F., Vulcano, A., Effects of Near-Fault Ground Motions on the Nonlinear Dynamic Response of Base-Isoleted R.C. Framed Buildings, *Earthquake Engineering and Structural Dynamics*, 41 (2012), pp. 211-232

[12] Sta4Cad V12.1, Statik ve Betonarme Yapı Analizi Programı, *STA Bilgisayar ve Mühendislik Ltd. Şti*., İstanbul, Turkey, 2007

[13] TSE-500, Betonarme Yapıların Tasarım ve Hesap Kuralları, *Türk Standartlar Enstitüsü*, Ankara, Turkey, 2000

[14] TSE-498, Yapı Elemanlarının Boyutlandırılmasında Alınacak Yüklerin Hesap Değerleri, *Türk Standartları Enstitüsü*, Ankara, Turkey, 1997

[15] Perform3D V.5., Structural-Engineering Software, *Computer & Structures INC*, USA, 2011

[16] PEER Ground Motion Database, http://peer.berkeley.edu/peer_ground_motion_database

[17] ASCE 7-16, Minimum Design Loads for Buildings and Other Structures, *American Society of Civil Engineering/Structural Engineering Institude*, USA, 2016

Vol 7, Number 1, 2017
European Journal of Technic
EJT

AN EFFICIENT ADAPTIVE CONTROLLER DESIGN FOR THREE PHASE INDUCTION MOTORS BASED ON RBF NEURAL NETWORK

Erdal KILIÇ[1*], Sami ŞIT[2], Hasan Rıza ÖZÇALIK[2], Ahmet GANI[2]

[1*] Afşin Vocational School, Kahramanmaras Sutcu Imam University, Kahramanmaraş, Turkey

[2]Department of Electrical Electronics Engineering, Faculty of Engineering, Kahramanmaras Sutcu Imam University, Kahramanmaraş, Turkey

[*] Corresponding author; ekilic@ksu.edu.tr

Received: 11 November 2016; Accepted: 2 January 2017

ABSTRACT: *There are difficulties in control of induction motors which are widely used in industrial applications due to their nonlinear complicated structures. Nowadays the use of advanced control methods along with technological progress has made it possible to achieve high performance in the control of these motors. Thanks to its nonlinear and adaptive structure, artificial neural network based control algorithms will be a suitable and efficient method for control of induction motors. In this study, the speed control of three-phase squirrel cage induction motor was implemented using the dsPIC30F6010A microcontroller. In order to improve the performance of the drive system, a speed control algorithm has been developed using a radial basis function artificial neural network based model reference adaptive control method. The success of the proposed control algorithm has been experimentally tested by operating the induction motor under different speed and load conditions.*

Key words: *induction motor, vector control, artificial neural networks, model reference adaptive control, dsPIC microcontroller.*

1. GIRIŞ

Asenkron motorların günümüz endüstrisinde yaygın kullanımı bu motorların sağlamlığı, yüksek verimliliği ve işletme güvenilirliğinden kaynaklanmaktadır. Bu motorlar aynı güçteki doğru akım motorları ile karşılaştırıldığında daha az bakım gerektirmekte, hacim ve ağırlık olarak daha küçük olmakla birlikte daha makul maliyetleri bulunmaktadır. Ancak karmaşık ve doğrusal olmayan yapıları nedeniyle asenkron motorları geniş bir yelpazede kontrol etmek oldukça zor olmaktadır. Bu nedenle kontrol hedeflerine ulaşmak güçlü ve sağlam kontrol algoritmaları yanında gelişmiş motor sürücü sistemleri de gerektirmektedir[1-5].

Asenkron motor sürücülerinde yüksek dinamik performansa sahip hız ve tork kontrol tekniklerini belirlemek amacıyla gerçekleştirilen birçok araştırma bulunmaktadır[6-11]. Bu çalışmalardan asenkron

motor kontrol uygulamalarında performans gereksiniminin vektör kontrol tekniğiyle karşılanabildiği görülmektedir. Vektör kontrol yönteminde, uzay vektörleri kontrol algoritmasına göre işlenerek üç fazlı motorun gerilim ve akım anlık değerleri ayarlanır[12].

Asenkron motorların hız kontrolünde, genellikle basit yapılarından dolayı geleneksel PI tipi denetleyiciler tercih edilmektedir. Ancak sistemin doğrusal olmayan yapısı ve değişen motor dinamiklerinin etkisi nedeniyle bu denetleyicilerden iyi bir performans elde edilememektedir[13]. Bu nedenle asenkron motor uygulamalarında adaptif, dayanıklı ve doğrusal olmayan denetleyiciler kullanılmaya başlanmıştır.

Model referans adaptif kontrol (MRAK), parametreleri bilinmeyen veya kısmen bilinen karmaşık doğrusal olmayan sistemlerin kontrolünde yaygın kullanılan adaptif kontrol yöntemlerindendir. Bazı ayarlanabilir denetleyici parametreleri ve bunları ayarlamak için bir ayarlama mekanizması ile doğrudan uyumlu bir kontrol sistemidir. Bu yöntemde, sistem çıkışının kararlılığı bilinen bir referans model çıkışını takip etmesi amaçlanır. Referans model, sistemde yükselme zamanı, maksimum aşım, kararlı hal hatası ile ilgili istenen özelliklere sahip ideal bir modeldir. Denetleyicinin performansı, uygun referans model seçimi ve ayar mekanizmasının yeteneğine bağlıdır[14-16].

Yapay sinir ağları (YSA) öğrenme ve adapte yeteneği sayesinde doğrusal olmayan dinamik sistemlerin modelleme ve kontrolünde yaygın olarak kullanılmaktadır[17-18]. Son yıllardaki çalışmalardan radyal taban fonksiyonlu yapay sinir ağları (RTYSA) asenkron motor sürücü sistemlerinde dayanıklılığı ve performansı artırdığı görülmektedir[19-21]. Bu çalışmada RTYSA sistemden gelen doğrusal olmayan kısımları kompanze etmek amacıyla denetleyici yapısında kullanılmıştır.

Bu çalışmada, asenkron motor sürücülerinde güvenilirliği ve verimliliği artırmak amacıyla RTYSA tabanlı MRAK bir denetleyici geliştirilmiştir. Bu denetim algoritması üç fazlı sincap kafesli 0.25 kW gücünde bir asenkron motorun hız kontrolünde deneysel olarak farklı hız ve yük durumları için test edilmiştir. Motorun sürme yönteminde yüksek performanslı asenkron motor sürücülerinde kullanılan dolaylı alan yönlendirmeli kontrol tekniği tercih edilmiştir. Üç fazlı eviricinin anahtarlamasında uzay vektör darbe genişlik modülasyon tekniği kullanılmıştır. Bu teknik yüksek hesaplama gücü gerektirdiğinden gelişmiş bir sayısal işaret işleyici olan dsPIC30F6010A mikrodenetleyicisi kullanılmıştır.

2. YÖNTEM

2.1 RTYSA Yapısı

RTYSA danışmanlı öğrenme algoritması kullanan çok katmanlı ileri beslemeli ağ mimarisine sahiptir. Bu ağ yapısı giriş, gizli ve çıkış olmak üzere üç farklı katmandan oluşmaktadır. RTYSA'da gizli katman aktivasyon fonksiyonu olarak genellikle doğrusal olmayan yapıya sahip Gauss Fonksiyonu kullanılır[22-23].

$$\phi_j(x) = \exp\left[\frac{-\|x - c_j\|^2}{\sigma_j{}^2}\right] \quad (1)$$

Burada x giriş vektörünü, c_i merkez vektörünü, ||x-ci|| standart Öklid uzaklığını, σ_j radyal taban fonksiyon genişliğini göstermektedir. c_i ve σ_j'ler giriş değerlerinin aralığına göre belirlenir. RTYSA'nın eğitimi adaptif parametrelerin (c_i, σ_j ve çıkış ağırlıkları w_{kj}) optimize edilmesi sürecidir[24-25].

Bu çalışmada Şekil-1'de gösterildiği gibi RTYSA topolojisi 2:5:1 (giriş katmanı düğüm sayısı 2, gizli katman düğüm sayısı 5 ve çıkış katmanı düğüm sayısı 1) ağ mimarisi yapısında seçilmiştir.

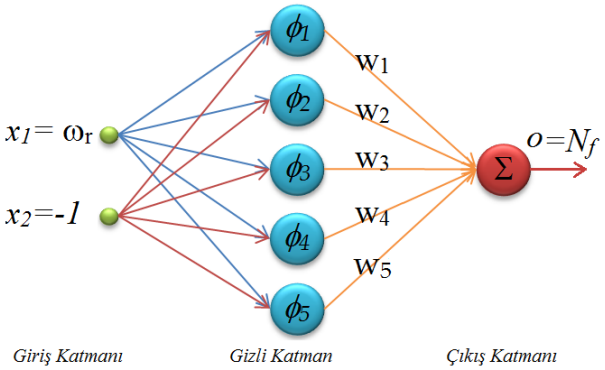

Şekil 1. RTYSA Yapısı

Ağ çıkışı aşağıdaki gibi ifade edilir:

$$o_k = \sum_{j=1}^{J} w_{kj}\phi_j(x) \tag{2}$$

Ayarlanabilen RTYSA parametreleri hatanın geri yayılım algoritması kullanılarak online ayarlanır.

$$w_{kj}(t+1) = w_{kj}(t) + \eta e(t)\phi_j \tag{3}$$

$$c_j(t+1) = c_j(t) + \eta e(t)\phi_j w_j \frac{(x - c_j)}{\sigma^2} \tag{4}$$

$$\sigma_j(t+1) = \sigma_j(t) + \eta e(t)\phi_j w_j \frac{\|x - c_j\|}{\sigma^3} \tag{5}$$

Burada η (0,1) aralığında seçilen öğrenme katsayısıdır. *e(t)* izleme hatasını göstermek üzere RTYSA'nın eğitilmesi için minimize edilmesi amaçlanan performans fonksiyonu aşağıdaki gibi ifade edilebilir.

$$E(t) = \frac{1}{2}e(t)^2 \tag{6}$$

2.2 Denetleyici Yapısı

MRAK algoritması adaptif bir denetleyici tasarlanması için kullanılmıştır. Bu yöntem sistem çıkışının referans model çıkışını takip edebilmesi için kontrol parametrelerini ayarlama prensibine göre çalışmaktadır. Şekil 2'de gösterildiği gibi önerilen kontrol şeması referans model ve RTYSA olmak üzere iki ana bölümden oluşmaktadır[26]. Sistem ve referans model ile ilgili diferansiyel eşitlik aşağıdaki gibi ifade edilebilir:

$$\dot{\omega}(t) + f\left[\omega(t)\right] = I_{sq}(t) \tag{7}$$

$$\dot{\omega}_m(t) + k_1\omega_m(t) = k_2\omega_{ref}(t) \tag{8}$$

Burada $\omega(t)$ ve $\omega_m(t)$ sırayla sistem ve referans model çıkışları; $I_{sq}(t)$ kontrol sinyali; $f(.)$ bilinmeyen statik doğrusal olmayan bir fonksiyon; k_1 ve k_2 pozitif katsayılardır.

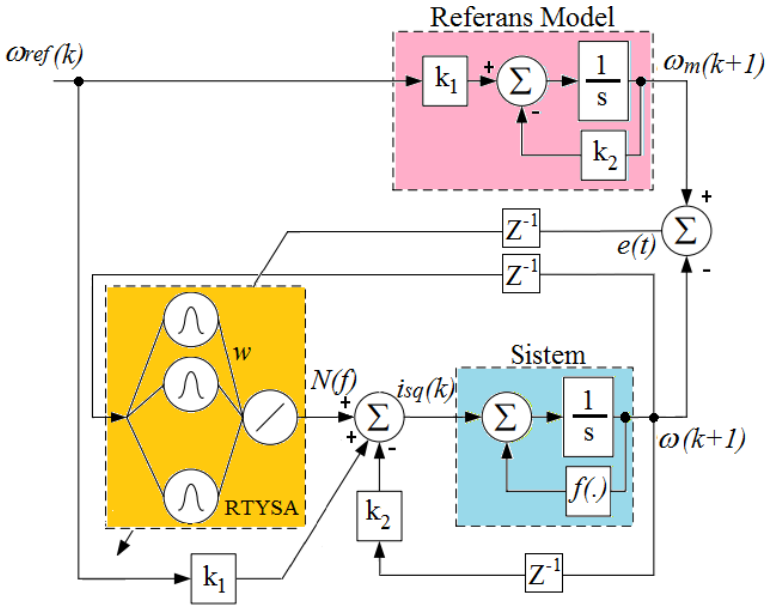

Şekil 2. RTYSA Tabanlı MRAK Yapısı

Model referans adaptif sistemin amacı kontrol edilen sistemin çıkışını model çıkışını izlemeye zorlayan bir denetleyici tasarlamaktır. Denetleyici tasarımı için, kontrol kuralı aşağıdaki gibi önerilebilir:

$$I_{sq}(t) = -k_2\omega(t) + k_1\omega_{ref}(t) + N_f\left[\omega(t), w(t)\right] \tag{9}$$

Burada N_f RTYSA çıkış vektörü; w RTYSA ağırlık vektörüdür. Ağ çıkışı N_f sistemin $f(.)$ ile ifade edilen doğrusal olmayan kısmını kompanze etmektedir. N_f aşağıdaki gibi ifade edilir.

$$N_f\left[\omega(t), w(t)\right] = \sum_{j=1}^{J} w_j(t)\exp\left[\frac{\left\|\omega(t) - c_j\right\|^2}{2\sigma^2}\right] \tag{10}$$

Eşitlik (7), (8) ve (9) birleştirilip yeniden yazılırsa aşağıdaki ifade elde edilir.

$$\left[\dot{\omega}(t) - \dot{\omega}_m(t)\right] + k_2\left[\omega(t) - \omega_m(t)\right] = N_f\left[\omega(t), w(t)\right] - f\left[\omega(t)\right] \tag{11}$$

Burada N_f asimptotik olarak $f(.)$'ye yaklaştığı zaman, izleme hatası $e(t)$ sıfıra doğru eğilim gösterecektir.

$$e(t) = \omega(t) - \omega_m(t) \tag{12}$$

$$\dot{e}(t) + k_2 e(t) \approx 0 \tag{13}$$

2.3 Deney Düzeneği

Deney düzeneği asenkron motorun hız kontrolünün gerçekleştirilmesi için tasarlanmıştır. Deney düzeneği dsPIC30F6010A mikrodenetleyici tabanlı motor kontrol geliştirme kartı, 1 kW doğrultucu ve evirici modülü, üç fazlı sincap kafesli 0.25 kW asenkron motor, yükleme amacıyla doğru akım şönt generatörü ve ölçüm cihazlarından oluşmaktadır. Asenkron motor sürücü sisteminin blok diyagramı Şekil 3'te, deney düzeneği ise Şekil 4'te gösterilmiştir.

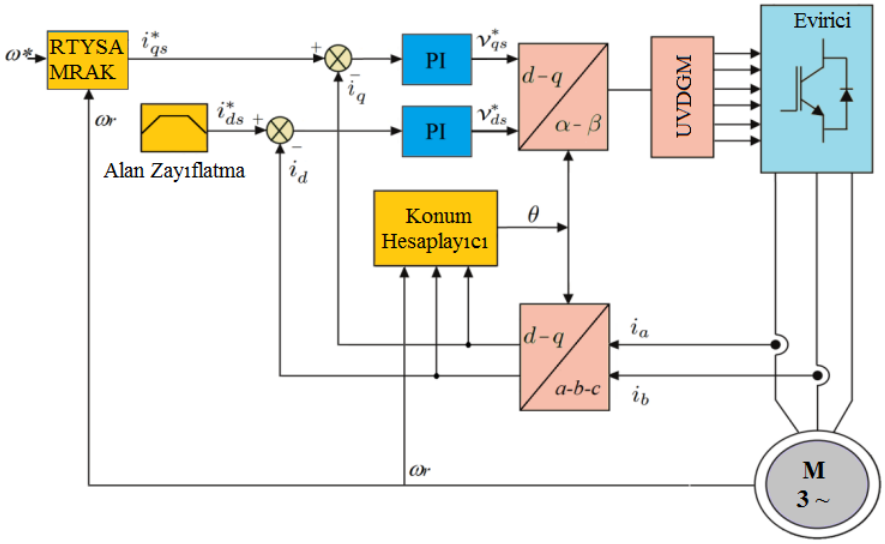

Şekil 3. Asenkron Motor Sürücü Sisteminin Blok Diyagramı

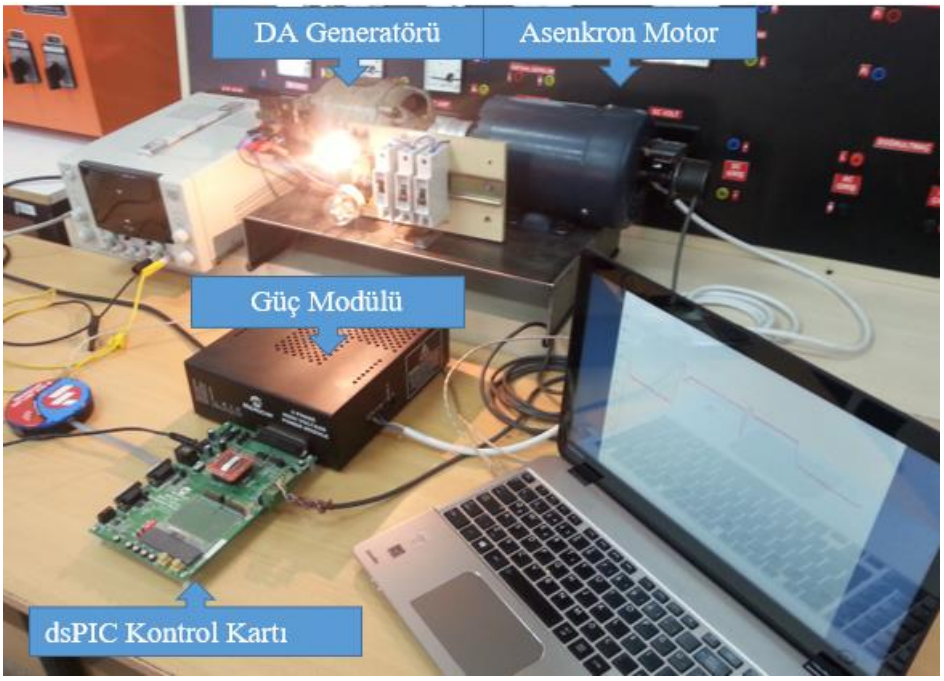

Şekil 4. Asenkron Motor Sürücü Sisteminin Deney Düzeneği

Kontrol sisteminde hız, akı ve torku kontrol eden üç kontrol döngüsü kullanılmaktadır. Önerilen RTYSA tabanlı MRAK hız kontrolörü olarak kullanılmıştır. Kontrol kartında akı ve tork kontrol döngüleri 100 µs'de, hız kontrol döngüsü ise 10 ms olarak yürütülmüştür. Eviricinin anahtarlama frekansı 10 kHz, ölü zaman ise 2 µs seçilmiştir. Asenkron motor sürücünün sistem cevabı ani referans hız ve ani yük değişimleri için gösterilmiştir.

3. BULGULAR

Asenkron motorun değişken hız referansları için elde edilen grafiği ve sistemin takip etmesi istenilen referans model çıkış işareti Şekil 5'te gösterilmiştir. Motora 1000 d/d referans hız ile yüksüz olarak yol verilmiştir. Çalışmanın 5. saniyesinde referans hız değeri 1000 d/d'dan 1500 d/d'ya çıkarılmıştır. Çalışmanın 15. saniyesinde referans hız değeri 1500 d/d'dan 1200 d/d'ya düşürülmüştür. Referans tork karakteristiğini temsil eden hız denetleyicisinin ürettiği kontrol işareti Şekil 6'da gösterilmiştir.

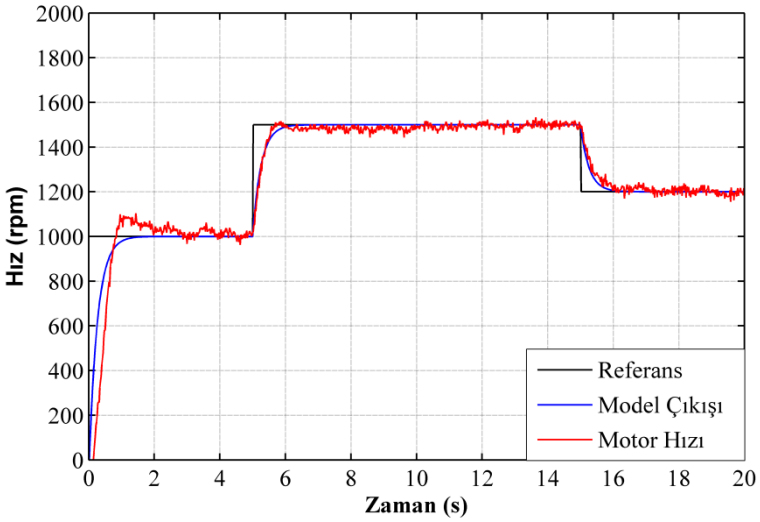

Şekil 5. Asenkron Motor Referans Hız Değişimlerindeki Hız Cevabı

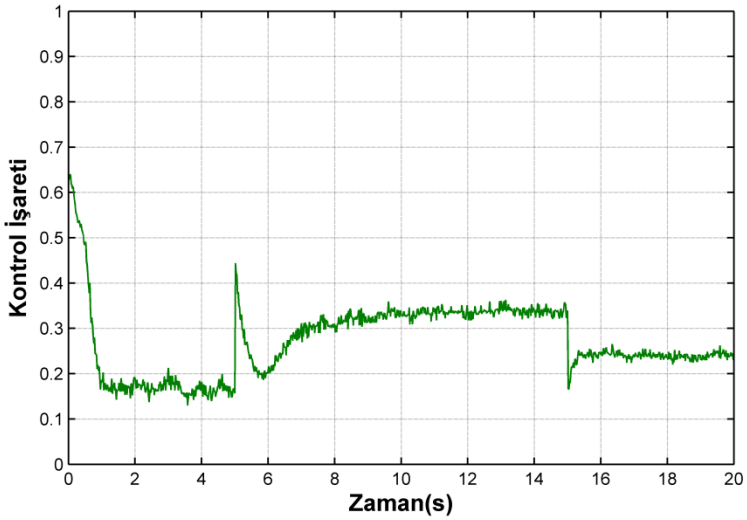

Şekil 6. Asenkron Motor Referans Hız Değişimlerindeki Kontrol Işareti

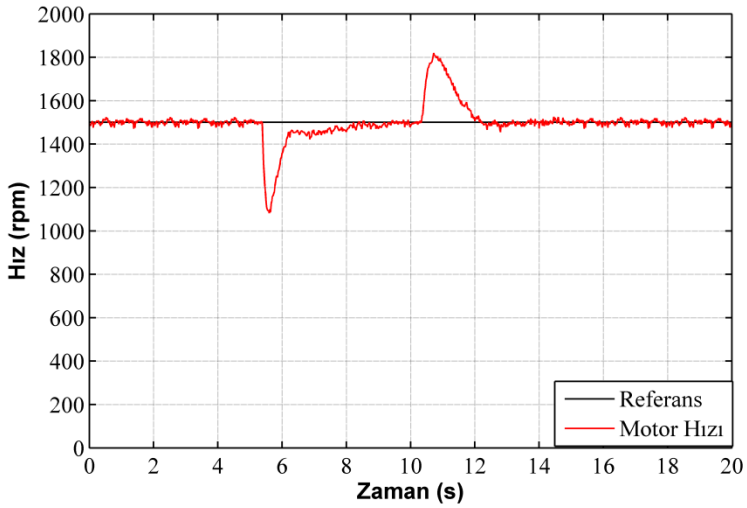

Şekil 7. Asenkron Motor Referans Yük Değişimlerindeki Hız Cevabı

Asenkron motor 1500 d/d referans hızda kararlı durumda çalışırken doğru akım generatörüne bağlı lamba yükü devreye alınmıştır. Bu yüklenme durumu asenkron motorun hızında anlık düşüşe sebep olmuştur. Denetleyici motor hızını tekrar kararlı duruma getirmiştir. Yine motor kararlı durumda çalışırken lamba yükü devreden çıkarılmıştır. Bu durum motorun hızında anlık yükselme etkisi oluşturmuştur. Denetleyici etkiyi telafi ederek motorun istenilen hızda çalışmasına devam etmesini sağlamıştır. Yük değişimi altında elde edilen hız grafiği Şekil 7'de gösterilmiştir. Bu çalışma durumunda üretilen kontrol işareti Şekil 8'de gösterilmiştir.

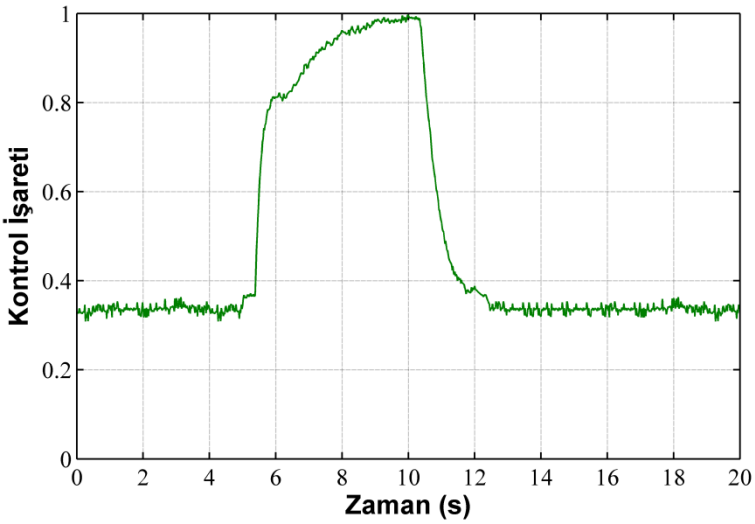

Şekil 8. Asenkron Motor Referans Yük Değişimlerindeki Kontrol Işareti

4. SONUÇ

Bu çalışmada, dsPIC30F6010A mikrodenetleyici tabanlı asenkron motor hız kontrol sistemi RTYSA tabanlı MRAK denetleyici kullanılarak gerçekleştirilmiştir. Dolaylı alan yönlendirmeli kontrol tekniğinde hız denetleyicisi olarak genellikle kullanılan PI denetleyici yerine RTYSA tabanlı MRAK denetleyici kullanılmıştır. Önerilen denetim algoritmasının performansı farklı çalışma koşullarında deneysel verilerle sunulmuştur.

Motora ait hız grafikleri incelendiğinde referans hızın değişim bölgelerinde sistemin istenilen değerler kısa sürede ulaştığı, aşmanın küçük olduğu ve sürekli hal hatasının oldukça küçük kaldığı görülmektedir. Yük değişiminin motor hızında oluşturduğu bozucu etki denetleyici tarafından kısa sürede ve yumuşak geçişle düzeltilmiştir. RTYSA tabanlı MRAK denetim yönteminin, yüksek dinamik performans gerektiren vektör kontrollü asenkron motor sürücülerinde kullanılması önerilmiştir.

KAYNAKLAR

1. Açıkgöz, H., & Şekkeli, M. (2013). Bulanık Mantık Denetleyici ile Doğrudan Moment Denetim Yöntemi Uygulanan Asenkron Motorun Hız Denetim Performansının Incelenmesi. *Akademik Platform Mühendislik ve Fen Bilimleri Dergisi, 1*(2), 50-57.
2. Daya, J. F., & Subbiah, V. (2012). A novel wavelet-fuzzy-based controller for robust speed control of induction motor drives. *Australian Journal of Electrical and Electronics Engineering, 9*(2), 185-195.
3. Mannan, M. A., Murata, T., Tamura, J., & Tsuchiya, T. (2006). A fuzzy-logic-based self-tuning PI controller for high-performance vector controlled induction motor drive. *Electric Power Components and Systems, 34*(4), 471-481.
4. Özçalık, H. R., Yıldız, C., Danacı, M., & Koca, Z. (2007). *RBF based induction motor control with a good nonlinearity compensation.* Paper presented at the International Work-Conference on Artificial Neural Networks.
5. Ustun, S. V. (2007). GA-based optimization of PI speed controller coefficients for ANN-modelled vector controlled induction motor. *Applied Sci, 7*, 4001-4006.
6. Kılıç, E., Özçalık, H. R., Yılmaz, Ş., & Şit, S. (2015). *A comparative analysis of FLC and ANFIS controller for vector controlled induction motor drive.* Paper presented at the 2015 Intl Aegean Conference on Electrical Machines & Power Electronics (ACEMP), 2015 Intl Conference on Optimization of Electrical & Electronic Equipment (OPTIM) & 2015 Intl Symposium on Advanced Electromechanical Motion Systems (ELECTROMOTION).
7. Kim, D. H. (2007). GA–PSO based vector control of indirect three phase induction motor. *Applied Soft Computing, 7*(2), 601-611.
8. Lin, F.-J., Wai, R.-J., Kuo, R.-H., & Liu, D.-C. (1998). A comparative study of sliding mode and model reference adaptive speed observers for induction motor drive. *Electric Power Systems Research, 44*(3), 163-174.
9. Menghal, P., & Laxmi, A. J. (2013). *Adaptive Neuro Fuzzy based dynamic simulation of induction motor drives.* Paper presented at the Fuzzy Systems (FUZZ), 2013 IEEE International Conference on.
10. Ramesh, T., Panda, A. K., & Kumar, S. S. (2015). Type-2 fuzzy logic control based MRAS speed estimator for speed sensorless direct torque and flux control of an induction motor drive. *ISA transactions, 57*, 262-275.
11. Vas, P. (1990). *Vector control of AC machines* (Vol. 22): Oxford University Press, USA.
12. Trzynadlowski, A. M. (2000). *Control of induction motors*: Academic press.
13. Şit, S., Özçalık, H. R., Kılıç, E., & Yılmaz, Ş. (2015). Üç Fazlı Asenkron Motor Sürücülerinde Hız Kontrol Yöntemlerinin Araştırılması.
14. Al-Aubidy, K., & Ali, M. (2004). A Hierarchical Neuro-Fuzzy MRAC of a Robot in Flexible Manufacturing Environment. *Int. Arab J. Inf. Technol., 1*(2), 209-214.
15. Jain, P., & Nigam, M. (2013). Design of a model reference adaptive controller using modified MIT rule for a second order system. *Advance in Electronic and Electric Engineering, ISSN*, 2231-1297.
16. Prakash, R., & Anita, R. (2012). Modeling and simulation of fuzzy logic controller-based model reference adaptive controller. *International Journal of Innovative Computing, Information and Control, 8*(4), 2533-2550.
17. Efe, M. Ö., & Kaynak, M. O. (1997). *Doğrusal Olmayan Dinamik Sistemlerin Yapay Sinir Ağları Tarafından Tanınması ve Denetimi*. Paper presented at the TOK'97 Endüstriyel Otomasyon Teknolojileri Sempozyumu, Mecidiyeköy, Istanbul, Türkiye.

18. Kılıç, E., Özbalcı, Ü., & Özçalık, H. R. (2012). *Lineer Olmayan Dinamik Sistemlerin Yapay Sinir Ağları ile Modellenmesinde MLP ve RBF Yapılarının Karşılaştırılması*. Paper presented at the ELECO '2012 Elektrik - Elektronik ve Bilgisayar Mühendisliği Sempozyumu, Bursa.
19. Brandstetter, P., Kuchar, M., & Skuta, O. (2014). Implementation of RBF Neural Network in Vector Control Structure of Induction Motor. *International Review of Electrical Engineering (IREE), 9*(4), 749-756.
20. Qian, M., Pei, L., & Hui-xian, H. (2009). *Induction Motor Vector Control Based on Immune RBF Neural Network Sliding Mode Variable Control.* Paper presented at the 2009 International Conference on Signal Processing Systems.
21. Şit, S., Kılıç, E., Özçalık, H. R., Altun, M., & Gani, A. (2016). *Model Reference Adaptive Control based on RBFNN for Speed Control of Induction Motors*. Paper presented at the International Conference on Natural Science and Engineering (ICNASE'16), Kilis.
22. Haykin, S. (1999). *Neural Networks: A Comprehensive Foundation*. Upper Saddle River, New Jersey, USA.: Prentice Hall.
23. Zhang, M.-G., Li, W.-H., & Liu, M.-Q. (2005). *Adaptive PID control strategy based on RBF neural network identification.* Paper presented at the 2005 International Conference on Neural Networks and Brain.
24. Okkan, U., & Dalkılıç, H. Y. (2012). Radyal tabanlı yapay sinir ağları ile Kemer Barajı aylık akımlarının modellenmesi. *Teknik Dergi, 23*(112).
25. Qin, L., Zhou, X., & Cao, P. (2012). New control strategy for PMSM driven bucket wheel reclaimers using GA-RBF neural network and sliding mode control. *Elektronika ir Elektrotechnika, 122*(6), 113-116.
26. Patino, H. D., & Liu, D. (2000). Neural network-based model reference adaptive control system. *IEEE Transactions on Systems, Man, and Cybernetics, Part B (Cybernetics), 30*(1), 198-204.